LBL-15013
c.2

Lawrence Berkeley Laboratory
UNIVERSITY OF CALIFORNIA

RECEIVED
LAWRENCE
BERKELEY LABORATORY
NOV 16 1982
LIBRARY AND
DOCUMENTS SECTION

Accelerator & Fusion Research Division

CROSS SECTIONS FOR BALMER-ALPHA EXCITATION IN HEAVY PARTICLE COLLISIONS

Young Kun Bae
(Ph. D. thesis)

August 1982

TWO-WEEK LOAN COPY
This is a Library Circulating Copy which may be borrowed for two weeks. For a personal retention copy, call Tech. Info. Division, Ext. 6782.

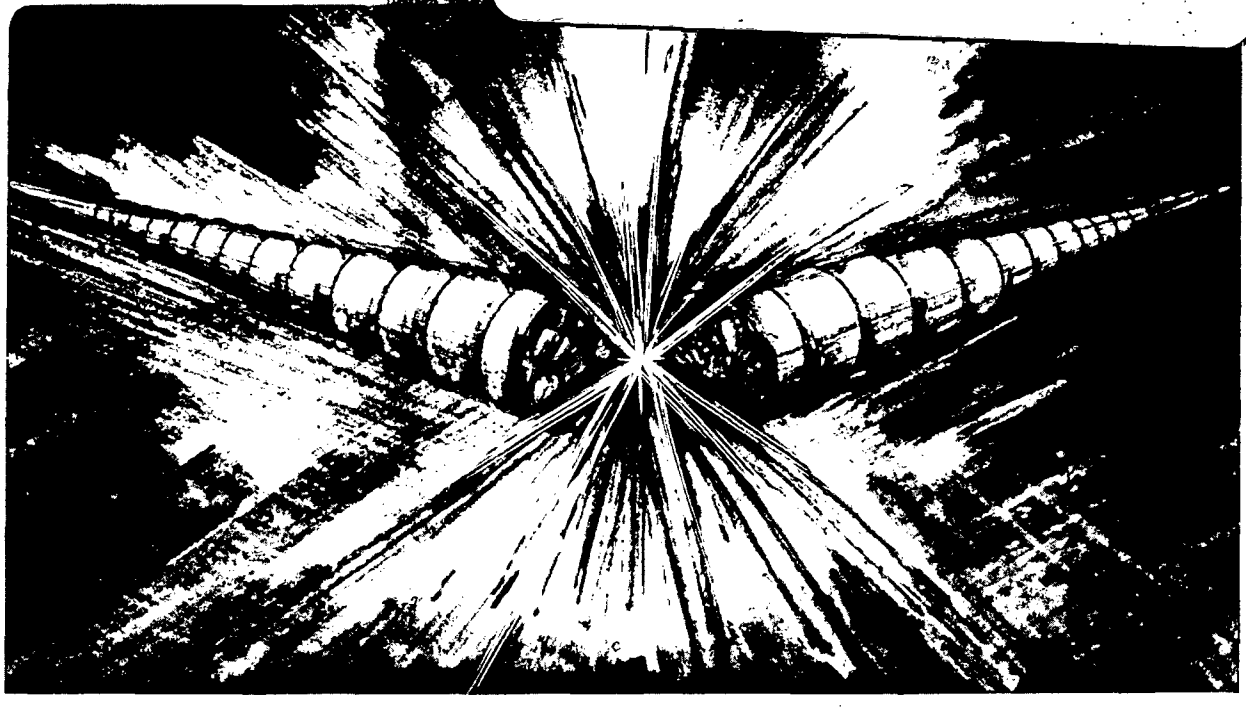

Prepared for the U.S. Department of Energy under Contract DE-AC03-76SF00098

LBL-15013
c.2

DISCLAIMER

This document was prepared as an account of work sponsored by the United States Government. While this document is believed to contain correct information, neither the United States Government nor any agency thereof, nor the Regents of the University of California, nor any of their employees, makes any warranty, express or implied, or assumes any legal responsibility for the accuracy, completeness, or usefulness of any information, apparatus, product, or process disclosed, or represents that its use would not infringe privately owned rights. Reference herein to any specific commercial product, process, or service by its trade name, trademark, manufacturer, or otherwise, does not necessarily constitute or imply its endorsement, recommendation, or favoring by the United States Government or any agency thereof, or the Regents of the University of California. The views and opinions of authors expressed herein do not necessarily state or reflect those of the United States Government or any agency thereof or the Regents of the University of California.

LBL-15013

CROSS SECTIONS FOR BALMER-ALPHA EXCITATION IN HEAVY PARTICLE COLLISIONS*

Young Kun Bae

Ph.D. Thesis

Accelerator and Fusion Research Division
Magnetic Fusion Energy Group
Lawrence Berkeley Laboratory
University of California
Berkeley, CA 94720

August 1982

* This work was supported by the Director, Office of Fusion Energy, Applied Plasma Physics Division of the U.S. Department of Energy under Contract No. DE-AC03-76SF00098.

CROSS SECTIONS FOR BALMER-α EXCITATION IN HEAVY PARTICLE COLLISIONS

Young Kun Bae

Lawrence Berkeley Laboratory
University of California
Berkeley, CA 94720

August 1982

ABSTRACT

Doppler shifted and unshifted Balmer-alpha radiation has been observed in the absolute sense for energetic H^+, H_2^+ and H_3^+ ions incident on molecular hydrogen by the method of decay inside the target within the energy range of 20 keV to 150 keV. Most of the measurements were based on single-collision conditions, but a simple thick-target experiment has been tried for the case of dissociative excitation of the target molecules by H atoms.

The Balmer-alpha radiation emitted by hydrogen and deuterium beams has been used as a diagnostic method of neutral beam parameters. One important neutral beam parameter is the species mix between H^+, H_2^+ and H_3^+ ion currents produced by the ion source and accelerator. This species mix can be resolved by analysis of the Balmer-alpha radiation if the beam is observed along an off normal axis with sufficient spectral resolution to separate the Doppler shifted radiation components from each other. An impediment to this approach to measuring the ion species is that some of the required cross sections have not been measured. This

is the motivation for the presented experimental work.

A home made monochromator gave enough optical throughput and spectral resolution for separation of the Doppler shifted lines from the unshifted lines. By selectively varying the target pressure and the distance of travel into the target prior to the observation region, excitation cross sections for three different angular momentum states (3s, 3p and 3d) have been determined. Combinations of a linear polarizer and a half-wave plate were used for polarization measurement. Separation of the individual Zeeman levels has been tried for the 3p state from the information obtained from the polarization. Theoretical estimates of the cascading corrections have been applied in the case of both thin and thick targets. The intensity development equations for thick targets also have been derived.

Cross sections for 3s production show general agreement with previous measurements, while those for 3p and 3d differ by as much as a factor of two. Target dissociative excitation cross sections show good agreement with previous measurements except those measured by Williams, et al..

ACKNOWLWDGEMENT

The author wishes to thank all the members of the MFE group for their help throughout the course of this work. The author especilly wixhes to thank Prof. Robert H. McFarland for his excellent guidance and encouragement, Prof. Robert V. Pyle for his good advice and support, Dr. Klaus H. Berkner for his criticism and useful help, Dr. Charles F. Burrell for his nice and kind help, and Prof. Wulf B. Kunkel for his kind guidance. Many valuable suggestions were given by Mr. John W. Stearns and Dr. Darlene J. Markevich.

CONTENTS

PAGE

1. Introduction ---------- 1
2. Theory
   A. General Atomic Physics ---------- 10
   B. Lifetime of the Excited States and Intensity Development Equations ---------- 15
   C. Polarization ---------- 22
3. Apparatus
   A. Monochromator and Other Optics ---------- 29
   B. Ion Source and Accelerator ---------- 33
   C. Target System ---------- 36
   D. Detector ---------- 40
4. Procedure and Data Analysis
   A. Absolute Optical Calibration ---------- 50
   B. Beam Tuning ---------- 58
   C. Development of Spectral Profile ---------- 59
   D. Linearity Test ---------- 61
   E. Data Analysis ---------- 65
5. Results and Discussion
   A. Results ---------- 73
   B. Discussion ---------- 92
6. Conclusions ---------- 95
7. References ---------- 99
8. Appendices
   A. Discussion of the Monochromator ----------103
   B. Comments on the Thick Target Experiments --------107

CHAPTER 1

Introduction

There has been considerable effort to derive useful energy from fusion reactions for many years. One of the most advanced and prospective technologies for a practical fusion reactor utilizes magnetic confinement which contains the fusion plasma with strong magnetic fields. To achieve a plasma with the necessary high temperature the usual reactors require auxiliary plasma heating, for which a promising technique is injecting of energetic neutral deuterium beams into the plasma.(1) These pass through the confining magnetic field and get trapped in the confinement region by either charge exchange or ionization collision processes. Thereafter the beam energy is shared with the target plasma by Coulomb collisions. A brief explanation of the idea is shown in Fig. 1-1; D^+, D_2^+ and etc. ions are formed in the ion source. After acceleration they are neutralized in the gas neutralizer. Usually this neutralization process is extremely complicated since it involves multiple atomic and molecular collisions. The beam will be composed of only neutral particles after it goes through the gas neutralizer and sweeping magnet which eliminate charged particles from the beam.

To develop a multi-mega watt neutral atom beam, it is required for the beam to travel over a distance of several meters with a minimum loss. Therefore, it is vital to be

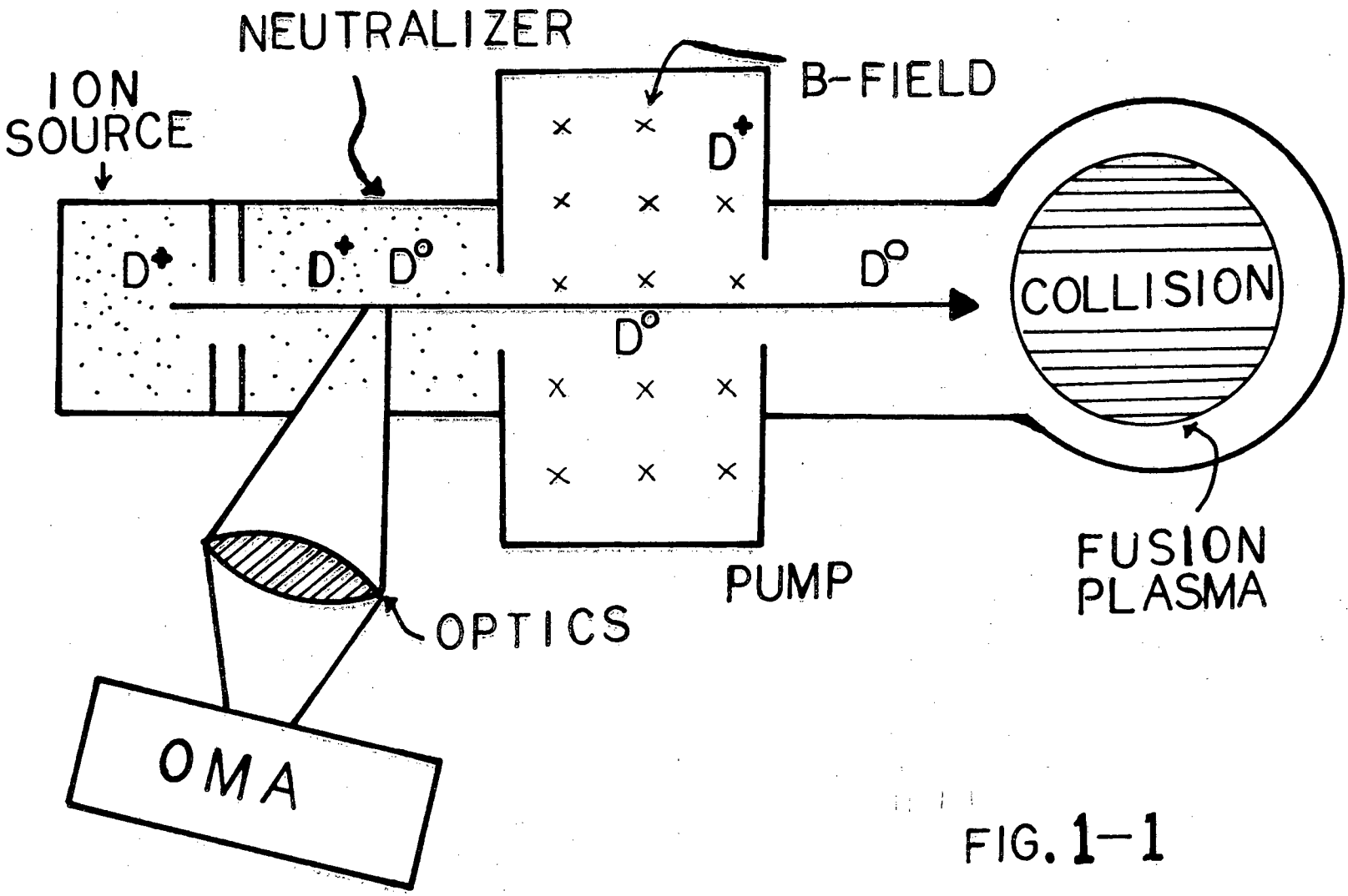

FIG. 1-1

XBL 829-11769

able to define and measure both the beam steering direction and beam angular divergence. It is also important to be able to measure the relative quantities of the different species in the mixed ion beam extracted from the ion source. The resulting neutral beam before injecting into the plasma is composed of D^o with full energy E, which comes from D^+, D^o with E/2 and D_2^o with E from D_2^+, D^o with E/3 and D_2^o with 2E/3 from D_3^+ and D^o with E/10 from D_2O^+. This is shown in Fig. 1-2 schematically.

In general the effective charge exchange and ionization cross sections depend on the beam energy. Hence, the mean free path lengths of the neutrals are dependent on both beam energy and beam species. Moreover in these neutral beams the peak power density may approach 30 kW/cm^2 which is at least one order of magnitude higher than can be deposited on even cooled conventional diagnostic probes. Therefore, it has been long desired to develop alternative non-disturbing diagnostic methods. One of the most successful methods is the optical spectroscopic beam diagnostics[1a]. The spectrum of Balmer-alpha radiation emitted by fast deuterium neutrals is observed inside the neutralizer along an optic axis at an angle to the neutral beam axis. The radiation is Doppler shifted sufficiently to resolve the three dominant energy components of the neutral beam. The typical spectrum of the radiation is shown in Fig. 1-3.

To make a quantitative assessment of such a spectrum,

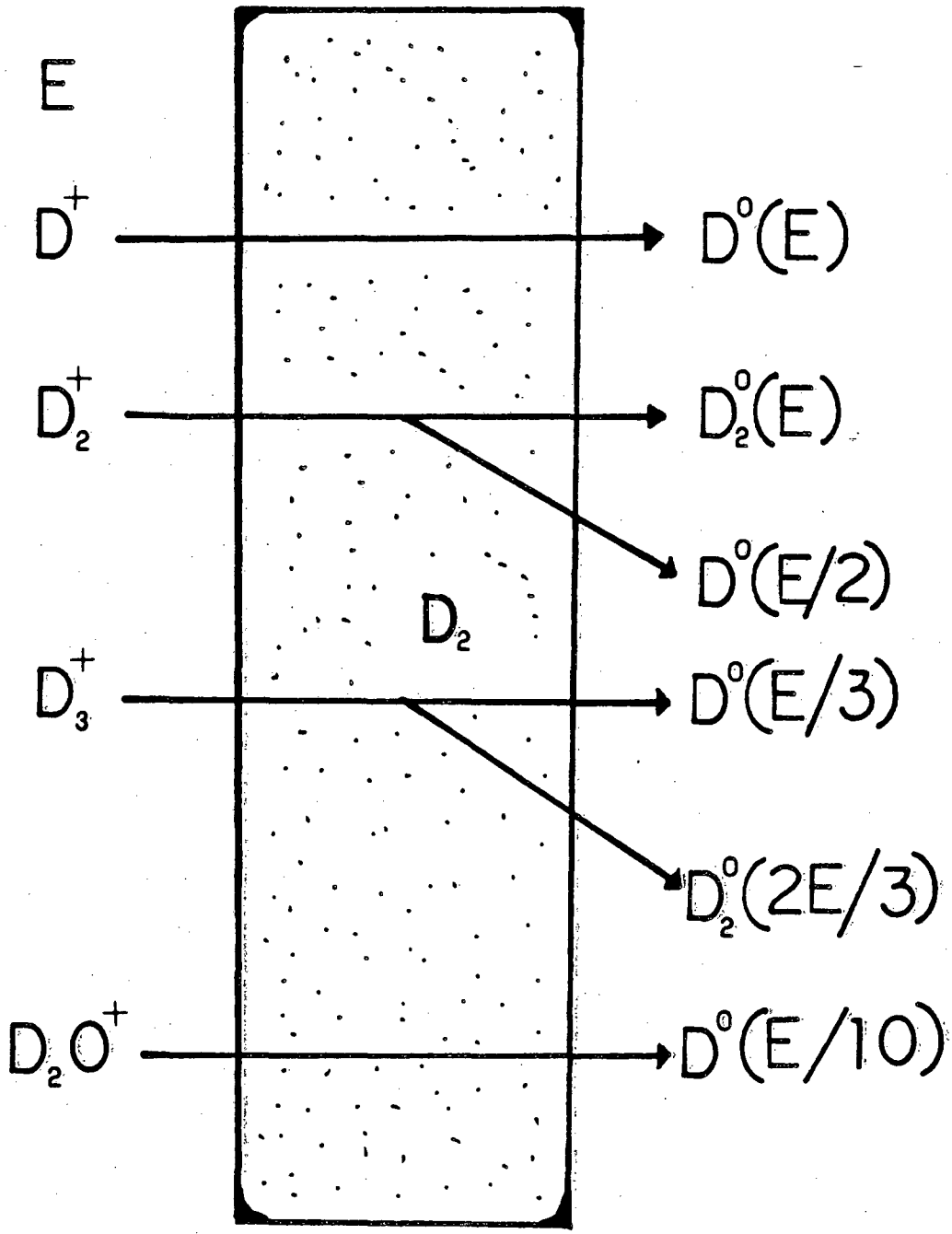

XBL 829-11770

FIG. 1-2

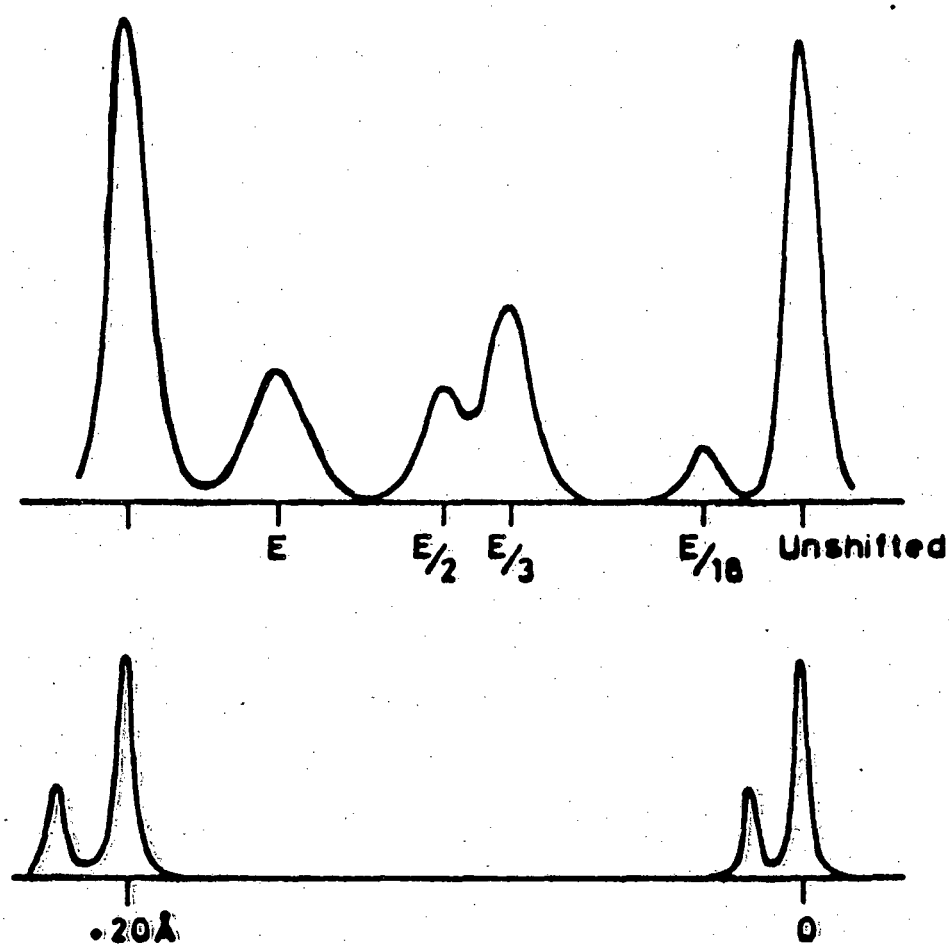

Upper: Fabry-Parot Interferogram of Beam

Lower: that of calibration H-alpha source

TYPICAL SPECTRAL PROFILE FROM NEUTRALIZER

XBL 829-11771

Fig. 1-3

many kinds of cross sections for light emission are needed, some of which are unknown. The reason for the lack of knowledge is the inherently low signal to noise ratios normally experienced in the relevant experiments.

A number of authors have measured relevant cross sections for producing n=3 state hydrogen atoms by hydrogenic molecular ions and protons incident on molecular hydrogen. Hughes and co-workers[1b)-(11)] have reported measurements which are often utilized in on-going research related to fusion. Thomas and co-workers[(12)-(13)] and other authors have reported,[(14)-(25)] discussed and extended Hughes' works. A common characteristic of most of their experiments is that energetic ions and/or atoms were passed through a gas target cell, and the radiation of the fast emerging neutral atoms was observed down stream in a reduced pressure region. Thomas' work[(13)] was an exception. For Balmer-alpha this allowed a separation of the s, p and d states and a measurement of both excitation cross section and respective lifetimes.

In the work presented herein, the observation of the emitted light was within the target cell itself, and the Doppler shift was used for the separation of the radiation from the fast beam and that from the target gas. Furthermore, in this work it was possible to move the aperture so that the distance the beam traveled before observation as well as the gas pressure and beam energy could be varied as needed. The specific apparatus and method will be discussed

in the following chapters.

More specifically, the reactions

$$\underline{H}^{+} + H_2 \dashrightarrow \underline{H}^{+} + H + H^{*}(n=3 \text{ to } 2) \quad (1\text{-}1)$$

and

$$\underline{H}^{0} + H_2 \dashrightarrow \underline{H}^{0} + H + H^{*}(n=3 \text{ to } 2) \quad (1\text{-}2)$$

have been studied for H^{+} beam incident on a thick hydrogen target by using species development equations.[26]

The charge changing reaction leaving the fast atom in an excited state

$$\underline{H}^{+} + H_2 \dashrightarrow \underline{H}^{*}(3s,3p,3d) + (H_2^{+}) \quad (1\text{-}3)$$

has been studied with H^{+} ions and thin hydrogen gas targets.

The individual cross sections of Zeeman levels of the 3p to 2s transition were studied by observation of the polarization which gave correction factors for total cross section. In many cases it was difficult to measure polarizations due to the low level of polarization involved.

The reactions

$$\underline{H}_2^{+} + H_2 \dashrightarrow [\underline{H}_2^{+}] + H + H^{*}(n=3 \text{ to } 2) \quad (1\text{-}4)$$

and etc.,

$$\underline{H}_2^{+} + H_2 \dashrightarrow \underline{H}^{*}(3s,3p,3d) + \underline{H}^{+} + (H_2) \quad (1\text{-}5)$$

and etc.,

$$\underline{H}_3^{+} + H_2 \dashrightarrow [\underline{H}_3^{+}] + H + H^{*}(n=3 \text{ to } 2) \quad (1\text{-}6)$$

and etc.,

$$\underline{H}_3^+ + H_2 \text{ ---- } \underline{H}^*(3s,3p,3d) + (\underline{H}_2^+) + (H_2) \quad (1\text{-}7)$$

etc.

have been studied for H_2^+ and H_3^+ beams on thin hydrogen targets.

Only the cross sections of H^+ impact on H_2 had been known when this work started. Those measurements show good agreement with the present results. Recently Williams[28] et al. have measured the cross sections of the target dissociation, formation of the fast 3s state and the sum of 3p and 3d states for H^+, H_2^+ and H_3^+ impact on H_2 up to 100 keV, some of which show agreement with the present results. No exact theoretical estimates of these cross sections have been made due to the lack of knowledge of molecular collisions. For the purpose of rough comparison the theoretical values of the cross sections for H^+ impact on H atoms have been used. Because at high energy the bonding of molecules could be negligible, these values should be close to half of the value of H^+ impact on H_2 . It turned out this argument was right in many cases. The present results show very good agreement with these values too. The detailed comparison is given in Chapter 5 .

Thick-target experiments have been studied only for the dissociative excitation of target molecules for H^+ impact on H_2. The problems for other thick target experiments are the difficulties of the separation of an excited state hydrogen atom from the ground state hydrogen atom. The

second difficulty is that there are too many unknown parameters going together resulting in statistically poor confidence. The third difficulty was that the cross sections to be measured couldn't be independent measurements. Rather they were dependent on the knowledge of other cross sections measured in some cases by others. In that sense the thick-target experiments are not good for confident measurements. Hence, the target dissociation of H_2 molecules by H atoms was experimentally studied using both thin and thick targets, but the theoretical description for other thick target systems is given in Appendix B.

Originally only relative measurements were planned because in the real application absolute values aren't needed. But seldom do absolute values of the cross sections measured by different authors agree with each other. Normalization requirements and conflicting published results suggested the need for new absolute measurements leading to the absolute calibration of the light detecting system. An advantage of this calibration procedure came from the usage of a home made monochromator which gave a large acceptance solid angle and an accurate wave-length response spectrum. Another advantage came from the usage of a one-to-one image technique which made it possible to cancel all geometric factors as explained in Chapter 4.A .

CHAPTER 2

Theory

A. General Atomic Physics

In this section a brief survey of theoretical models and calculation methods for the excitation in heavy particle collisions will be presented. The phenomenon of interest in this work is the formation of excited states either by charge transfer or by dissociation. Relatively few theoretical calculations have been developed for those phenomena, because of the difficulty in the calculation of more than three body interactions. For the charge transfer calculation there have been three lines of approach in general; the Born approximation, the quantal impulse approximation and the binary encounter approximation. Although there is no exact definition, what is called low or high velocity is determined by the velocity of the first orbit electron in the Bohr atom; i.e. $v_0 = 2.19 \times 10^8$ cm/sec. For a collision between two systems at high energy the systems don't have enough time to interact strongly with each other, therefore the molecular effect can be negligible. In that case the Born approximation gives the simplest theoretical calculation. If the two systems are labeled A and B, then the Hamiltonian can be written as

$$H = (T_R + H_A + H_B) + V \qquad (2\text{-}1)$$

where $T_R = -(\hbar^2 / 2\mu) \nabla_R^2$ and H_A and H_B are Hamilton-

ians for the isolated systems A and B in a reference frame with respect to the center of mass of each system. $\vec{R}$ is the relative separation between the two centers of mass and V is the interaction potential between two systems. The differential cross section for a scattering of the system A by the system B accompanied by a transition of the internal structure of A and B from the initial state Ψ_I to the final state Ψ_F is given by[29a]

$$\frac{d\sigma}{d\Omega} = \left(\frac{\mu}{2\pi\hbar^2}\right)^2 \left(\frac{K_F}{K_I}\right) \quad |M_{FI}|^2 \tag{2-2}$$

where $\hbar\vec{K}_I$ and $\hbar\vec{K}_F$ are the initial and final relative momenta of the two systems and M_{FI} is

$$M_{FI} = \langle e^{i\vec{K}_F\cdot\vec{R}} \Psi_F \mid V \mid e^{i\vec{K}_I\cdot\vec{R}} \Psi_I \rangle \tag{2-3}$$

But for the case of rearrangement collisions like

$$A + B \text{ -------}\rangle \; C + D \tag{2-4}$$

the Hamiltonian is decomposed in two different ways

$$\begin{aligned} H &= T_I + H_A + H_B + V_I \\ H &= T_F + H_C + H_D + V_F \end{aligned} \tag{2-5}$$

But there is an ambiguity as to whether to use V_I or V_F as

V in the matrix element M_{FI}. This is called the post/prior discrepancy.

Earlier theoretical work applying this method to the electron capture by a proton incident on a hydrogen atom was undertaken by numerous authors[30]-[34]. Oppenheimer demonstrated that at high incident velocity charge capture occurs almost entirely to s-state and that the probability of capture into a state of principal quantum number n varies as n^{-3}. This is the famous n^{-3} law for charge capture cross sections.

In order to take into account multiple collisions of the charge exchanged electron which are important in the transfer process, a rigorous expression is given by[35]

$$\frac{d\sigma}{d\Omega} = \left(\frac{\mu}{2\pi\hbar^2}\right)^2\left(\frac{K_F}{K_I}\right) \left|R^+_{FI}\right|^2 \qquad (2\text{-}6)$$

where $R^+_{FI} = \langle e^{i\vec{K}_F\cdot\vec{R}} \Psi_F \mid V_F \mid e^{i\vec{K}_I\cdot\vec{R}} \Psi_I \rangle$

$+ \lim_{\varepsilon\to 0^+} \langle e^{i\vec{K}_F\cdot\vec{R}} \Psi_F \mid V_F \mid G_{\varepsilon+} V_I \; e^{i\vec{K}_I\cdot\vec{R}} \Psi_I \rangle$

and $G_{\varepsilon+} = (E - H + i\varepsilon)^{-1}$

This is the so-called quantal impulse approximation.[36]

In the binary encounter approximation[37], the atomic electrons and the nucleus of each system are considered to act as independent scattering centers. In other words the mutual interaction between components in the same system are neglected during the collision process.

All the theoretical results for the charge capture of a proton incident on the hydrogen atom are compared with experimental results for protons incident on molecular hydrogens, under the assumption that a hydrogen molecule acts like two isolated hydrogen atoms. But it has been shown[38] that this is not exactly true. It has been shown[39] that a previously overlooked backscattering contribution to the cross section becomes dominant in the high energy limit, making the cross section depend on energy as E^{-3} instead of E^{-6}.

Very few theoretical calculations have been developed for the dissociative excitation of the molecular beam. The detailed channel of molecular dissociation process will be followed. For H_2 target gas dissociation three possible mechanisms are

$$\underline{H}_m^+ + H_2 \dashrightarrow (\underline{H}_m) + H^* + H^+ \qquad (2\text{-}7)$$

$$\underline{H}_m^+ + H_2 \dashrightarrow (\underline{H}_m^+) + H^* + H^+ + e \qquad (2\text{-}8)$$

$$\underline{H}_m^+ + H_2 \dashrightarrow (\underline{H}_m^+) + H^* + H^* \qquad (2\text{-}9)$$

where m = 1, 2 and 3.

For the high energy proton the first and second processes can be ruled out by Keene's[40] failure to observe an appreciable number of slow protons in the study of protons impact on H_2. Even for m=2 and m=3 cases the third process would seem to be dominant since Afrosimov [41] has measured

secondary slow proton production by these ions impact on H_2 and found this to be small.

From the same argument as before the possible mechanisms for the projectile dissociation can be written as

$$\underline{H}_2^+ + H_2 \text{ ----- } \underline{H}^* + \underline{H}^* + (H_2^+) \quad (2\text{-}10)$$

$$\underline{H}_2^+ + H_2 \text{ ----- } \underline{H}^* + \underline{H}^+ + (H_2) \quad (2\text{-}11)$$

and

$$\underline{H}_3^+ + H_2 \text{ ----- } (\underline{H}_2) + \underline{H}^* + (H_2^+) \quad (2\text{-}12)$$

$$\underline{H}_3^+ + H_2 \text{ ----- } (\underline{H}_2^+) + \underline{H}^* + (H_2) \quad (2\text{-}13)$$

B. Life Time of the Excited States and Intensity Development Equations.

In order to calculate the life-time of a certain excited state one should determine transition probabilities between that state and other states, i.e. the matrix elements of the electric dipole moment between two states.

For the n=3 state there are three different angular momentum states, 3s, 3p and 3d and the effective life-time of the state i is given by

$$1/\tau_i = \sum_j A_{ij} \qquad (2\text{-}14)$$

where τ_i is the effective life time of the state i and A_{ij} is the transition probability between the higher state i and the lower state j. This leads to $\tau_{3s} = 16.0\times10^{-8}$ sec $\tau_{3p} = 0.54\times10^{-8}$ sec, and $\tau_{3d} = 1.56\times10^{-8}$ sec.[41a]

The light intensity equations along the beam direction are needed to evaluate the excitation cross sections from the experimental data. Under the single collision condition without cascading of the higher state into the state i, the differential equation for the number density of the projectile particles in the excited state i, N_{bi}, is given by

$$\frac{dN_{bi}}{dt} = (N_a \sigma_i^* v) N_b - (1/\tau_i) N_{bi} \qquad (2\text{-}15)$$

where N_b ; number density of the projectile,

N_a ; number density of the target,

σ_i^* ; excitation cross section into the state i,

v ; velocity of the projectile in the lab. frame.

Under the assumption that there is no collision in the pre-target region and setting the time as 0 when the projectile goes through the entrance aperture, the boundary condition for that equation is that at t=0, $N_{bi}=0$. Therefore

$$N_{bi} = K_i \left(1 - e^{-x/v\tau_i} \right) \tag{2-16}$$

where $K_i = N_a \sigma_i^* v N_b \tau_i$ and $x=vt$.

With the geometry of the system like that shown in Fig. 2-1 the total number of photons J_{ij} emitted from the shaded section is given by

$$\begin{aligned} J_{ij} &= \int_L^{L+\ell} A N_{bi} A_{ij} \, dx \\ &= (I_b/e) N_a \ell \tau_i A_{ij} \sigma_i^* h_i(L) \end{aligned} \tag{2-17}$$

where $I_b = e A N_b v$; the current of the beam,

e ; charge of the electron,

A ; cross sectional area of the beam,

and $h_i(L) = \left(1 - (v\tau_i/\ell) \left(1 - e^{-\ell/v\tau_i} \right) e^{-L/v\tau_i} \right)$.

For $L \gg \ell$, $h_i(L) \simeq g_i(L) = \left(1 - e^{-L/v\tau_i} \right)$.

Therefore, the expected signal S(L) from the photon detection system is given by

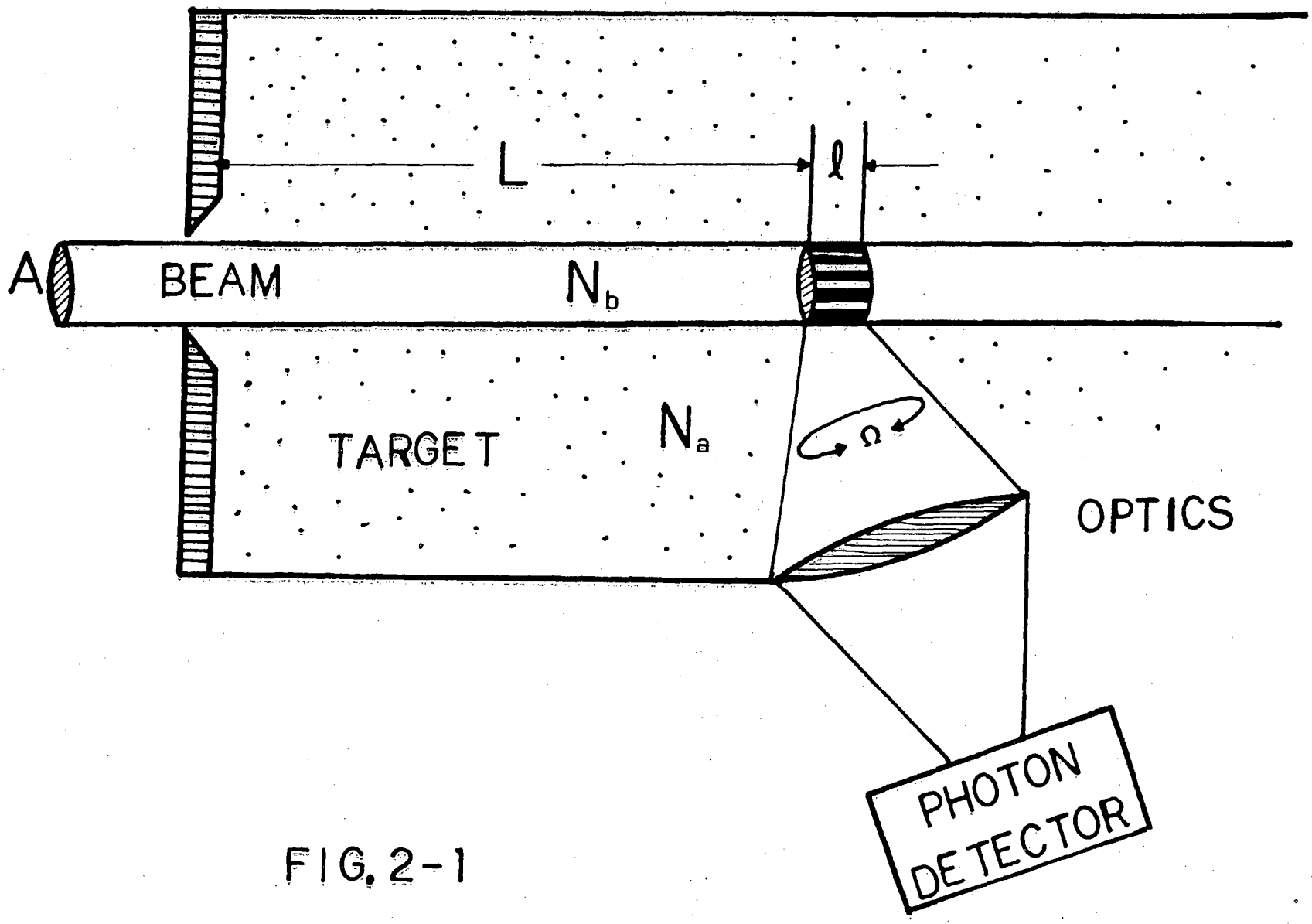

FIG. 2-1

XBL 829-11772

$$S(L) = \sum_i (\Omega/4\pi)\ T\ Q\ J_{ij}(L) \qquad (2\text{-}18)$$

where Ω ; observational solid angle

T ; transmittance of the optical system

Q ; quantum efficiency of the photon detector.

Finally $S(L)$ can be expressed as

$$S(L) = D\ (\ I_b/e\ )\ N_a\ \ell \sum_i A_{ij}\ \tau_i\ g_i(L) \qquad (2\text{-}19)$$

where D is the detection efficiency defined as

$$D = (\Omega/4\pi)\ Q\ T \qquad (2\text{-}20)$$

So far the cascading effect has been neglected; including it changes equation (2-15) to

$$\frac{dN_{bi}}{dt} = (I_b/e)\ \sigma_i^*\ N_a - (1/\tau_i)\ N_{bi} + \sum_{k>i} A_{ki} N_{bk} \qquad (2\text{-}21)$$

This is a 1st order self consistent differential equation. Since the excitation cross section follows n^{-3} law and A_{ki} becomes smaller for the higher k the magnitude of the self-consistent term should be small. Hence, a perturbation method can be applied to solve this equation. The solution including the first order term can be written as

$$N_{bi} = N_{bi}^0 + N_{bi}^1 \qquad (2\text{-}22)$$

then the equation for the zeroth order is given by

$$\frac{dN_{bi}^{0}}{dt} = (I_b/e) N_a \sigma_i^* - (1/\tau_i) N_{bi}^{0} \qquad (2\text{-}23)$$

which has the same form with equation (2-15). Therefore the zeroth order solution can be written as

$$N_{bi}^{0} = K_i \; g_i(x) \qquad (2\text{-}24)$$

The equation for the first order term is then

$$\frac{dN_{bi}^{1}}{dt} = - (1/\tau_i) N_{bi}^{1} + \sum_{k>i} A_{ki} \; N_{bi}^{0} \qquad (2\text{-}25)$$

In order to solve this equation one starts with a homogeneous part of the solution

$$N_{bi}^{1h} = \alpha_i \; e^{-t/\tau_i} \qquad (2\text{-}26)$$

and a particular part of the solution

$$N_{bi}^{1p} = \sum_{k>i} (\beta_k A_{ki} K_k (1 - e^{-t/\tau_k}) + \gamma_k) \qquad (2\text{-}27)$$

Boundary conditions lead to

$$\beta_k = \tau_k \tau_i / (\tau_k - \tau_i)$$

$$\gamma_k = K_k A_{ki} \tau_i^2 / (\tau_k - \tau_i)$$

$$\alpha_i = - \sum_{k>i} \gamma_k$$

The combination of these constants leads to a final form as

$$N_{bi}^1 = \tau_i \sum_{k>i} \frac{A_{ki} K_k}{(\tau_k - \tau_i)} (\tau_k g_k(x) - \tau_i g_i(x)) \quad (2\text{-}28)$$

Only the single collision system has been treated to this point, but the multiple collision system will be presented also. For the real experiment the simplest multiple collision system is the case of the target molecule dissociative excitation by protons. The equations for other cases have been developed and they will be presented in Appendix B. Consider the two component system including H^+ and H^0 and neglecting H^-. The relative density of H^0 and H^+ in the projectile beam can be denoted by y_0 and y_+ . Neglecting the excitated state effect one can write the equation for y_0 and y_+ as

$$y_0 + y_+ = 1 \quad (2\text{-}29)$$

and

$$\frac{dy_0}{d\pi} = - \sigma_{01} y_0 + \sigma_{10} y_+ \quad (2\text{-}30)$$

where $\pi = N_b x$ and σ_{10} and σ_{01} are charge exchange cross sections. The boundary condition is given at $\pi = 0$ where $y_0 = 0$ and $y_+ = 1$. Then the solutions are

$$y_+ = F_{1\infty} + F_{0\infty} e^{-\sigma_T \pi} \tag{2-31}$$

and

$$y_0 = F_{0\infty} (1 - e^{-\sigma_T \pi}) \tag{2-32}$$

where $\sigma_T = \sigma_{10} + \sigma_{01}$, $F_{0\infty} = \sigma_{10}/\sigma_T$ and $F_{1\infty} = \sigma_{10}/\sigma_T$.

The light intensity from the target, J is given by

$$J = \int_L^{L+\ell} N_a A v N_b (\sigma_+^* y_+ + \sigma_0^* y_0) dx \tag{2-33}$$

where σ_+^* and σ_0^* are dissociative excitation cross sections of H_2 by H^+ and H^o beam.

For $L >> \ell$ this can be simplified as

$$J \simeq N_a A v N_b (\sigma_+^* (F_{1\infty} + F_{0\infty} e^{-\sigma_T N_a L}) + \sigma_0^* F_{0\infty} (1 - e^{-\sigma_T N_a L})) \cdot \ell \tag{2-34}$$

C. Polarization

Studying the interaction between the beam and target, one can assume the system to be azimuthally symmetric due to the cylindrical geometry of the beam. Assigning the beam axis as the z-axis and observing along the axis which has an angle θ with the z-axis, $I_{\perp}(\theta)$ is defined as the local relative intensity of photons which have their electric fields normal to the z-axis and $I_{\parallel}(\theta)$ as the intensity of photons with the electric fields parallel to the z-axis as shown in Fig. 2-2. With this geometry, the polarization at an angle θ with the z-axis can be specified as

$$P(\theta) = \frac{I_{\parallel}(\theta) - I_{\perp}(\theta)}{I_{\parallel}(\theta) + I_{\perp}(\theta)} \qquad (2\text{-}35)$$

To derive $P(\theta)$ in terms of cross sections one starts with the quantum mechanical form of dipole radiation under the assumption that the diploe process is dominant in the radiative transition. The equation for the dipole radiation is given by[42]

$$I(\Omega, \hat{e}_j) = n'(e^2/2\pi c^3)\omega^4 |\hat{e}_j \cdot \langle N'|\vec{r}|N\rangle|^2 \qquad (2\text{-}36)$$

where $I(\Omega, \hat{e}_j)$ is the intensity of radiation in the direction of Ω which has the electric field along the unit vector $\hat{e}_j$ and $|N\rangle$ is the ket for the higher energy quantum state and $|N'\rangle$ is that for lower energy quantum state,

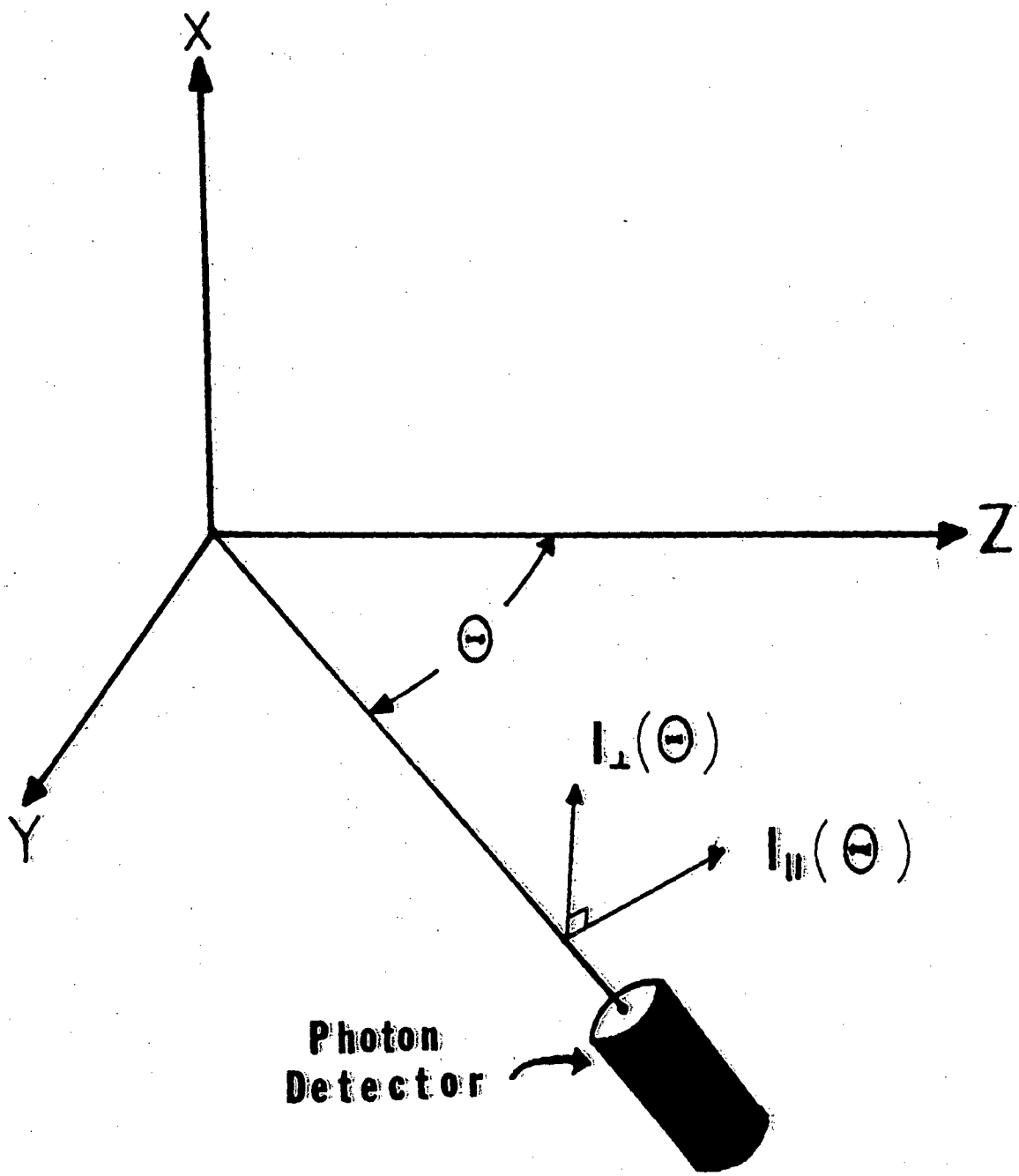

XBL 829-11773

FIG. 2-2

where n' represents the density of the excited state N, $\vec{r}$ the length and direction of the individual dipole, and ω the angular frequency of the radiation. Since the radial part of the dipole transition doesn't contribute to the polarization only the angular part is of importance. From this knowledge the previous equation can be simplified to

$$I(\Omega, \hat{e}_j) = \sum_{N,N'} K \sigma_N \, | \hat{e}_j \cdot \langle N' | \vec{r} | N \rangle |^2 \quad (2\text{-}37)$$

where $K = e^2\omega^4 / 2\pi c^3 f(x)$,

and σ_N is the cross section for the state $|N\rangle$ and $f(x)$ is a function of the travel distance of the beam into the target under the single collision condition.

The equations for $I_\perp(\theta)$ and $I_\parallel(\theta)$ are

$$I_\perp(\theta) = \sum_{N,N'} K \sigma_N \, | \hat{x} \cdot \langle N' | \hat{r} | N \rangle |^2 \quad (2\text{-}38)$$

$$I_\parallel(\theta) = \sum_{N,N'} K \sigma_N \, |(- \cos\theta \, \hat{y} + \sin\theta \, \hat{z}) \cdot \langle N' | \vec{r} | N \rangle |^2 \quad (2\text{-}39)$$

But

$$\begin{aligned} \hat{x} \cdot \hat{r} &= - r \sqrt{4\pi/3} \, (Y_{11} + Y_{1-1})/\sqrt{2} \\ \hat{y} \cdot \hat{r} &= - r \sqrt{4\pi/3} \, (Y_{11} - Y_{1-1})/\sqrt{2}i \\ \hat{z} \cdot \hat{r} &= r \sqrt{4\pi/3} \, Y_{10} \end{aligned} \quad (2\text{-}40)$$

The quantum number N represents a set of quantum numbers

(n,l,m) without spin consideration, where n is the principal quantum number, ℓ the angular quantum number and m the magnetic quantum number. Then in the wave function representation $\langle N' | \hat{x}\cdot\vec{r} | N\rangle$ can be written as

$$\begin{aligned}\langle N' | \hat{x}\cdot\vec{r} | N\rangle &= \int d^3r \; \Psi_{n'\ell'm'} (\hat{x}\cdot\vec{r}) \; \Psi_{n\ell m} \\ &= \int dr \; r^2 \; R_{n'\ell'} \; R_n \quad \int d\Omega \; Y_{\ell'm'}(\hat{x}\cdot\vec{r}) \; Y_{\ell m} \\ &\equiv g \; \langle Y_{\ell'm'} | \hat{x}\cdot\vec{r} | Y_{\ell m} \rangle \qquad (2\text{-}41)\end{aligned}$$

where Ψ is the wave function, R is the radial part of that and $g = \sqrt{4\pi/3} \int dr \; r^2 \; R_{n'\ell'} \; R_{n\ell}$.

Therefore

$$I_\perp(\theta) = K' \sum_{N,N'} \sigma_N/2 \; | \langle Y_{\ell'm'} | Y_{11} + Y_{1-1} | Y_{\ell m}\rangle |^2 \qquad (2\text{-}42)$$

$$I_\parallel(\theta) = K' \sum_{N,N'} \sigma_N | \cos\theta \langle Y_{\ell'm'} | \frac{Y_{11} + Y_{1-1}}{\sqrt{2}\, i} | Y_{\ell m}\rangle + \sin\theta \langle Y_{\ell'm'} | Y_{10} | Y_{\ell m}\rangle |^2 \qquad (2\text{-}43)$$

where $K' = K g^2$.

For the 3s → 2p transition

$$I_\perp(\theta) = K' \sum_{N,N'} \sigma_N = I_\parallel(\theta) \qquad (2\text{-}44)$$

Thus the 3s → 2p transition is not polarized. For the 3p → 2s transition one considers the m=+1, m=0 and m=-1 states

separately. Because of the symmetry between clockwise and counter-clockwise rotations, there should be no difference between m=+1 and m=-1 states. Defining their cross sections as σ_{1+}, σ_{10} and σ_{1-} and setting $\sigma_{1+} = \sigma_{1-} = \sigma_{11}$, then

$$\begin{aligned} I_{\perp}(\theta) &= K'\sigma_{11} \\ I_{\parallel}(\theta) &= K'(\cos^2\theta\sigma_{11} + \sin^2\theta\sigma_{10}) \end{aligned} \tag{2-45}$$

Therefore the polarization is given by

$$P(\theta) = \frac{\sin^2\theta\,(\sigma_{10} - \sigma_{11})}{\sigma_{10}\sin^2\theta + \sigma_{11}(1+\cos^2\theta)} \tag{2-46}$$

For the 3d → 2p transition the situation is more complicated. Defining σ_{22}, σ_{21} and σ_{20} as the cross sections for m=2,1 and 0 states and by the same symmetry argument as before the equations for $I_{\parallel}$ and $I_{\perp}$ are

$$I_{\parallel}(\theta) = K' \sum_{m,m'} \sigma_{2m} |(\cos\theta/\sqrt{2}i) < Y_{1m'}|Y_{11} - Y_{1-1}|Y_{2m}> + \sin\theta <Y_{1m'}|Y_{10}|\ Y_{2m}>|^2 \tag{2-47}$$

$$I_{\perp}(\theta) = \frac{K'}{2} \sum_{m,m'} \sigma_{2m} |<Y_{1m'}|Y_{11} + Y_{1-1}|\ Y_{2m}>|^2 \tag{2-48}$$

Table (2-1) has been prepared for these values. Then the final equations defining the intensities are

m	m'	$40\pi\langle Y_{1m}, \lvert Y_{11}\rvert Y_{2m}\rangle$	$40\pi\langle Y_{1m}, \lvert Y_{1-1}\rvert Y_{2m}\rangle$	$40\pi\langle Y_{1m}, \lvert Y_{10}\rvert Y_{2m}\rangle$
2	1	12	0	0
1	0	6	0	0
0	1	0	2	0
0	0	0	0	8
0	-1	2	0	0
-1	0	0	6	0
-2	-1	0	12	0

TABLE (2-1)

$$I_{\perp}(\theta) = 2\,K'\,(\;6\sigma_{22} + 3\sigma_{21} + \sigma_{20}\;)$$

--------(2-49)

$$I_{\parallel}(\theta) = I_{\perp}(\theta)\cos^2\theta + 8\,K'\,\sigma_{20}\sin^2\theta$$

Finally the polarization is given by

$$P(\theta) = \frac{\sin^2\theta(\;\sigma_{20} - (\;2\sigma_{22} + \sigma_{21}\;))}{\dfrac{(\;2 + 3\sin^2\theta)}{3}\;\sigma_{20} + (1+\cos^2\theta)(2\sigma_{22}+\sigma_{21})}$$

----------(2-50)

CHAPTER 3

Apparatus

A. Monochromator and Other Optics

To increase the detection efficiency a Littrow type monochromator[43] was designed and constructed in this laboratory. The basic structure of this type monochromator was very simple. It had two slits, one large grating with some adjustment equipments, one large achromatic lens and a 90° 1"x1" prism. A more detailed description is presented in Appendix A.

The optics were designed to give the largest observation solid angle. Two lenses with 10 cm focal length and 4 cm diameter were used to give a one-to-one target image on the slit area of the monochromator. One lens was mounted on a Varian flange which had an optical window, with a 10 cm distance from the target. Between these two lenses was positioned a linear polarizer and a half wave plate. Since the monochromator had the greater sensitivity to the horizontally polarized light, in the measurement of the vertical component the polarization of light was rotated by 90° to give it a horizontal polarization. The physical idea of this arrangement is described below.

Consider the geometry shown in Fig. 3-1. With Jones matrix notation[44] the initially vertically polarized light is represented by $(1 , 1)^{t}$ and the half wave plate as

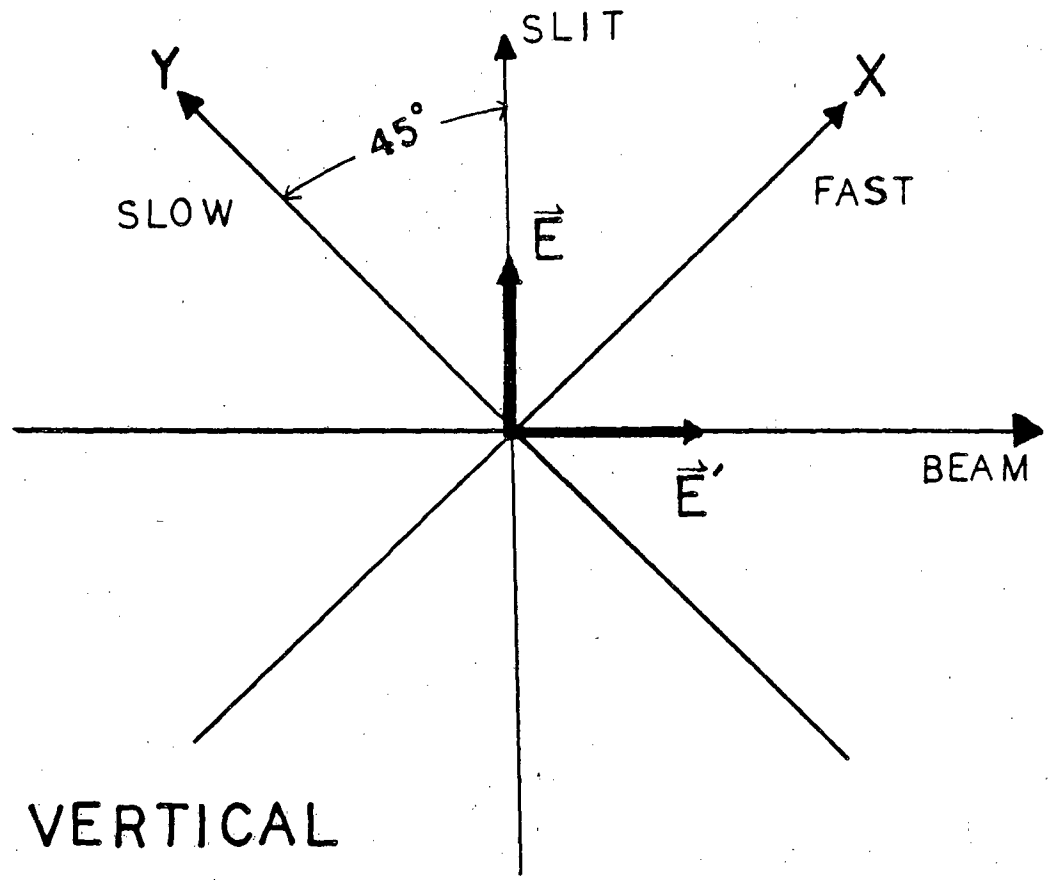

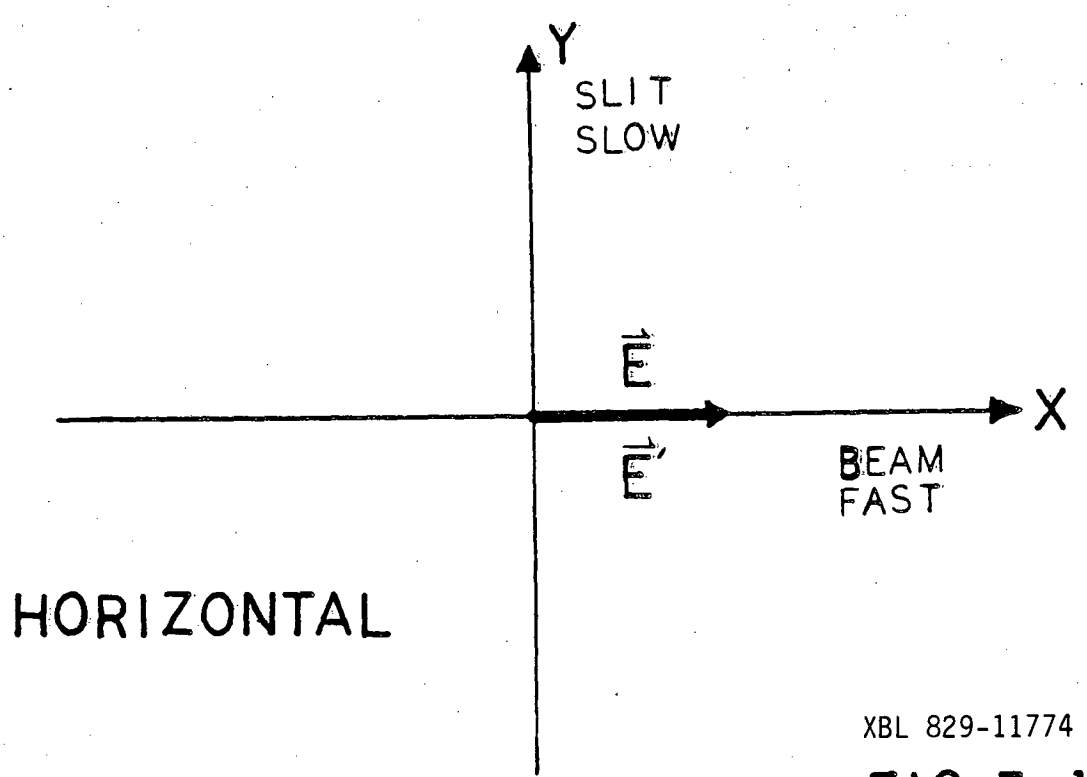

XBL 829-11774

FIG. 3-1

$$\begin{bmatrix} 1 & 0 \\ 0 & -1 \end{bmatrix} \tag{3-1}$$

If the fast and slow axis of the half wave plate is set as shown in Fig. 3-1, through the half wave plate the state of polarization is transformed according to the following equation and the result of which is horizontally polarized light.

$$\begin{bmatrix} 1 & 0 \\ 0 & -1 \end{bmatrix} \cdot \begin{bmatrix} 1 \\ 1 \end{bmatrix} = \begin{bmatrix} 1 \\ -1 \end{bmatrix} \tag{3-2}$$

Practically there is a certain attenuation factor due to the finite transmittance of the half wave plate. To measure horizontally polarized light, the fast and slow axis should be set parallel to the slit and the beam direction. In this geometry the incident light is represented as $(1 , 0)^t$ and the half wave plate as

$$\begin{bmatrix} 1 & 0 \\ 0 & -1 \end{bmatrix} \tag{3-3}$$

Therefore, the final result is given by

$$\begin{bmatrix} 1 & 0 \\ 0 & -1 \end{bmatrix} \cdot \begin{bmatrix} 1 \\ 0 \end{bmatrix} = \begin{bmatrix} 1 \\ 0 \end{bmatrix} \tag{3-4}$$

i.e. there is no rotation effect at all. In practice the relative transmittances of the horizontal axis and vertical

axis for the optical system were needed and measured with an unpolarized white light source.

After the monochromator one 5 cm focal length lens was used for one-to-one imaging of the exit slit image onto the window of the photomultiplier tube.

B. Ion Source and Accelerator

The electrostatic accelerator used in this research was a 150 kV TNC (Texas Nuclear Corporation) equipped with an R.F. ion source. It had extendable high voltage capability with a SF_6 gas system, up to 250 kV. Due to the design of this accelerator no usuable beam current was obtainable below 10 kV. For lower energy beam a number of stacks for electrostatic acceleration were used for electrostatic focusing by the use of clippleads. The lower the beam energy was the more clippleads were used. By that way the beam current was increased.

The ion source bottle was a typical commercial R.F. type made of quartz. The position of the R.F. rings was adjusted to give maximum current. With a proton beam, an aluminium canal was used to produce maximum proton species. With H_2^+ and H_3^+ beam a nickel canal was used. For H_2^+ beam a low stack gas pressure ($\sim 3 \times 10^{-6}$ Torr) and for H_3^+ beam a relatively high stack gas pressure ($\sim 8 \times 10^{-6}$ Torr) gave the best results.

After acceleration the beam was focused by two eletrostatic quadrupole lenses oriented at 90° to each other. The focused beam entered a steering plate section with two vertical sets of steering plates. The beam then entered a bending magnet, was momentum analyzed, and was bent at an angle of approximately 15°. The purity of the beam was ensured by using the Hall-probe signal to select the correct mass

ions to be sent to the target chamber. The schematic diagram of the whole system is given in Fig. 3-2.

The beam then passed through the first collimator of the gas cell which had a 4 inch diameter diffusion pump used for pumping out. Then the beam entered the gas target whose length was defined being from the observation region to the movable 1/16 inch diameter aperture system. The beam then impinged on the pyroelectric detector.

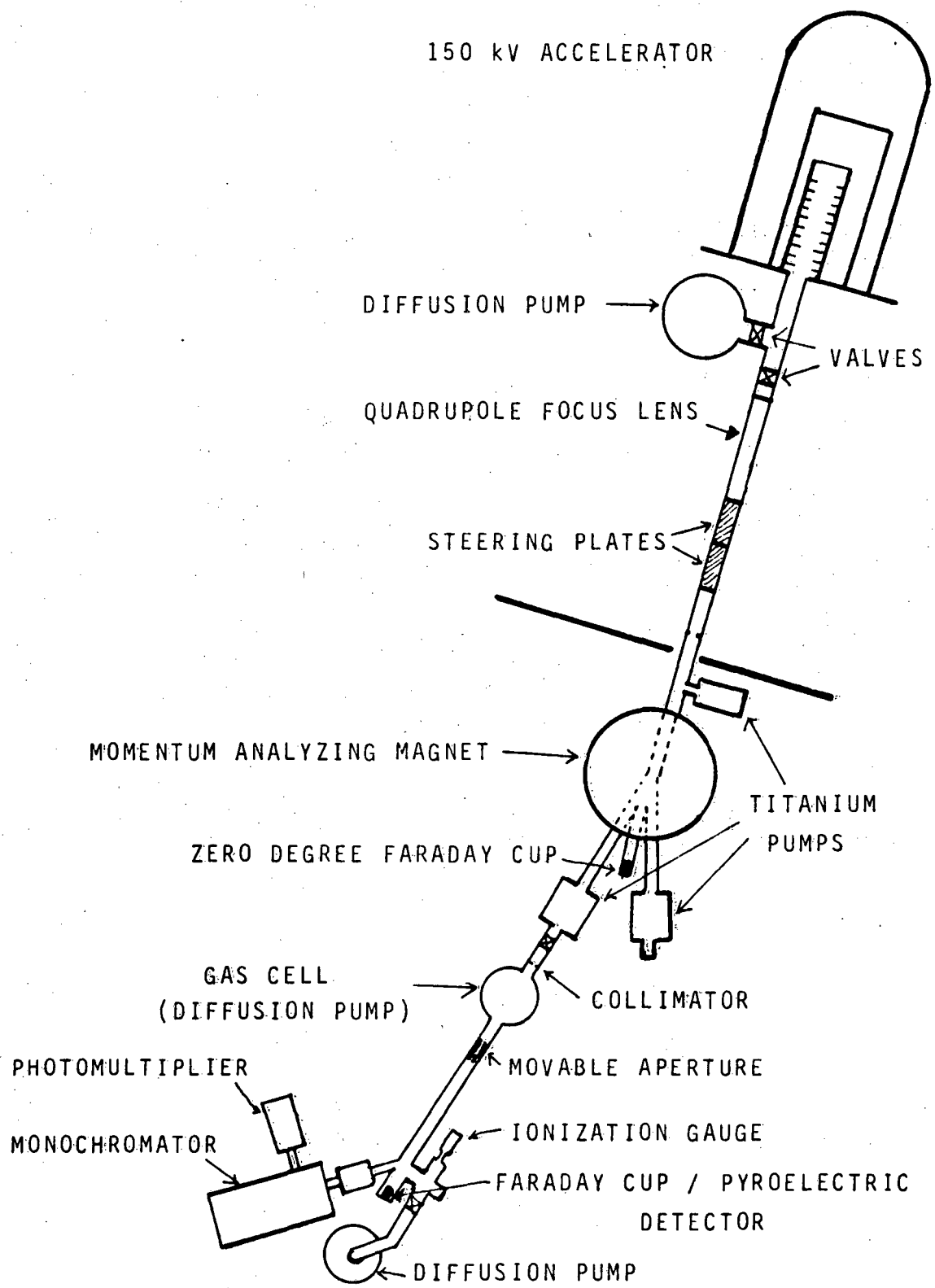

XBL 829-11775

FIG. 3-2

C. Target System

The target chamber was basically made of a 34 inch length 1½ inch diameter stainless steel pipe. As shown in Fig. 3-3 there were two additionally attached 1½ inch diameter stainless steel pipe sections with angles 54.8^{o} and 90° to the main pipe section. The 54.8^{o} angled section was designed for two purposes. One was to give sufficient Doppler shift of light for separation of the radiation of fast particles from that of slow particles; the other was to simplify the polarization correction factor for cross sections. The 90° angled section was used for pumping out the residual gas and pressure measurement of the main target chamber. This section was connected to an ionization gauge, a capacitance manometer (Barocel) and a 4 inch diameter diffusion pump through a hand operated valve and 3/8 inch aperture. The ionization gauge was used for monitoring the zero point drifting of the Barocel and approximate residual background gas pressure measurements. The 4 inch diameter diffusion pump was used to reduce the back-ground pressure and to help to pump out during outgassing. The residual gas pressure was normally less than $2x10^{-6}$ Torr during the experimental procedure. The Barocel was calibrated by an oil manometer before usage. The optical window which was connected to 54.8^{o} angled section was made of fused silica.

To provide minimum light reflection, every surface inside

the target chamber was blackened with Aquadag (micro-graphite in aquous base) dissolved in ethyl alcohol.

The movable aperture system had two o-rings to minimize loss of gas from the target chamber. Pumping out was through a hole at the center of the aperture system. The schematic is presented in Fig. 3-4.

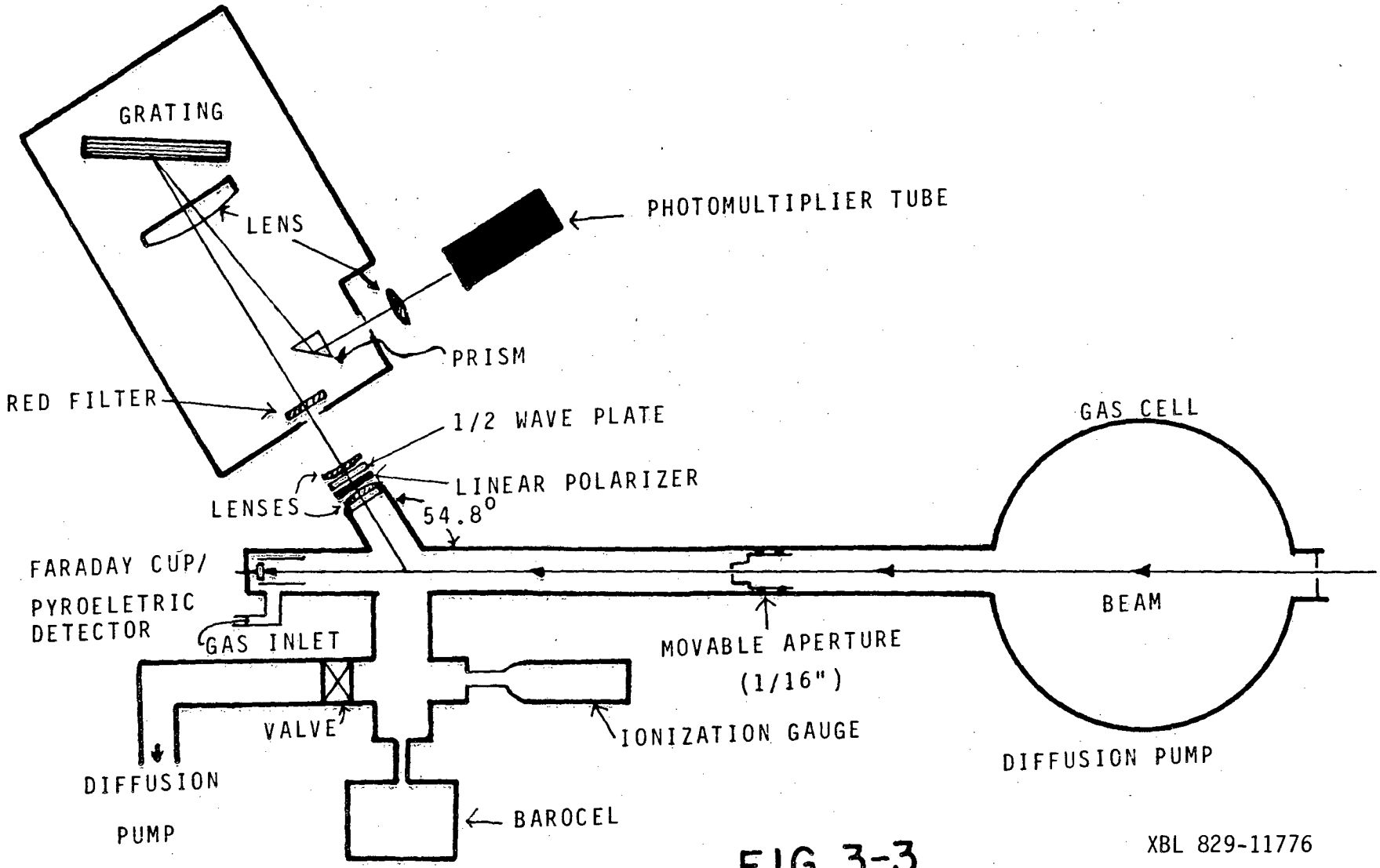

FIG. 3-3

XBL 829-11776

FIG.3-4

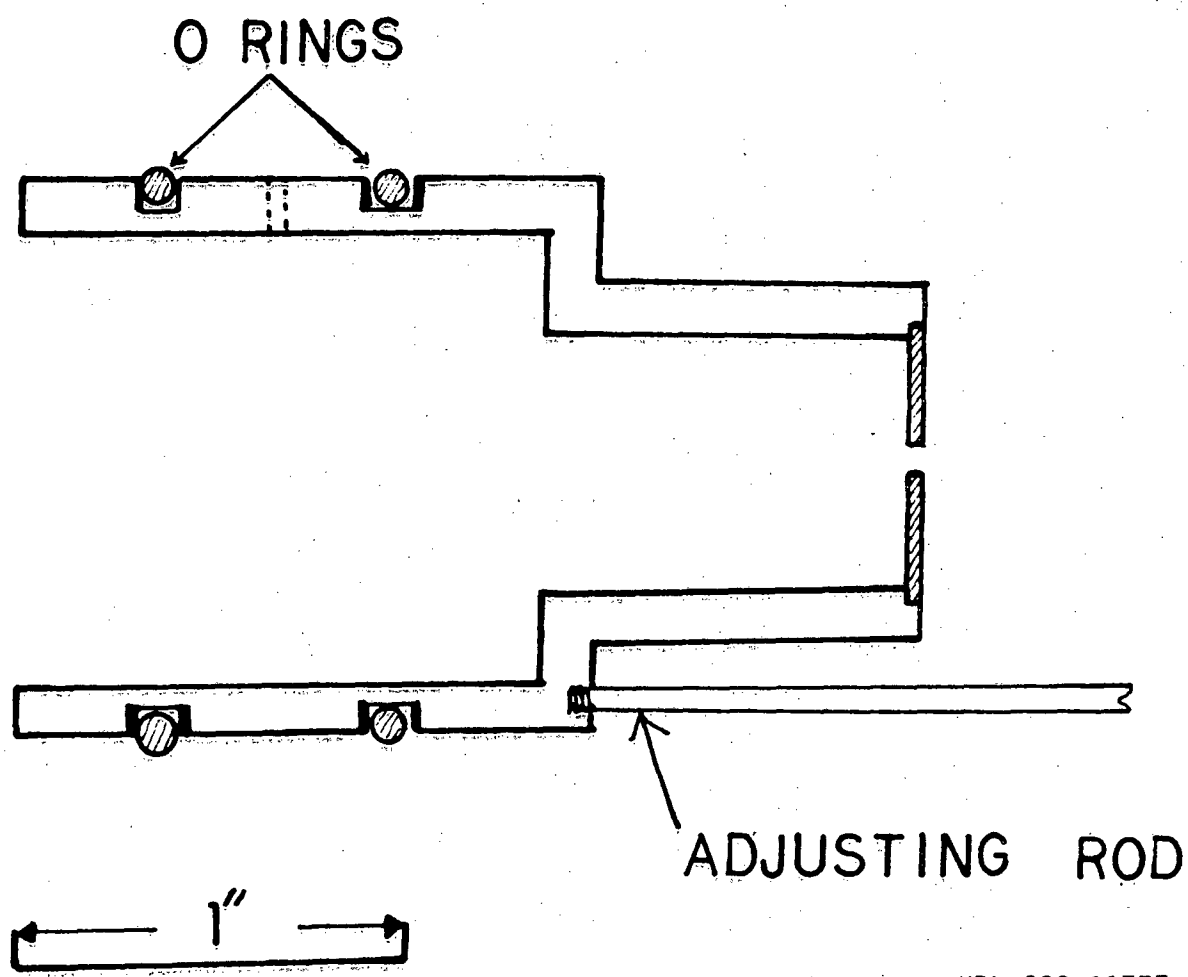

XBL 829-11777

D. Detector

a. Photomultiplier Tube

A photomultiplier tube (EMI 9862A) was used for photon detection and the statistics was based on counting. The main limitation of the photon detection system came from the dark current due to thermionic electrons emitted by the photo cathode, and poor quantum efficiency in the red light region. To decrease the dark current the photomultiplier tube was cooled to -25°C and only a small center part of the photo-cathode (1 cm diameter)was used. The high voltage for the photo-cathode was then selected for the best signal-to-noise ratio and pulse-height distribution. About 5% quantum efficiency and about 5 count/sec dark count allowed about 100 photon resolution of the photomultiplier tube in a second.

The pulse shapes from the pre-amp and the main-amp are shown in Fig. 3-5. The typical pulse height distribution is also shown in Fig. 3-6. From the pulse rise time of the pre-amp (~50 μsec) a nonlinear effect of the photon detection system can be expected for count rates of more than 10^{4}count/sec. This was experimentally verified in Chapter 4-A.

b. Pyroelectric Detector / Faraday Cup

The incident beam current was measured with a pyroelectric detector connected to lock-in amplifier (Princeton Applied Research) model number H-R-8 and was normalized to the

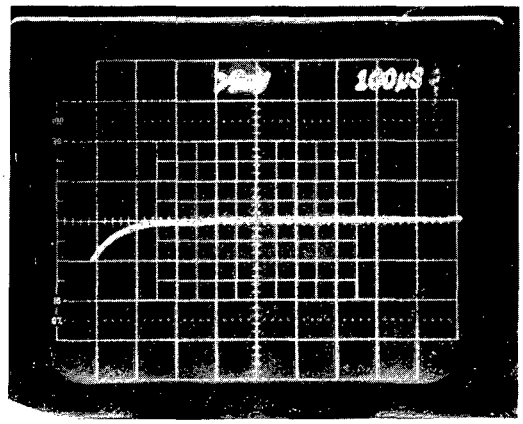

SIGNAL FROM PRE-AMP

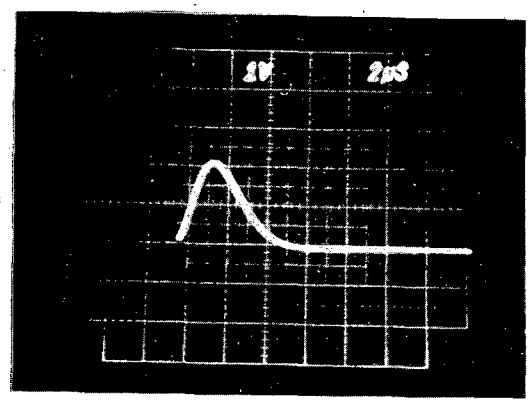

XBB 829-8375

SIGNAL FROM MAIN AMP

Fig. 3-5

TYPICAL PULSE HEIGHT SPECTRUM

NUMBER OF PULSES

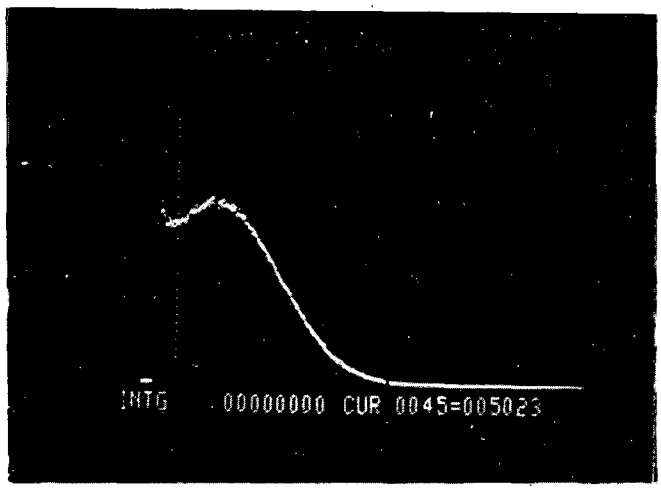

PULSE HEIGHT

XBB 829-8374

FIG. 3-6

Faraday cup signal. The schematic diagram of this is shown in Fig.3-7. The characteristics of the pyroelectric detector is known fairly well[45] and a brief explanation is given below. The detector consisted of a 2.5 cm diameter polarized lead zirconate titanate ceramic disk which was silvered on both sides to provide electrical contact. The contact resistance between the surface and the electric contactor was confirmed to be much less than 1 ohm with an ohm-meter. The ion beam was chopped by electrostatic plates and an alternating signal was obtained from the detector. This had two advantages, number one was that the dark current of the photomultiplier tube could be discriminated from the real signal, and number two was that it simplified the amplification and interpretation of the signal and permitted an increased signal to noise ratio by measuring the signal with a phase-sensitive amplifier. Fig. 3-8 shows triggering signal used for the phase sensitive detection. Often in the measurement of low power signal the acoustical and electrical noise problems occur, but with phase sensitive detection these were negligible. The typical signal from the lock-in amplifier is shown in Fig. 3-9 and the detailed electronics are shown in Fig. 3-10. Since it was desired that the cross sections should be absolute, normalization of the pyroelectric detector signal was required. The Faraday cup was constructed with the pyroelectric crystal as an integral part and the secondary electron loss was prevented by the use of magnetic suppression.

PYROELECTRIC DETECTOR / FARADAY CUP

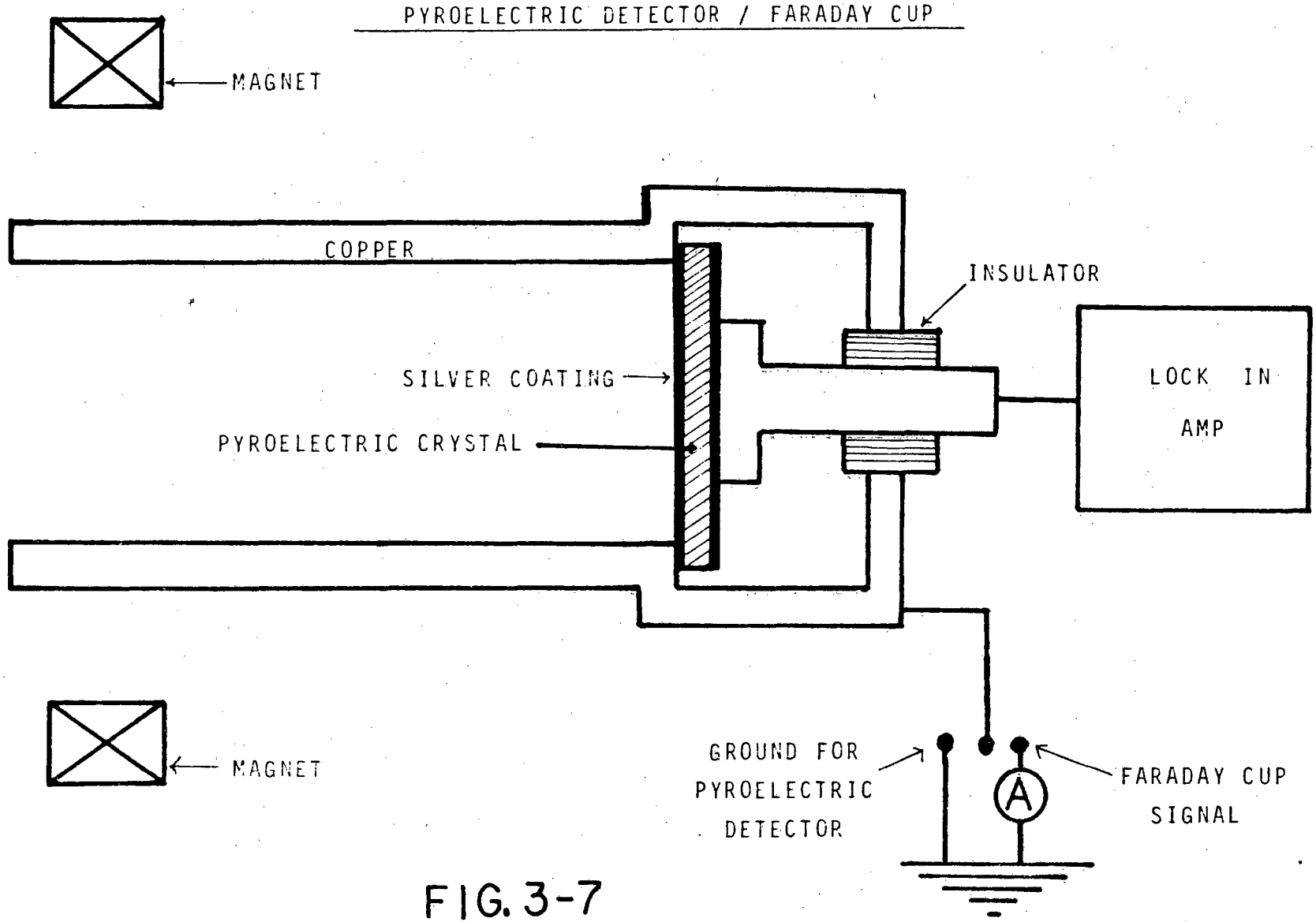

FIG. 3-7

XBL 829-11778

TRIGGERING SIGNAL

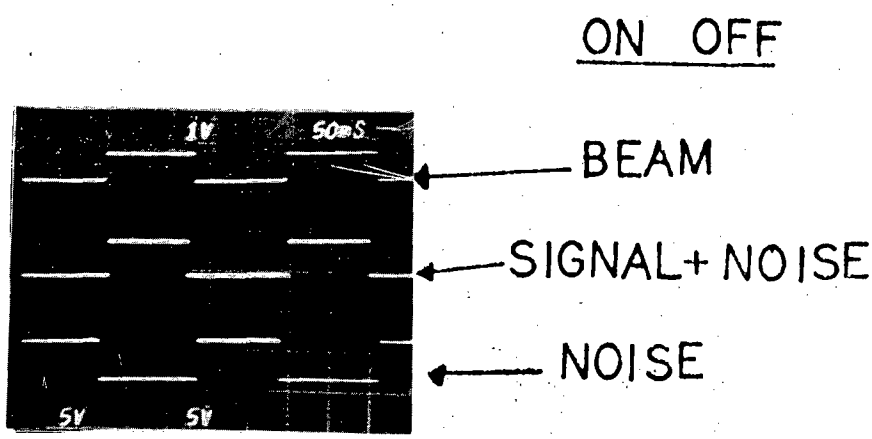

XBB 829-8376

FIG. 3-8

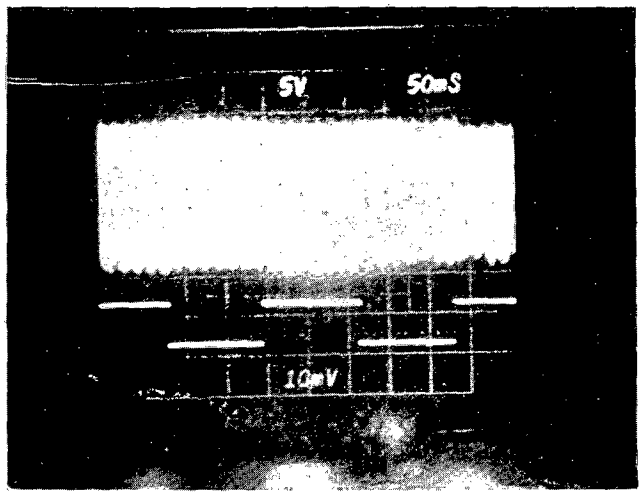

RAW SIGNAL FROM PYROELECTRIC CRYSTAL

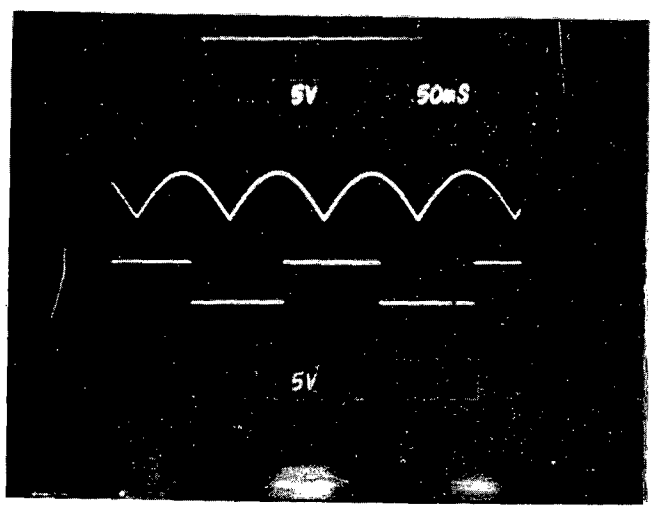

XBB 829-8377

UPPER : SIGNAL FROM LOCK IN AMP

LOWER : TRIGGERING SIGNAL FOR BEAM

FIG. 3-9

Data Aquisition System

PA	;	Pre Amplifier
PG	;	Pulse Generator
PMT	;	Photo-Multiplier Tube
SCA	;	Single Channel Analyzer
PHA	;	Pulse Height Analyzer
PD	;	Pyroelectric Detector
IFC	;	Inter-Face Controller
CI	;	Counter-Integrator
PSA	;	Phase Sensitive Amplifier
DCI	;	Digital Current Integrator
HV	;	High Voltage
SP	;	Steering Plate

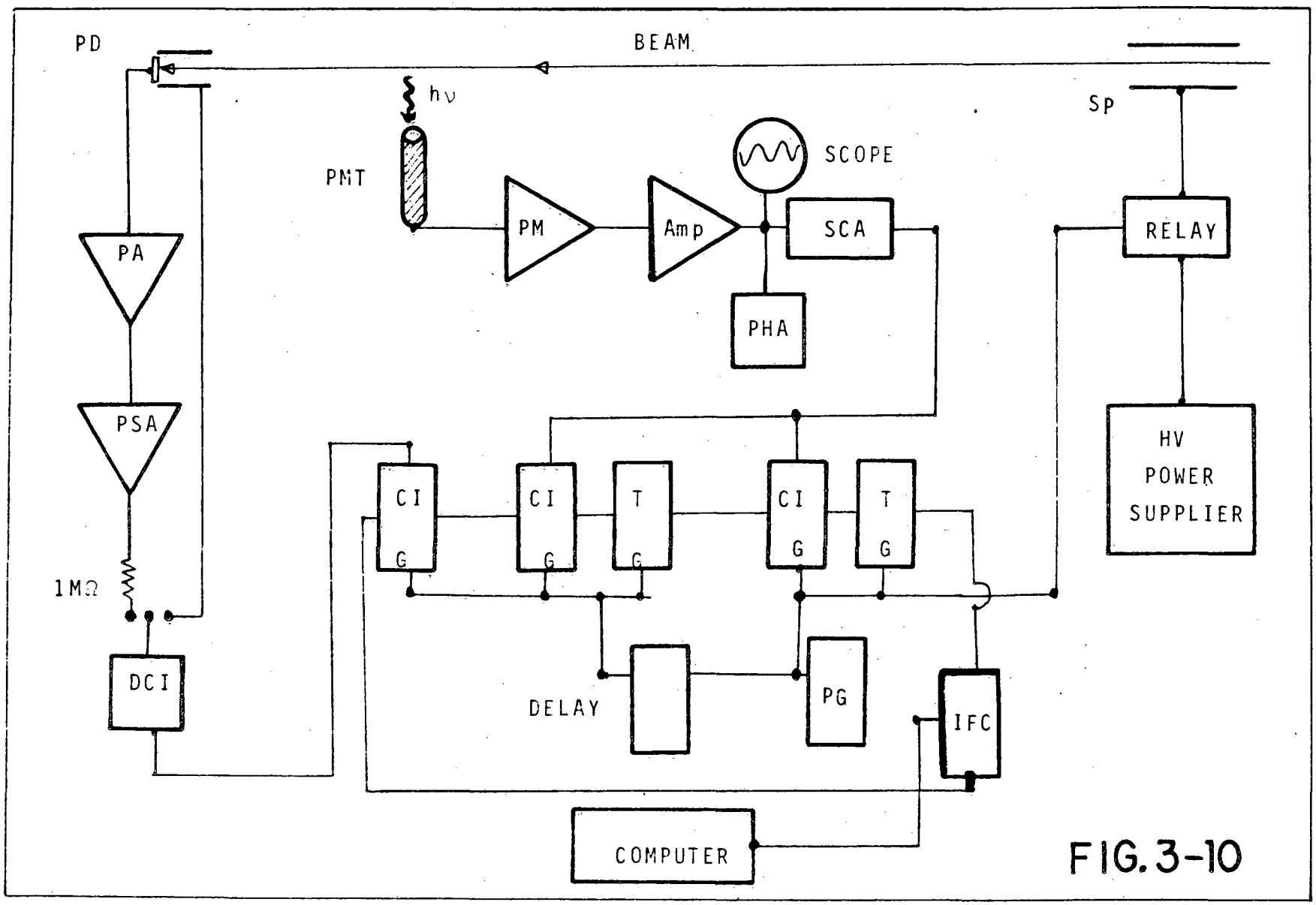

FIG. 3-10

XBL 829-11779

The Faraday cup was connected directly to an Ortec 439 Digital Current Integrator which was also used for measurement of the signal from the pyroelectric detector. Ortec 770 Counters and 771 Timer-Counters were used for counting and timing.

To measure K which was defined as the ratio of Faraday cup signal to pyroelectric detector signal the gas target density was reduced to zero and the signal from the Faraday cup was integrated during 20 to 30 seconds. The signal from the pyroelectric detector was then integrated during the same amount of time as before. After one measurement, K was then measured in the reverse way. The accuracy of K depended on the stability of the current. In the normal case the standard error was less than a few percent. In all measurements the power of the incident ion beam exceeded the levels where one could expect problems.

CHAPTER 4

Procedure and Data Analysis

A. Absolute Optical Calibration

Absolute optical calibration requires calibration of the sensitivity of the total detection system to the best known standard photon source. The best known standard photon source is a standard tungsten ribbon lamp. Since the photon detection system used in this work was extremely sensitive, neutral filters were required for reducing the light intensity. Attention was also given to the linearity of the detection system.This is shown in Fig. 4-1 indicating the range of response for which linearity could be expected. Every measurement was limited to this range.

The equation for the relation between the known emissivity of the tungsten standard lamp and the detection efficiency of the system can be developed as follows. Define E_t as the number of photons which come from unit area of the tungsten filament within a unit solid angle and unit wavelength per second. Then the number of counts per second, S, from the detector due to the standard lamp is

$$S = D (4\pi E_t A_m \Delta\lambda) \qquad (4\text{-}1)$$

where A_m denotes the area of the tungsten filament to be seen by the monochromator (the slit area of the monochro-

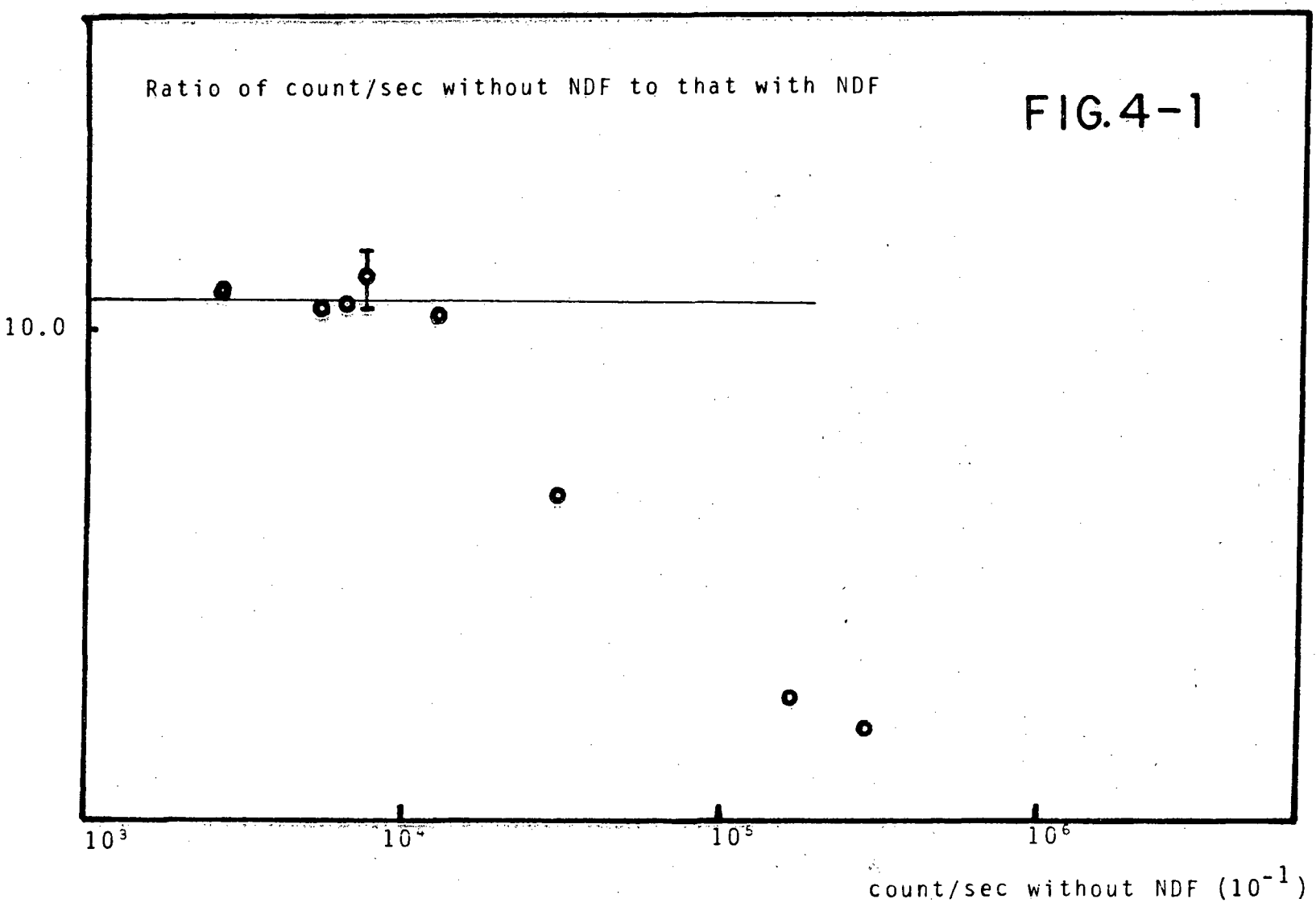

FIG.4-1

XBL 829-11780

mator because a one-to-one image onto the slit area was used). $\Delta\lambda$ is the resolution of the monochromator and D is the detection efficiency of the system which includes the detection solid angle and the quantum efficiency of the photon detector. Therefore D is given by

$$D = S / 4\pi E_t A_m \Delta\lambda \qquad (4\text{-}2)$$

The next process is to relate the excitation cross section to the number of counts per second from the detector. At equilibrium (i.e. without considering the distance dependency of the emission into the target) the total number of photons per second, N_p, come from a length ℓ and density N_a of the target due to the current I_b of the beam is given by

$$N_p = N_a \sigma (I_b/e) \ell \qquad (4\text{-}3)$$

where e is the charge of an electron and σ is the excitation cross section. On the other hand the number of counts per second, N_s, from the photon detector due to N_p is

$$N_s = D N_p \qquad (4\text{-}4)$$

Therefore, from the equations (4-2), (4-3) and (4-4) the excitation cross section can be expressed as

$$\sigma = \left(\frac{4\pi\ E_t\ \Delta\lambda}{S}\right)\left(\frac{A_m}{\ell}\right)\ \left(\frac{e}{I_b}\right)\left(\frac{1}{N_a}\right)\ N_s \qquad (4\text{-}5)$$

From this equation parameters which are needed for absolute optical calibration can be determined.

To ensure the monochromator slit was completely covered by the image of the tungsten strip, a 4.5±0.1 mm length center portion of the slit was used. By that way A_m was given by ℓ x (4.5±0.1) mm^2 and the width of the slit ℓ canceled out automatically in the equation (4-5). $\Delta\lambda$ was given by either the spectral line from the Doppler unshifted target emission, or that from H_2 discharge lamp. The scale unit of the monochromator was calibrated by Ne and H_2 discharge lamps. The spectrum from Ne lamp is shown in Fig. 4-2.

S required care in its measurement. Using neutral filters and with the detector in its mode, it was determined that the detector was linear to 10^4 count/sec. Above that rate, Piling up of the pulses due to a pulse rise time of the order of 0.1 msec caused nonlinearity as shown in Fig. 4-1. S was measured with a known current for the tungsten ribbon filament lamp and with a combination of neutral density filters to give an allowable count rate. The current of the standard lamp was then decreased to give a reasonable count rate such as 100 count/sec . This was integrated more than 100 second to give a less than 1 % standard counting error. From the above procedure the relative ratio between those amounts of filament current was developed with less than 1 %

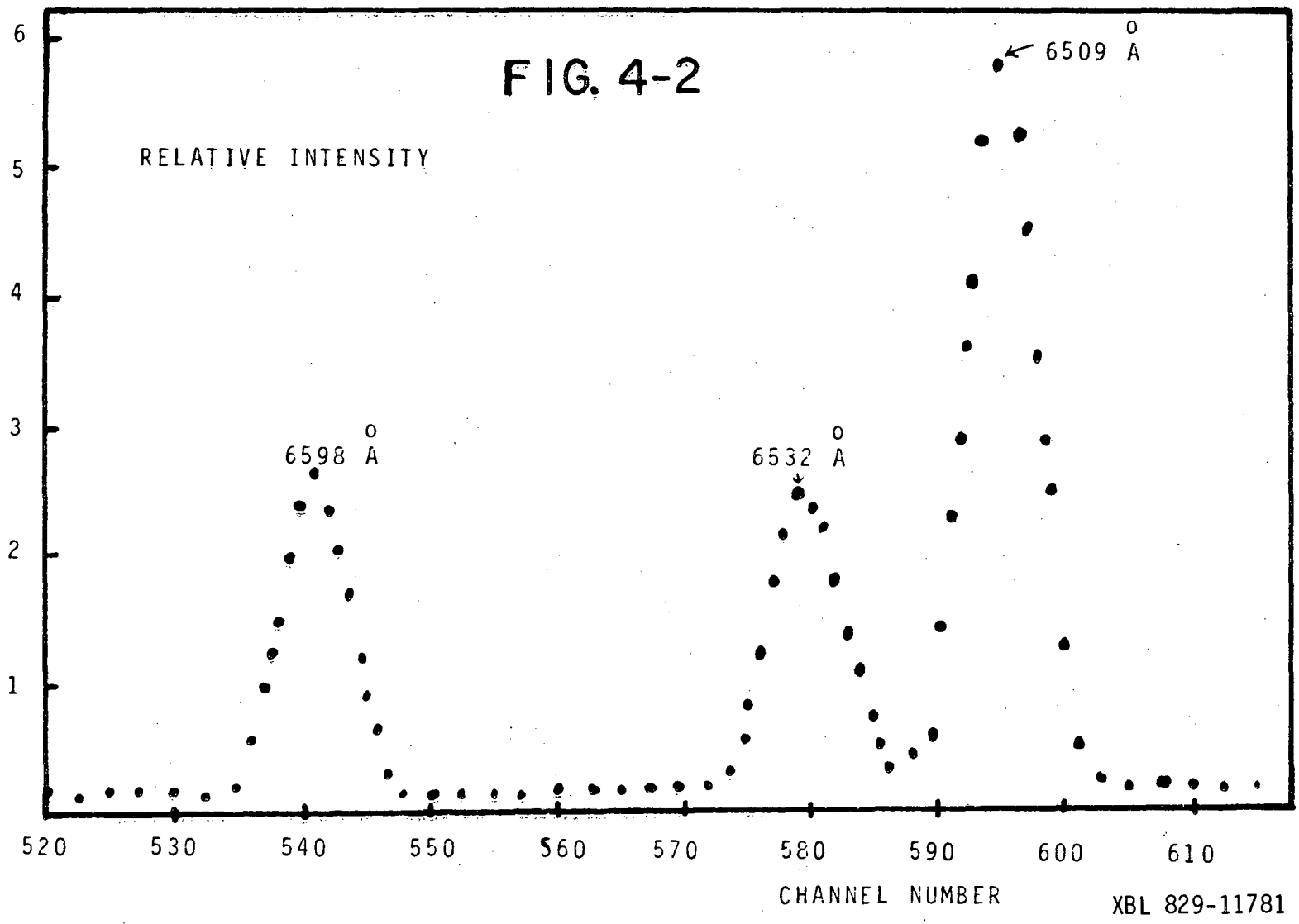
RELATIVE INTENSITY
6598 Å
6532 Å
6509 Å
1
2
3
4
5
6
520
530
540
550
560
570
580
590
600
610
CHANNEL NUMBER
XBL 829-11781

FIG. 4-2

standard error. The neutral filter was then changed to give maximum allowable count rate and this rate was determined with less than 1 % standard error. Again the lamp current was decreased to give a resonable count rate. By repeating these procedures the lamp emissivity versus the filament current was developed without the knowledge of transmission characteristics of neutral filters. This is shown in Fig. 4-3. At the smallest current, the lamp can be used without any filter. So far these procedures were performed at a fixed wavelength. The detection efficiency at other wavelengths was also required. Fig. 4-4 shows the wavelength response of the detection system to be constant within a few percents for the wavelengths of interset. Therefore, the detection efficiency could be set to be constant with a few percent standard error.

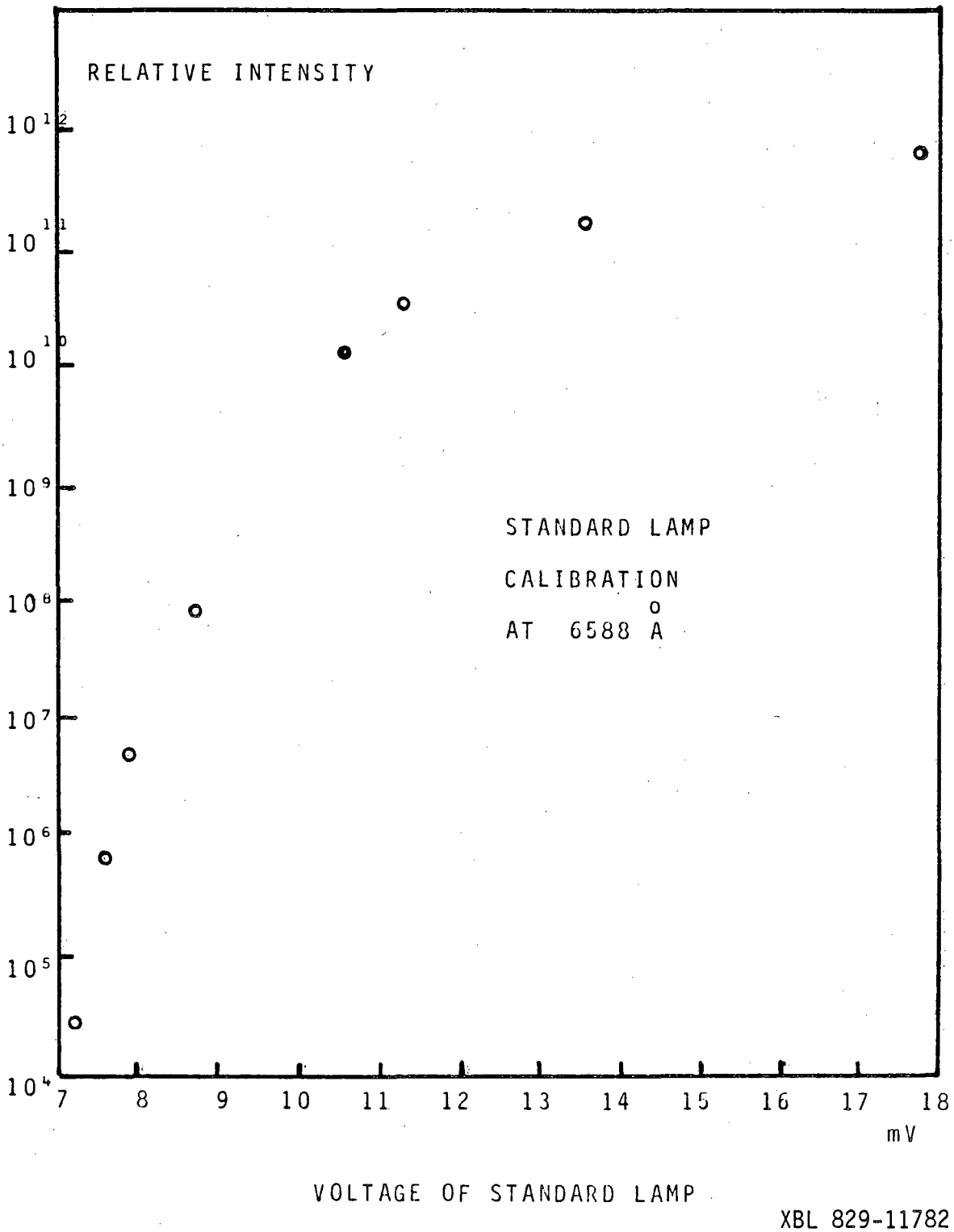

XBL 829-11782

FIG. 4-3

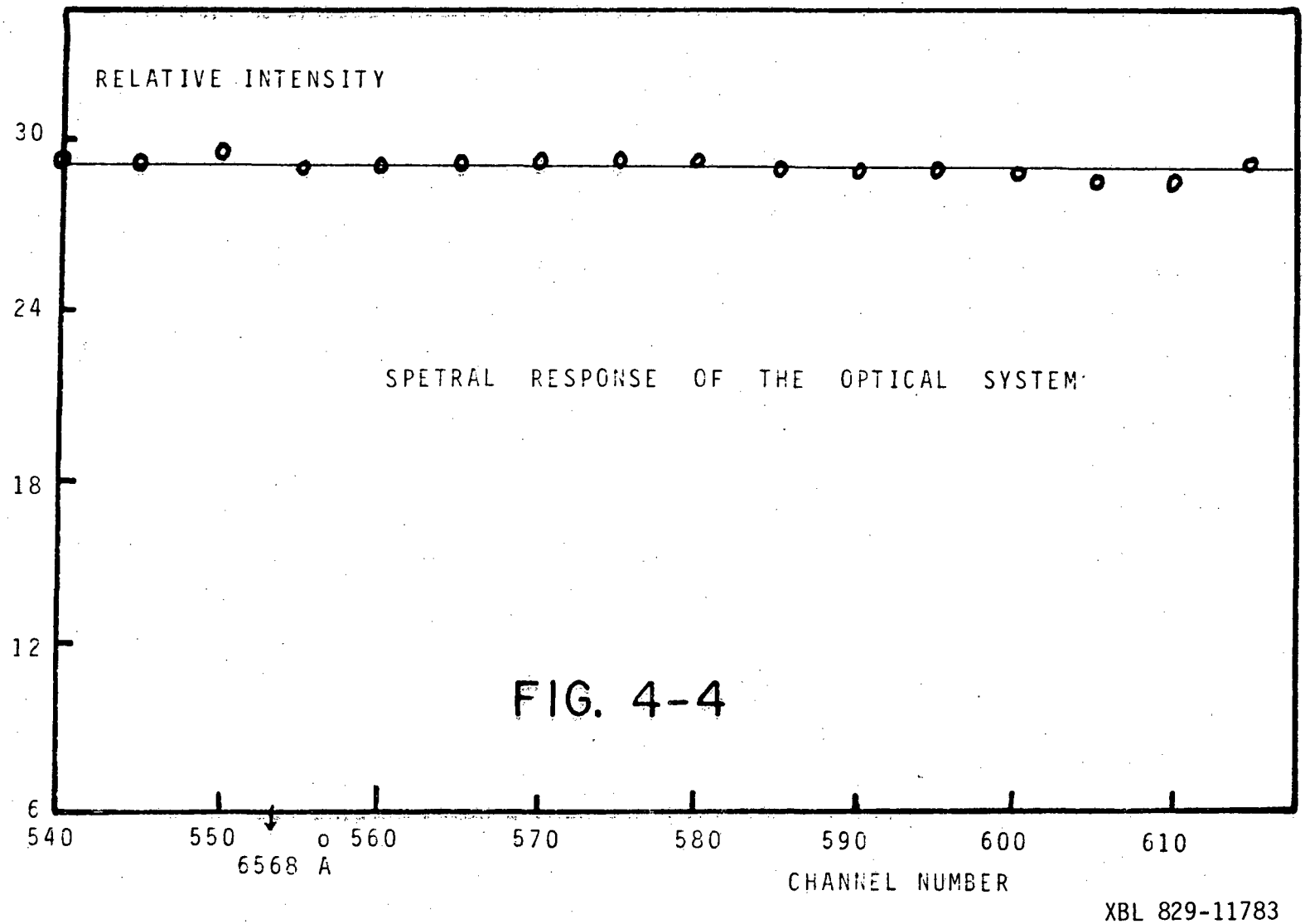
RELATIVE INTENSITY
30
24
18
12
6
SPETRAL RESPONSE OF THE OPTICAL SYSTEM
540
550
560
570
580
590
600
610
6568 A
CHANNEL NUMBER
XBL 829-11783

FIG. 4-4

B. Beam Tuning

After pumping down of the entire system the accelerator was turned on and the desired beam energy was set by the accelerator H.V. power supply. Then the palladium leak was tuned on to give the desired amount of hydrogen gas into the R.F. bottle which was checked by the ion gauge in the stack section of the accelerator. Initially the beam was tuned by letting it run straight down the accelerator and into a Faraday cup placed on the zero degree axis of the accelerator just after the momentum analyzing magnet. Without any collimation the current was typically 10^{-4}A with moderate ion soure extraction voltage and stack gas pressure. After a brief warm up time (normally about 20 minutes) all power suppliers and palladium leak were stable enough to give a few percent fluctuation in the beam intensity on a moderate time scale. Then the bending magnet was energized and set to the value needed to bend the desired energy and species beam into the beam line. After passing through one collimator (100 mil diameter) and one entrance aperture of the gas target cell, the beam hit the pyroelectric detector/Faraday cup in the gas target. The maximum beam current was obtained by adjusting steering plates, electrostatic quatrupole, the gas pressure inside the R.F. bottle, the extraction voltage and the focus voltage of the ion source. The amount of beam depended on the energy and species. The typical current on the

the final pyroelectric detector / Faraday cup inside the target cell was the order of ½ μA. The beam was stable during at least several minutes after tuning.

C. Development of Spectral Profile

After the beam was stabilized the beam was chopped by the use of a square wave potential applied to the steering plate. Then the calibration factor for the pyroelectric detector was measured as it was described in Chapter 3-D-b. Since the Doppler shifted line and the unshifted line had different spectral profiles, a well developed spectral profile was needed for separation of the Doppler shifted line from the unshifted line and the determination of a needed correction factor. The difference between those two spectral profiles resulted from an angular broadening effect.

The Doppler shift of the light which comes from the particle which moves with the velocity v can be described by

$$\lambda = \gamma \lambda_0 (1 - \beta \cos\theta) \qquad (4\text{-}6)$$

where λ_0 is the unshifted wave-length, $\beta = v/c$, c the velocity of the light and $\gamma = 1/\sqrt{1 - \beta^2}$. For a fixed $\beta << 1$ the angular broadening is given by

$$\Delta\lambda_A \simeq \lambda_0 \beta \sin\theta \Delta\theta \qquad (4\text{-}7)$$

For the Doppler unshifted light, there are only instrumental and thermal broadening effects. For the Doppler shifted line, there are angular broadening effects as well as instrumental broadening effect. As shown in the Appendix A the broadening of the monochromator was about 10 Å (full width at half maximum); and the thermal broadening is given below. According to the Franck-Condon principle when there is a collisional break up of the target molecule due to the energetic beam, the average kinetic energy of daughter particles is about 3 eV [46]. If the kinetic energies of the particles are in a Gaussian distribution the broadening of the light which comes from the target is given by [47]

$$\Delta\lambda_{th} = \frac{2\,\lambda_0}{c}\left(\frac{2\ln 2\, k_B T}{m}\right)^{\frac{1}{2}} \qquad (4\text{-}8)$$

where k_B is the Boltzmann constant, T is the temperature of the particles and m is the mass of the particle. For $k_B T \simeq 3$ eV, $\Delta\lambda_{th}$ is about 0.8 Å. Since the individual broadening effect behaves like an independent vector component the total broadening of the unshifted light is

$$\Delta\lambda_{Total} = \sqrt{\Delta\lambda_I^2 + \Delta\lambda_{th}^2} \simeq 10\ \text{Å} \qquad (4\text{-}9)$$

where the other broadening effects are negligible and this will be shown in Appendix A.

For the Doppler shifted light as discussed earlier, there is an observational angular broadening effect. Therefore, the total broadening effect is given by

$$\Delta\lambda_T = \sqrt{\Delta\lambda_I^2 + \Delta\lambda_{th}^2 + \Delta\lambda_A^2} \qquad (4\text{-}10)$$

Fig. 4-5 shows the typical spectral line profile.

Since intensity measurements were normally made by setting the monochromator at the peak of the line, corrections were necessary based on the shape of the line. For the unshifted line which remained at a constant setting of the monochromator, this correction could be included in the absolute calibration. The correction for the shifted line was the ratio of the counting rate at the peak of the line to integrated counting rate over the breadth of the line. It was typically 10 to 50 %.

D. Linearity Test

Linearity of signal with pressure provides a test of the system for all single collision effects. Both single and multiple collision effects are linear with respect to beam current. Frequently, during the course of an experiment, linearity tests were applied for assurance that the instrumentation was performing properly. Typical result of linear response with the current is shown in Fig. 4-6; that of linear response with the target pressure is shown is Fig. 4-7.

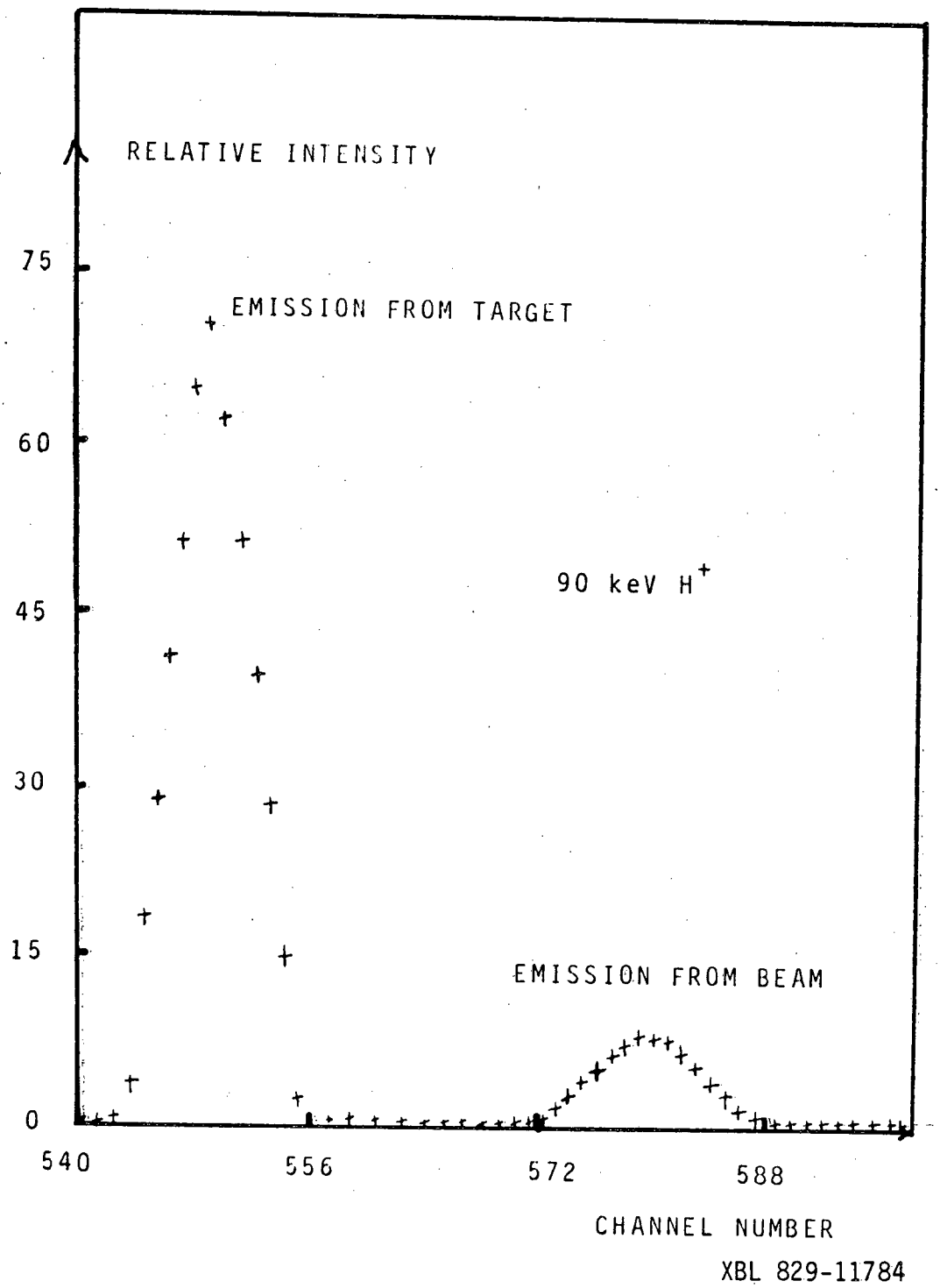
RELATIVE INTENSITY
75
60
45
30
15
0
EMISSION FROM TARGET
90 keV H+
EMISSION FROM BEAM
540
556
572
588
CHANNEL NUMBER
XBL 829-11784

FIG. 4-5

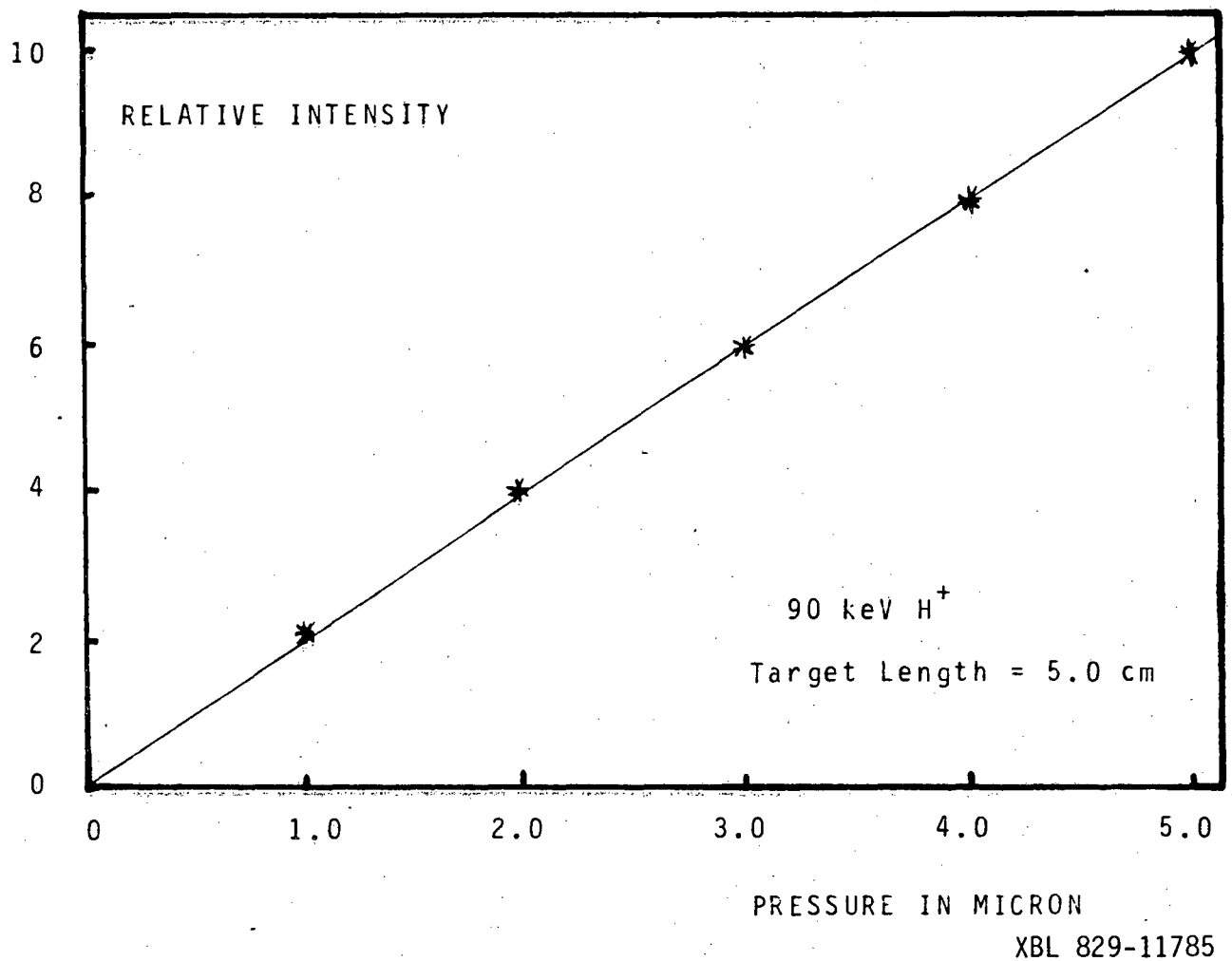
RELATIVE INTENSITY
90 keV H^+
Target Length = 5.0 cm
10
8
6
4
2
0
0
1.0
2.0
3.0
4.0
5.0
PRESSURE IN MICRON
XBL 829-11785

FIG. 4-6

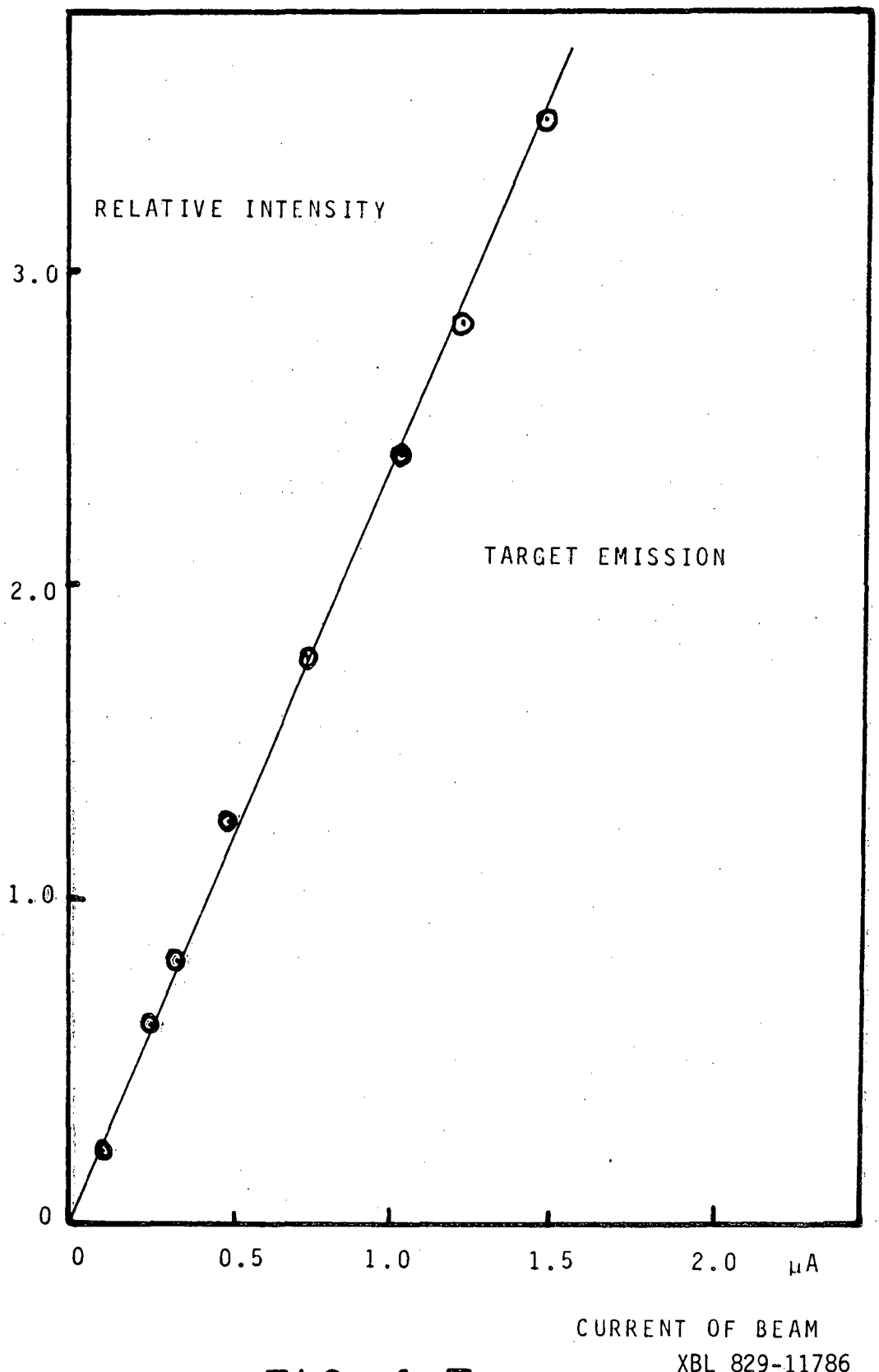
RELATIVE INTENSITY
TARGET EMISSION
3.0
2.0
1.0
0
0
0.5
1.0
1.5
2.0
μA
CURRENT OF BEAM
XBL 829-11786

FIG. 4-7

E. Data Analysis

All data were taken and analyzed using a HP 9845B (Hewlett Packard Co.) desk top computer. For the determination of the calibration factor K of the pyroelectric detector, a computer software program was used. Standard deviation was determined as errors for the K value and a typical integration time for a K measurement was 20 seconds. Soon after the determination of a K value, the spectral line shape was determined for separation of the Doppler shifted line from the unshifted line and measurement of a line broadening factor. The protram LINE was used for this purpose. This was composed of two parts. The first part was for the automatic data taking and storing of data. The second part was for the least square curve fitting of the spectral line shape. This curve fitting program had the basic structure for least square fitting of arbitrary combination of Gaussian curves. But for the unshifted line, the line shape was strictly triangular as shown in Chapter 4-C and the Gaussian curve fitting was invalid. Since one of the main broadening factors for the Doppler shifted line was an angular broadening which was asymmetrical, the Doppler shifted line was a slightly asymmetrical Gaussian curve. This curve fitting and other least square curve fitting used here after, were mainly based on the program, PISA[48], except some minor modifications. Since the line shape itself was indenpendent of the target

pressure, a high pressure target was used which decreased integration time to obtain sufficient signal to noise ratio (normally about 30 seconds) and less than 1 % standard counting error, was 20 seconds at the peak of the line shape. As mentioned earlier the beam was chopped to allow for measurement of the real signal plus the background signal and the background signal alone. The quantities measured were

T_{on}	;	time when the beam was on,
T_{off}	;	time when the beam was off,
C_{on}	;	total counting signal from the photomultiplier tube when the beam was on,
C_{off}	;	total counting signal from the photomultiplier tube when the beam was off
I_p	;	total signal from the pyroelectric detector when the beam was on,
K	;	the ratio of counting signal from Faraday cup to that of pyroelectric detector which gave the amount of current in 10^{-8} A units.

Then the signal/sec/10^{-8} A is given by

$$S = \frac{C_{on}/T_{on} - C_{off}/T_{off}}{I_p \; K/T_{on}} \qquad (4\text{-}11)$$

The curve fitting formula for the line was

$$y = a \; e^{-\left(\frac{x - b}{c}\right)^2} \tag{4-12}$$

In the thin target measurements, it was necessary to confirm that the measurements satisfied the single collision condition. To do that the curve for light intensity versus target density was developed. The signal formula was the same as before, and the curve fitting formula was

$$y = a + b\,x \tag{4-13}$$

where "a" was confirmed to be near zero.

After measuring the signal intensity versus the distance of penetration of the beam into the gas target, the sum of data were computer analyzed using the program PISA. Every data point was weighted by a weighting factor w_i which is biven by[49]

$$w_i = \frac{1/\sigma_i^2}{1/N \sum_i (1/\sigma_i^2)} \tag{4-14}$$

where N is number of data points and σ_i^2 is the estimated variance of each data point which was given by the quadrature of the sum of the related uncertainties. The uncertainties came from counting statistics, pressure and length measurements of the target. The error from the counting statistics can be expressed as

$$\sigma_{counting} = \sqrt{C_{on} + C_{off}\,(T_{on}/T_{off})^2} \,/\, C_{on}$$
$$\simeq \sqrt{C_{on} + C_{off}} \,/\, C_{on} \qquad (4\text{-}15)$$

The uncertainty of the pressure measurement was mainly from the zero point drift of the capacitance manometer and given approximately as 0.1 micron per 200 second measurement time at most. The uncertainty from the measurement of the distance through which the beam went was 0.1 cm at most. These effects were considered when the collection of data were analyzed.

A curve fitting formula for separation of the 3s, 3p and 3d state cross sections was

$$y = \sum_i a_i \left(1 - e^{-x/v\tau_i} \right) \qquad (4\text{-}16)$$

where v is the beam velocity and τ_i is the effective life time of each excited state. Fig. 4-8 shows the typical result of this curve fitting. For the thick target measurement of the target dissociative excitation in the case of H^+ impact on H_2 the curve fitting formula was given by

$$y = a + b\, e^{-\sigma_T x} \qquad (4\text{-}17)$$

where $\sigma_T = \sigma_{10} + \sigma_{01}$, and σ_{10} and σ_{01} are charge exchange cross section for H^+ and H^0 as defined earlier.

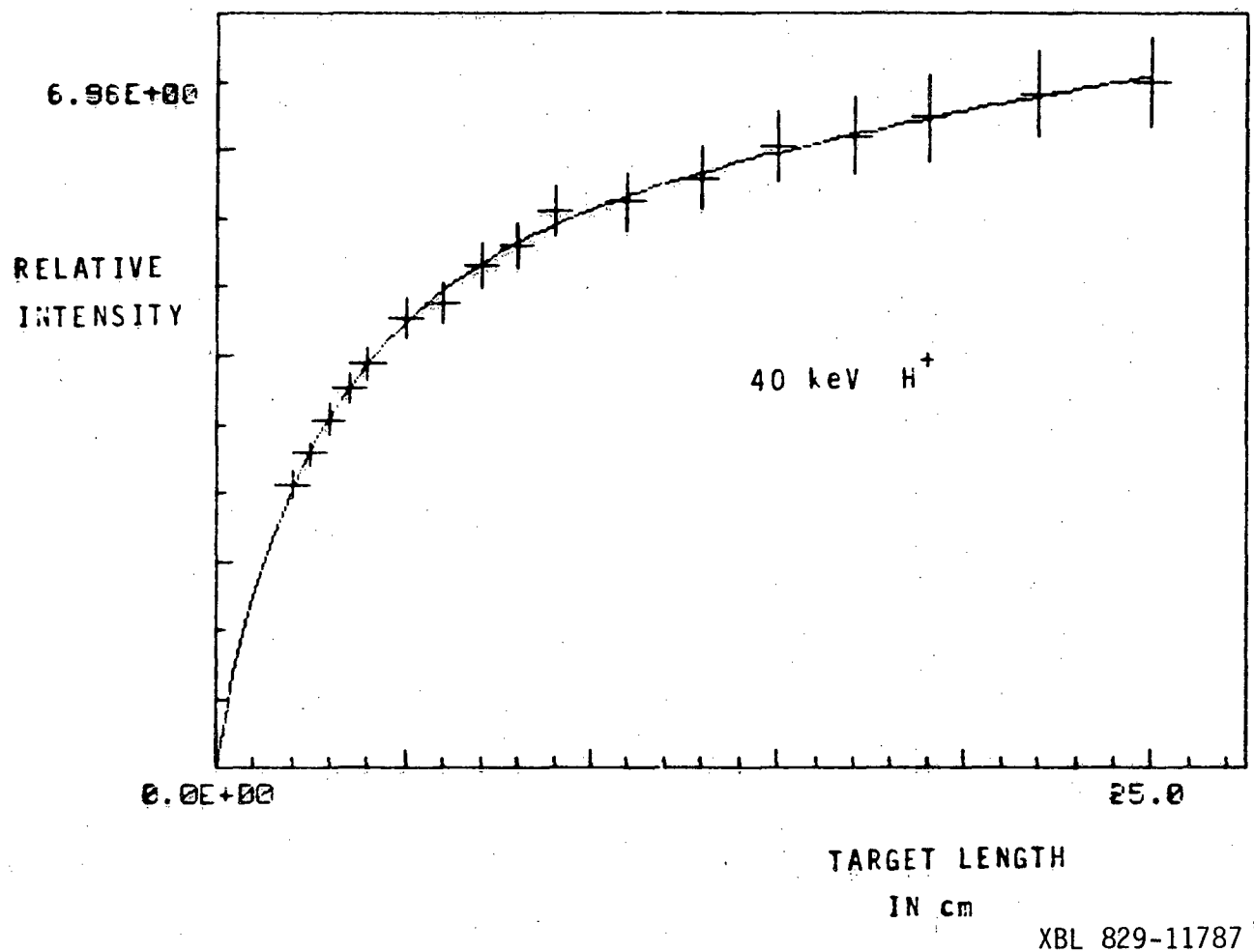

XBL 829-11787

FIG. 4-8

The typical result of this curve fitting is shown in Fig. 4-9.

So far no polarization correction has been discussed. If the observation apparatus is set to observe emission from the target at an angle θ to the beam direction as shown in Fig. 4-10, then the correction factor for the anisotropy in emission is given by[50]

$$\gamma = \frac{(3 - P)}{3(1 - \cos^2\theta)} \frac{(C + 1)(\alpha + 1)}{2(C\alpha + 1)} \qquad (4\text{-}18)$$

where P is the polarization of the emission and C is the ratio of the emission intensity polarized parallel to the beam direction to that polarized perpendicular to the beam direction. And α is the ratio of the instrumental sensitivity parallel to the beam direction to that polarized perpendicular to the beam direction. For $\theta = 54.76^{\circ}$ the first factor in the above equation is 1. Since in this experiment $1/\alpha = 0$, therefore γ is simply given by

$$\gamma = \frac{1 + 1/C}{2} = \frac{1 + I_{\perp} / I_{\parallel}}{2} \qquad (4\text{-}19)$$

where $I_{\perp}$ and $I_{\parallel}$ were defined earlier in Chapter 2.

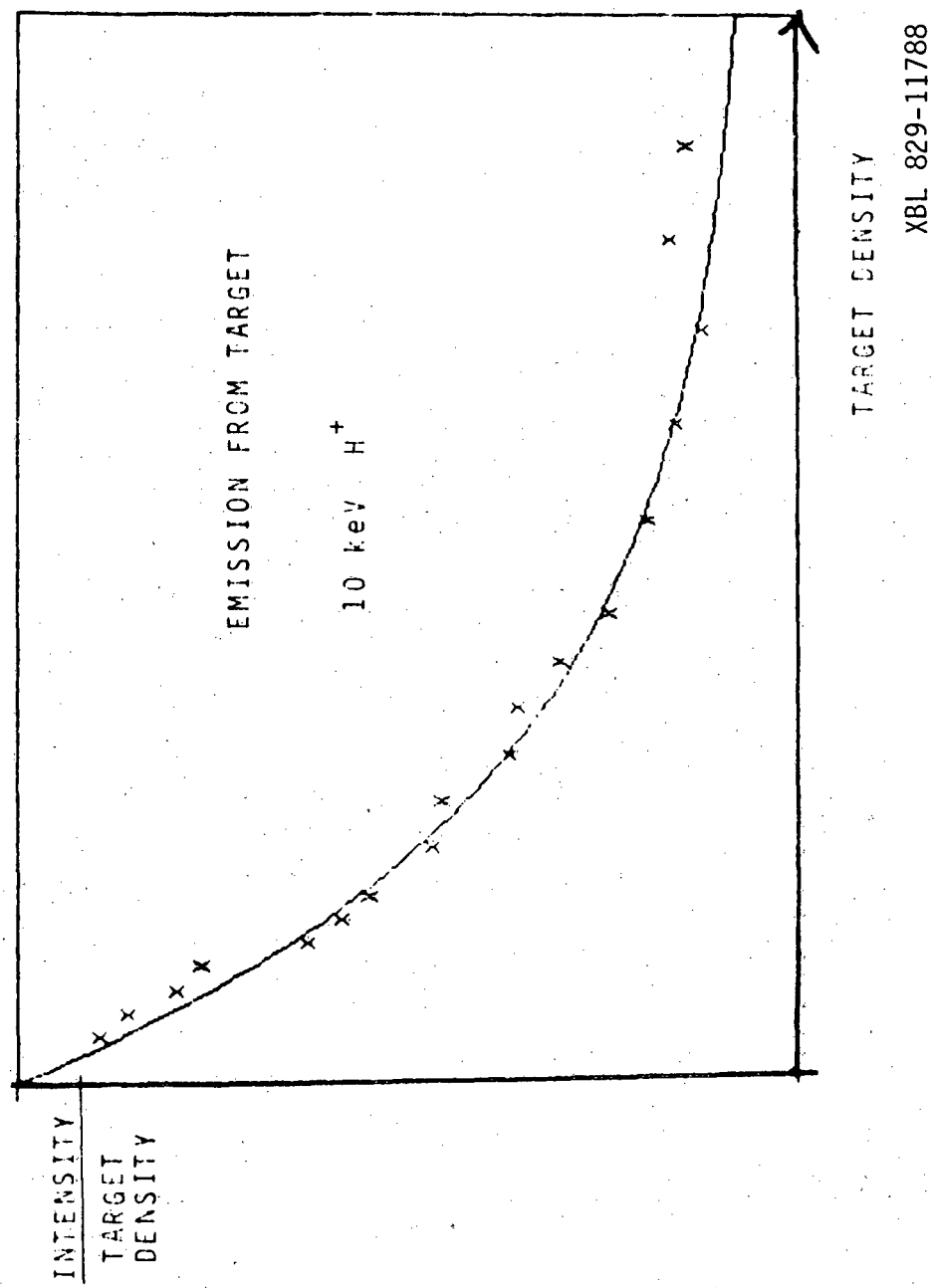
EMISSION FROM TARGET
10 keV H^+
INTENSITY / TARGET DENSITY
TARGET DENSITY
XBL 829-11788

FIG. 4-9

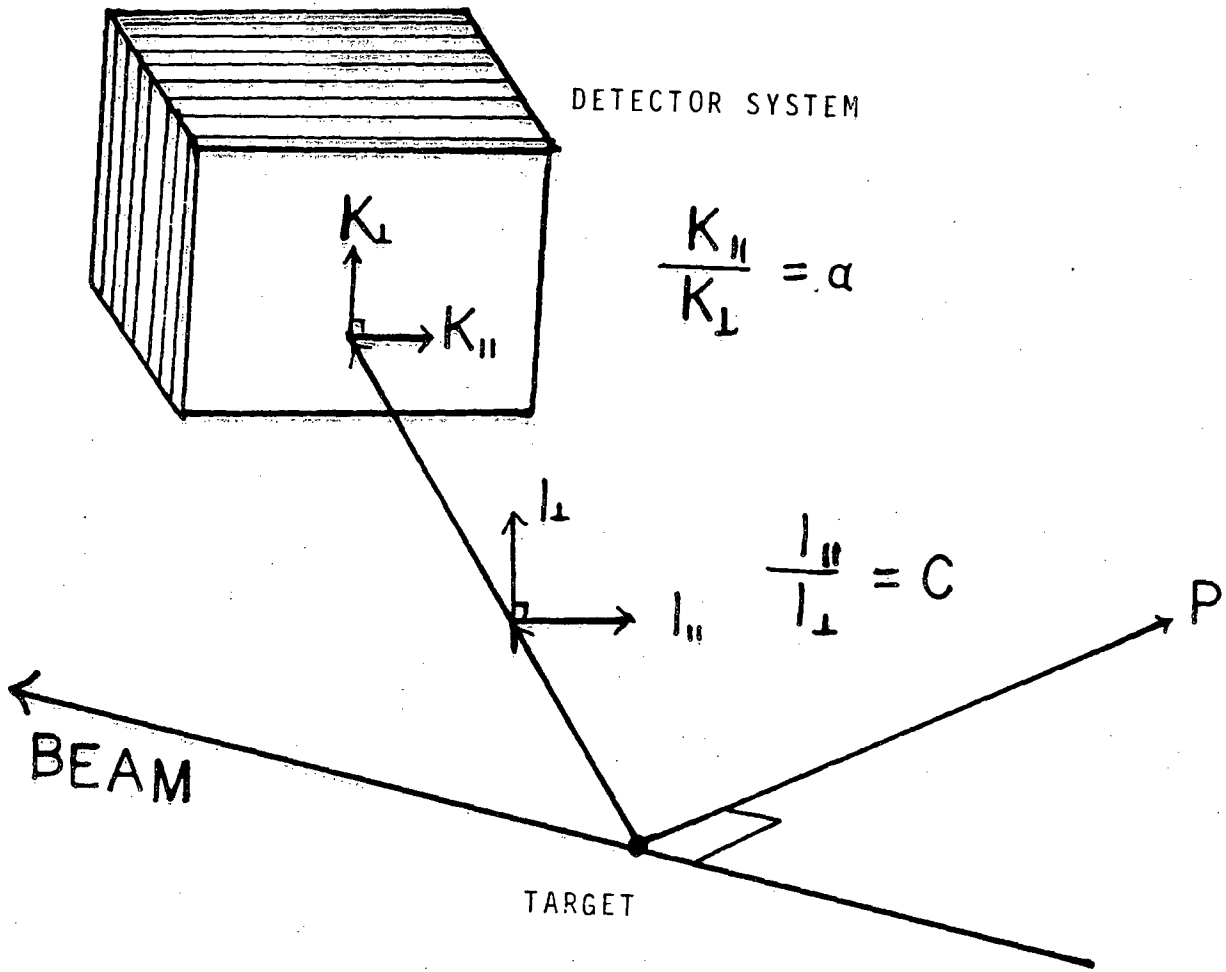

FIG. 4-10

XBL 829-11789

CHAPTER 5

Results and Discussion

A. Results

The final results and error estimations are presented in Table 5-1 --- 5-5 and Fig. 5-1 --- 5-17. The detailed methods of data analysis have been given in Chapter 4, and the error analysis is given in this section. In general there are two classes of errors. The one is the class of systematic errors such as those which result from limited accuracy of calibrated equipment, from the impurity of prepared materials and from pre-estimated values used in the experiment. The other is the class of the random errors, such as those result from the statistical fluctuations of counting finite numbers of events and from small unpredictable drifts in the instrumental sensitivities and zeros.

The important quantities from which resulted systematic errors were the beam and target impurity, the uncertainties in measurement of the target density, the beam current and the beam energy, the uncertainty in calibration of the photon detector and the uncertainty in pre-estimated values of the life times of the excited quantum states. The beam purity was confirmed by a magnetic mass analyzer with less than 1% error. The purity of the target gas was limited by the impurity of the target gas itself and by residual back-

ground gas in the target chamber. The purity of the target gas had been assured by the manufacturer and the impurity level should not exceed 1%. Since the minimum target pressure used in this experiment was about 0.2 mTorr where residual background pressure was maintained less than 2 μTorr the error from this should not exceed 1% because the cross sections for H_2 gas is almost the same as that of the impurity gas. The uncertainty in the measurement of the beam current was due to two factors. The one was the uncertainty in normalization of the pyroelectric signal to the Faraday cup signal. The other was the limitation of the accuracy in the measurement of the Faraday cup current. The former uncertainty was kept to be about 1%. The accuracy of the Faraday cup current was established by checking the calibration of the digital current integrator. The test was carried out with a standard current source and gave less than 1% error. The calibration of the capacitance manometer was checked by comparing it to an oil-manometer. The oil-manometer and the capacitance manometer agreed to within 5% which allowed up to 7% maximum uncertainty in the pressure measurement. The accuracy of the beam energy was confirmed by the terminal voltage of the accelerator which was calibrated with a known standard meter, and was found to be accurate to within 5%.

The calibration of the detection sensitivity of the photon detection system including optics employed a tungsten strip filament lamp as a standard source of light emission.

The emissivity of the standard lamp at a specified filament current (35 A) was given by the manufacturer; and had an accuracy with a 5% maximum error. In the calibration procedure the other working tungsten strip lamp was used. Therefore the normalization of this working lamp to the standard lamp resulted in 10% maximum uncertainty. The development of the lamp emissivity versus the filament current characteristics which was used in the calibration procedure resulted in 3% maximum error. In the measurement of the resolution $\Delta\lambda$ and the slit length there are 5% and 2% uncertainties. The uncertainty in the wavelength response of the detector system was maximum 3%. The effect of the uncertain velocities and lifetimes had been studied by J.C. Ford et al.[13], and typically a 1% change in those produced changes in the 3s, 3p and 3d corss sections of, respectively, 0.5, 0.5 and 1.5 %.

For the purpose of final data interpretation there is another way of classification of errors. Conventionally the cross sections are described as functions of the energy, therefore, the cross seciton curves have the uncertianty in the structure of the curves themselves and in the absolute magnitudes of the whole curves. The class of errors thich varies the internal structure of the cross section curve is defined as a relative uncertainty. And the class of errors which varies the absolute magnitudes of the whole curves is defined as an absloute uncertainty. The absloute uncertainty

presented here, was determined by the possible errors in beam energy, pressure, current and detection sensitivity measurement, etc.. The total absolute uncertainty was given by taking the root of the sum of the squares of these errors and found to be 17% at the most.

The main sources of the random errors were limited counting statistics and zero point drift of the capacitance manometer during the measurement procedure. The random errors resulted by counting statistics was kept to be the order of 1%. Even the total random error during this experiment was kept small, there might still be large random error in the derived cross sections for the 3p and 3d state excitations of the projectile. This was due to either relatively small magnitudes of those or/and branching ratio. This effect was counted during the establishment of the relative uncertainties of the cross sections.

$H^+ + H_2$ Collision, Excitation Cross Sections in $10^{-18} cm^2$

Energy in keV	Slow n=3	Fast 3s	Fast 3p	Fast 3d
20	5.01±0.11	4.29±0.26	10.7±1.1	1.06±0.13
30	3.70±0.15	6.60±0.41	7.9±1.7	0.81±0.20
40	2.68±0.05	5.47±0.33	7.0±1.4	0.33±0.16
50	2.42±0.04	4.77±0.29	4.0±1.2	0.34±0.14
65	1.81±0.03	3.00±0.18	1.12±0.75	0.29±0.09
80	1.65±0.03	2.23±0.14	--------	---------
100	1.33±0.02	1.13±0.07	0.39±0.28	0.133±0.034
125	1.18±0.02	0.693±0.042	0.31±0.17	0.0266±0.0070
150	1.04±0.01	0.239±0.015	----------	----------

Table 5-1

$\underline{H}^+ + H_2$ Collision

Energy	Polarization in %		Cross Sections in $10^{-18}cm^2$	
(keV)	3p	3d	3p, m=0	3p, m=±1
20	25±10	-8±12	5.4±1.0	2.7±0.7
30	9±21	-2±24	3.1±1.3	2.4±1.1
40	7±20	-1±50	2.7±1.1	2.2±1.0

Table 5-2

$H_2^+ + H_2$ Collision, Excitation Cross Sections in $10^{-18} cm^2$

Energy in keV	Slow n=3	Fast 3s	Fast 3p	Fast 3d
20	3.81±0.08	4.64±0.47	5.9±1.4	3.75±0.30
30	4.95±0.18	4.94±4.94	7.6±1.6	3.86±0.31
40	5.12±0.20	4.81±0.44	8.1±1.7	4.01±0.32
50	4.98±0.18	5.51±0.55	7.9±1.8	4.20±0.34
65	4.87±0.15	5.59±0.56	10.8±2.2	3.80±0.31
80	4.12±0.23	5.51±0.55	11.2±1.9	3.26±0.26
100	3.52±0.08	4.24±0.60	7.4±1.4	3.52±0.28
125	3.01±0.07	3.71±0.34	6.3±1.2	3.29±0.26
150	2.23±0.10	2.72±0.25	6.4±1.1	2.71±0.22

Table 5-3

$H_3^+ + H_2$ Collision, Excitation Cross Sections in $10^{-18} cm^2$

Energy in keV	Solw n=3	Fast 3s	Fast 3p	Fast 3d
20	2.50±0.05	3.73±0.26	2.30±1.06	3.22±0.26
30	3.61±0.12	5.03±0.35	3.95±1.31	3.31±0.27
40	4.37±0.11	6.18±0.43	9.10±2.28	4.32±0.35
50	4.96±0.15	6.66±0.47	7.14±1.72	4.48±0.36
65	4.95±0.10	8.00±0.56	7.69±2.08	4.05±0.33
80	5.02±0.12	7.20±0.51	14.6±3.6	3.24±0.26
100	5.38±0.14	7.47±0.53	11.2±2.8	3.56±0.29
125	5.03±0.08	7.58±0.53	9.5±2.4	3.79±0.31
150	3.84±0.10	6.97±0.49	12.3±3.1	2.12±0.17

Table 5-4

$H^0 + H_2$ Collision

Production of Slow n=3 state H-atoms

Energy (keV)	Cross Sections ($10^{-18} cm^2$)
15	2.16±0.31
25	1.69±0.24
35	1.21±0.17
50	0.91±0.14
75	0.69±0.13

Table 5-5

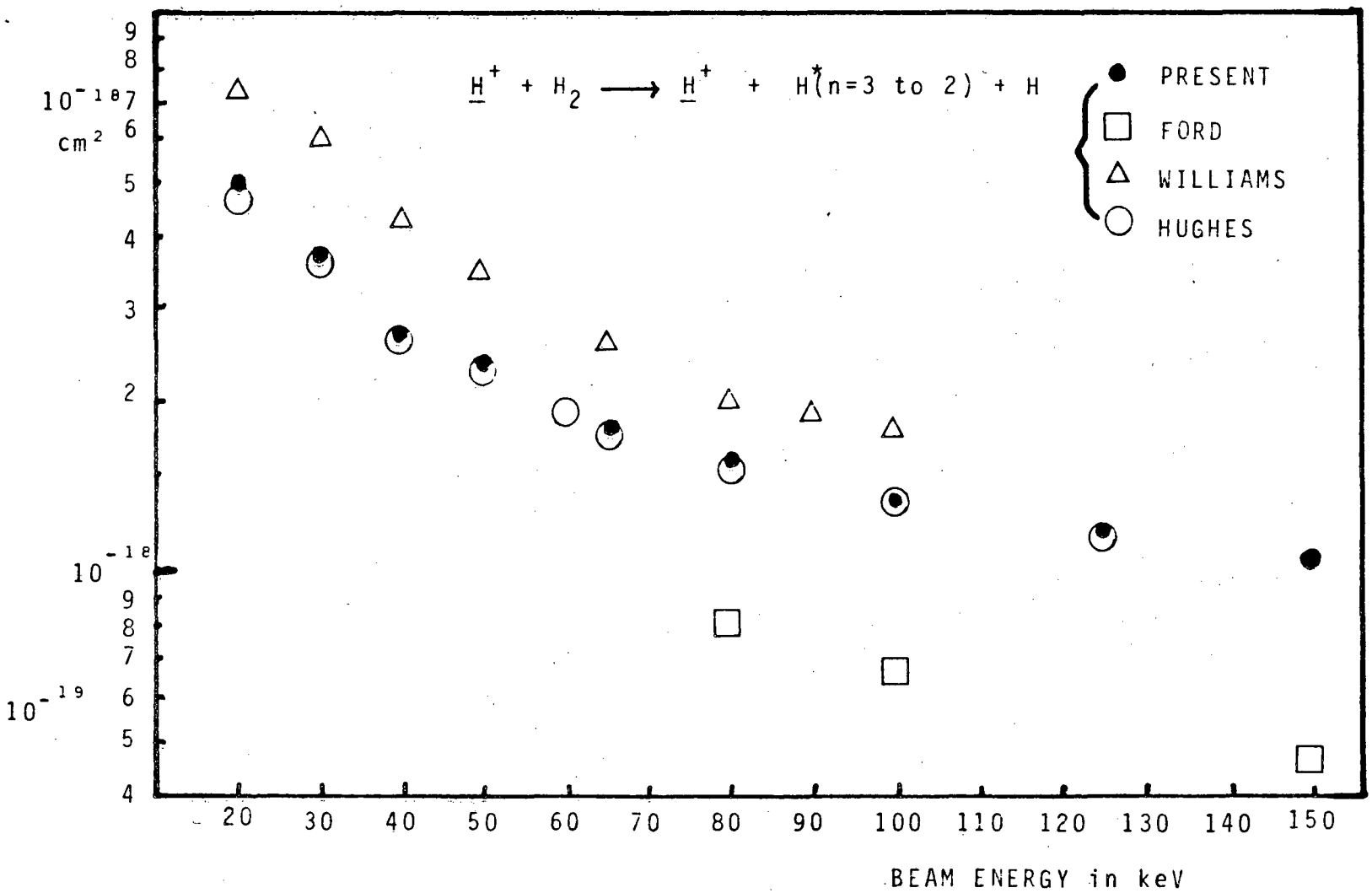

XBL 829-11790

FIG. 5-1

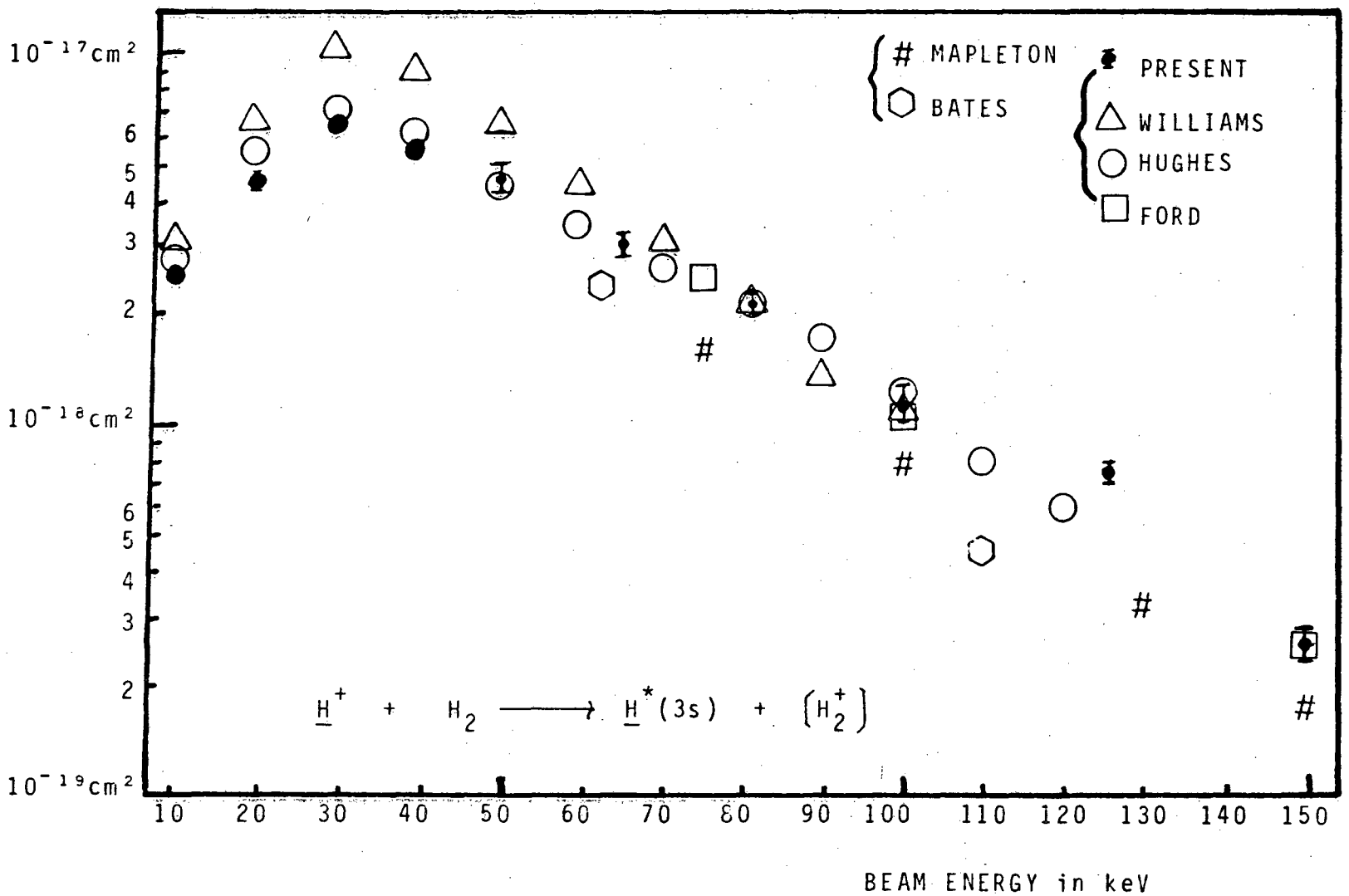

XBL 829-11791

Fig. 5-2

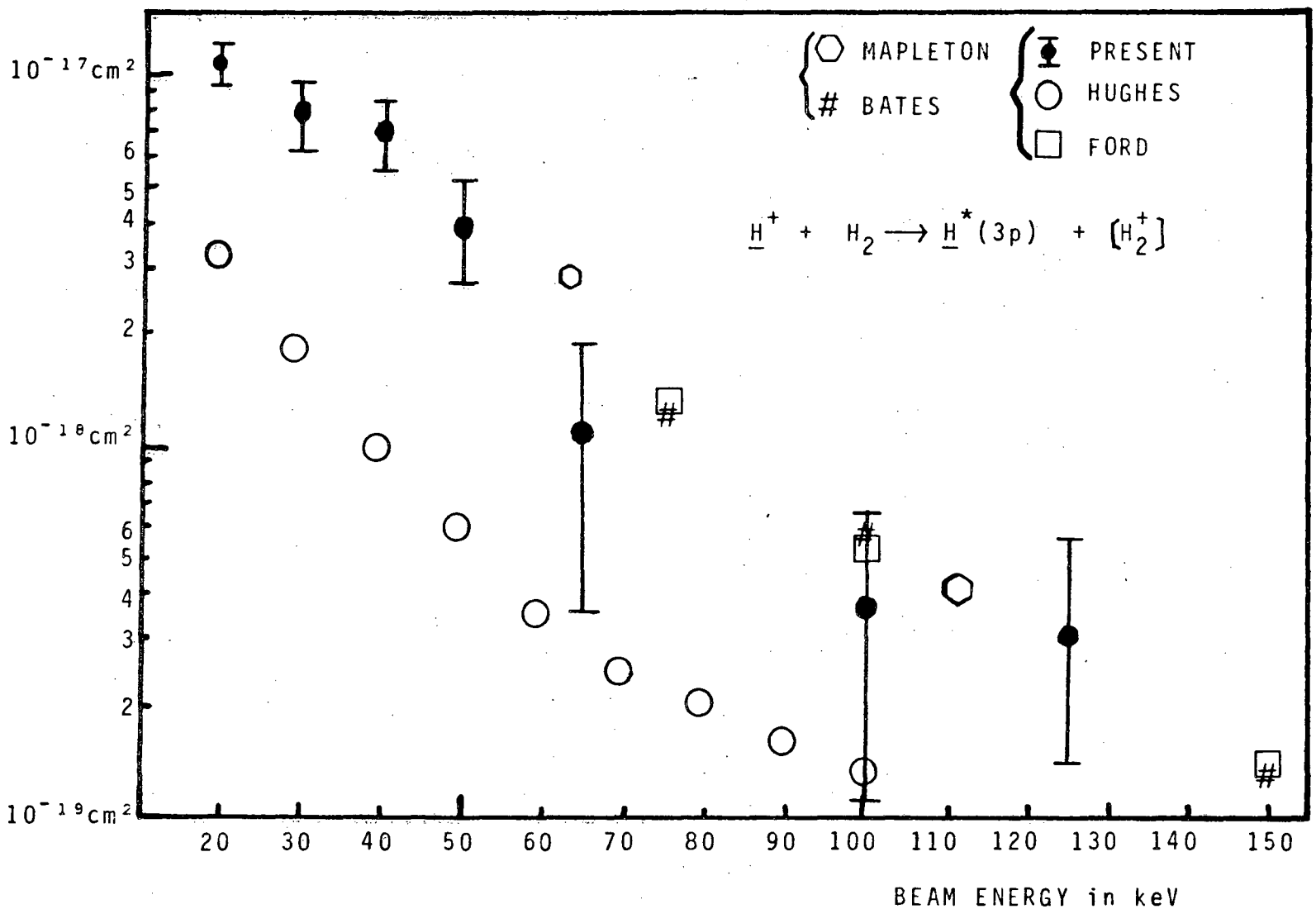

XBL 829-11792

Fig. 5-3

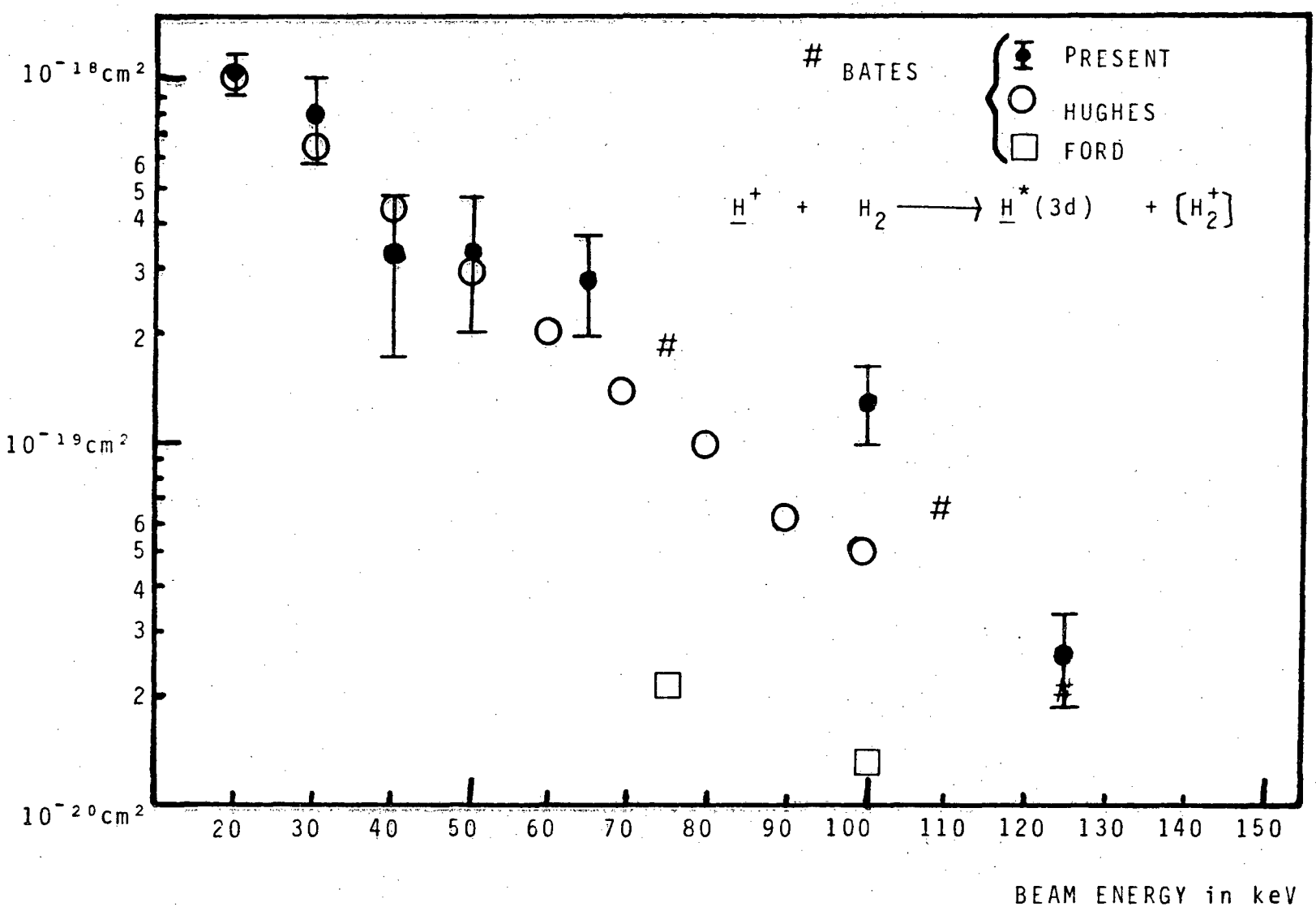

Fig. 5-4

XBL 829-11793

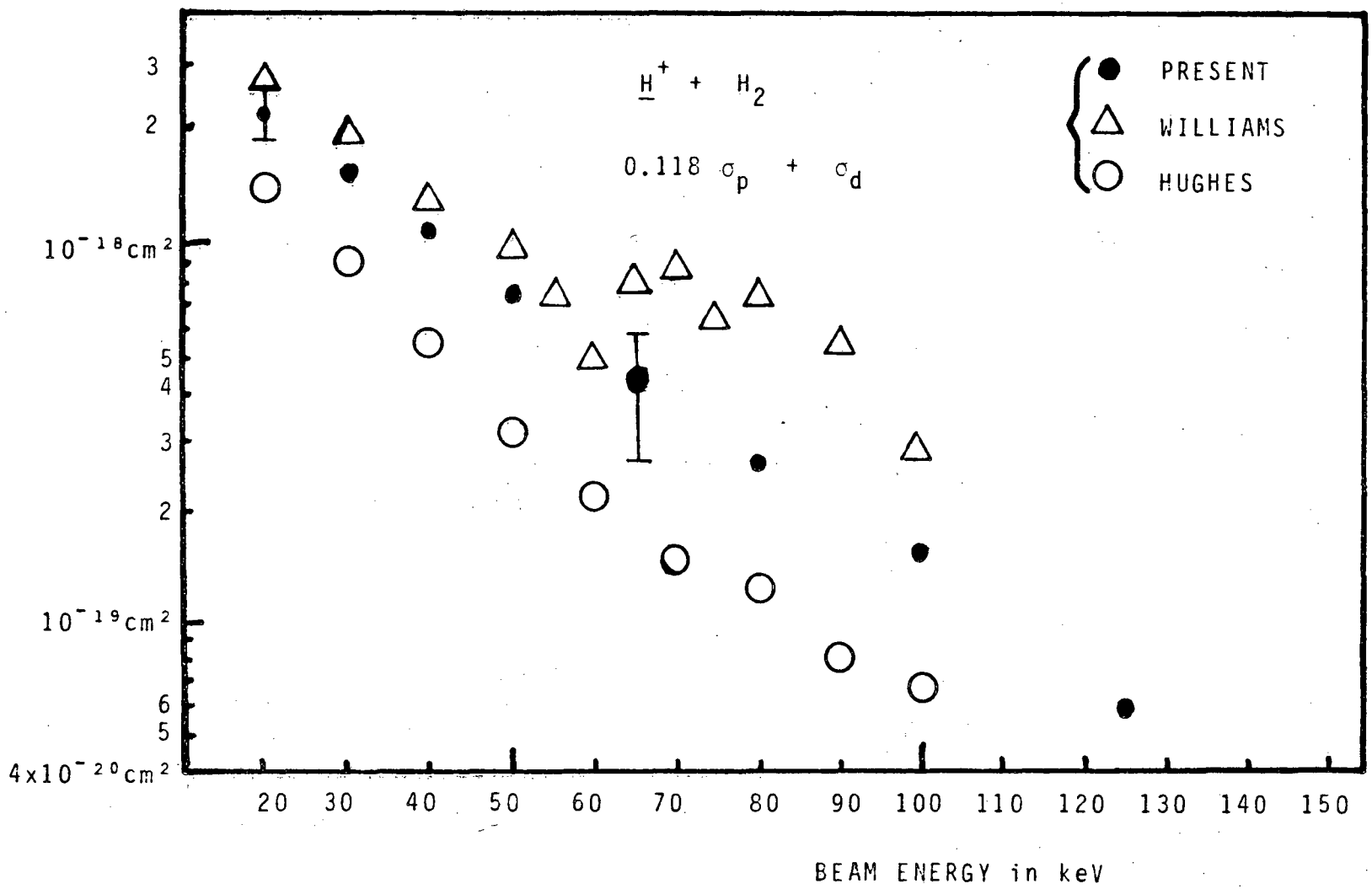

XBL 829-11794

Fig. 5-5

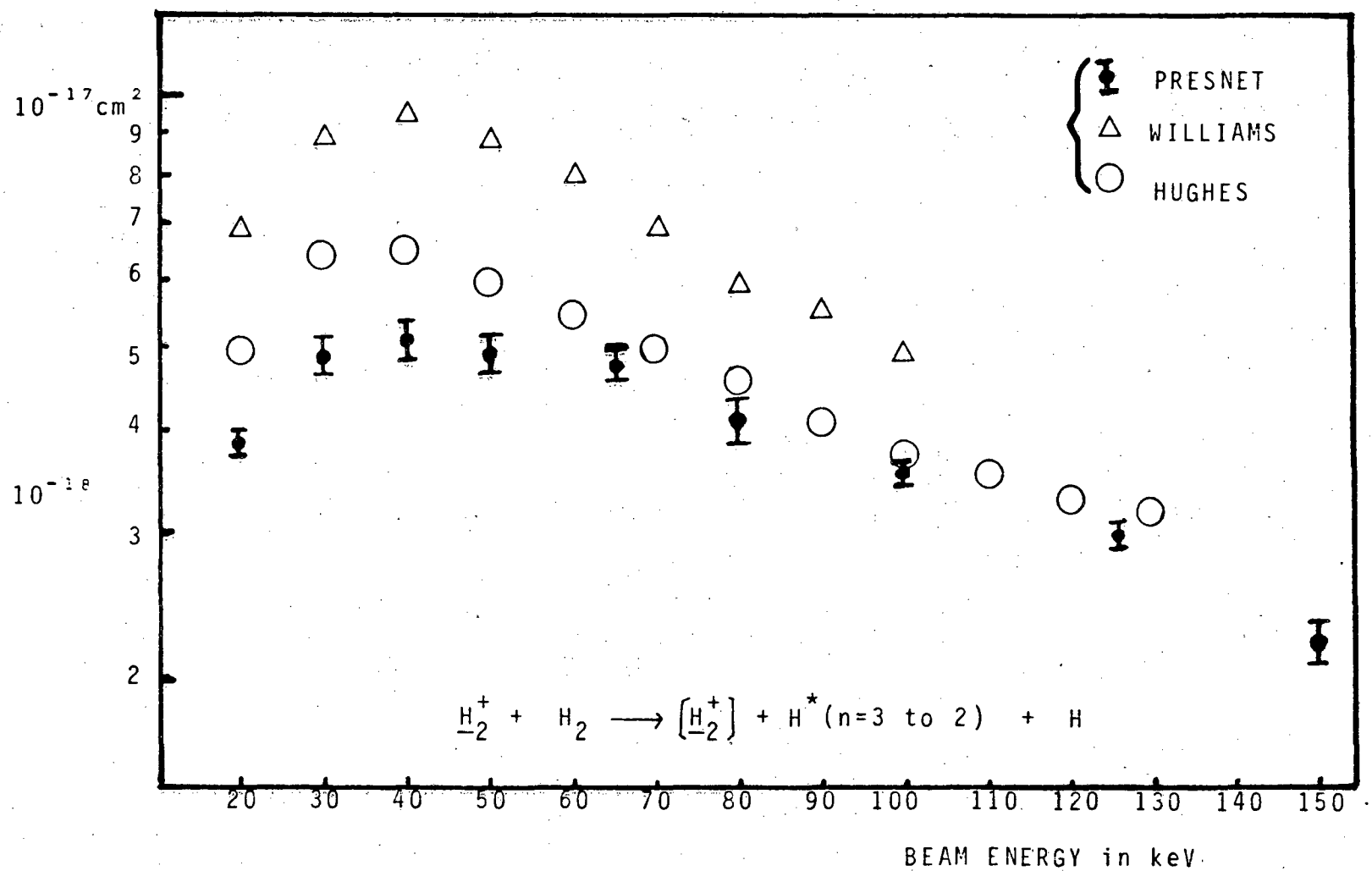

XBL 829-11795

Fig. 5-6

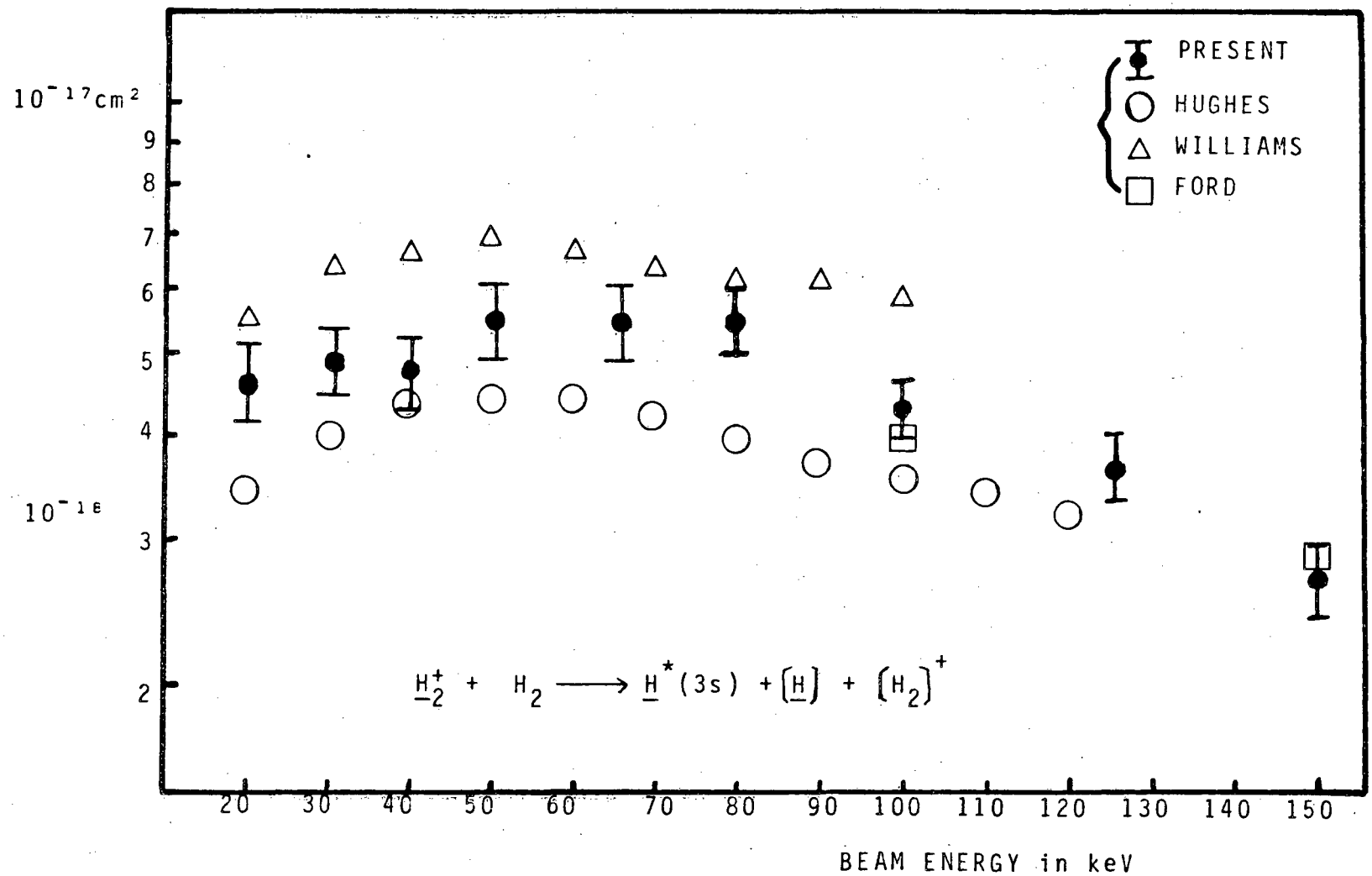

XBL 829-11796

Fig. 5-7

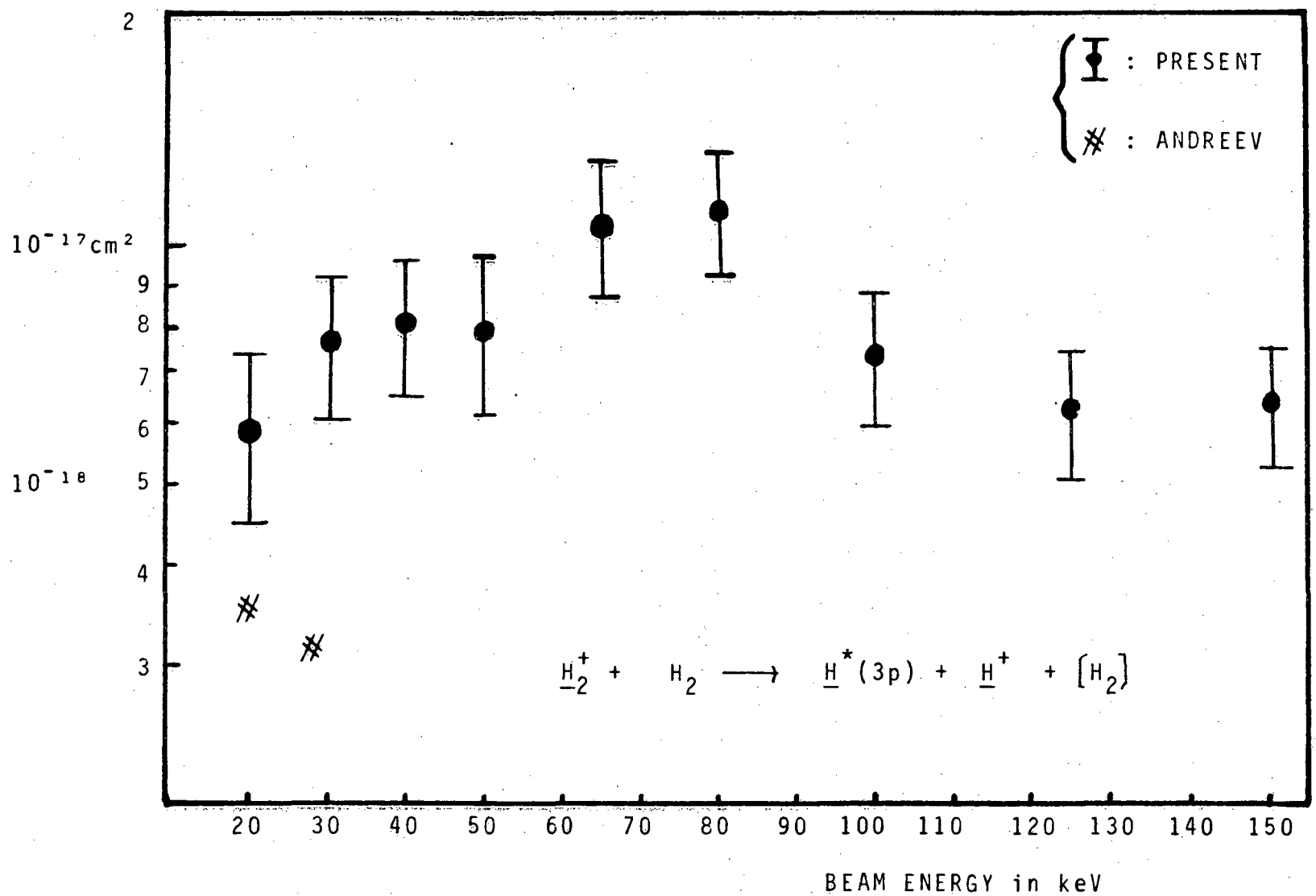

XBL 829-11797

Fig. 5-8

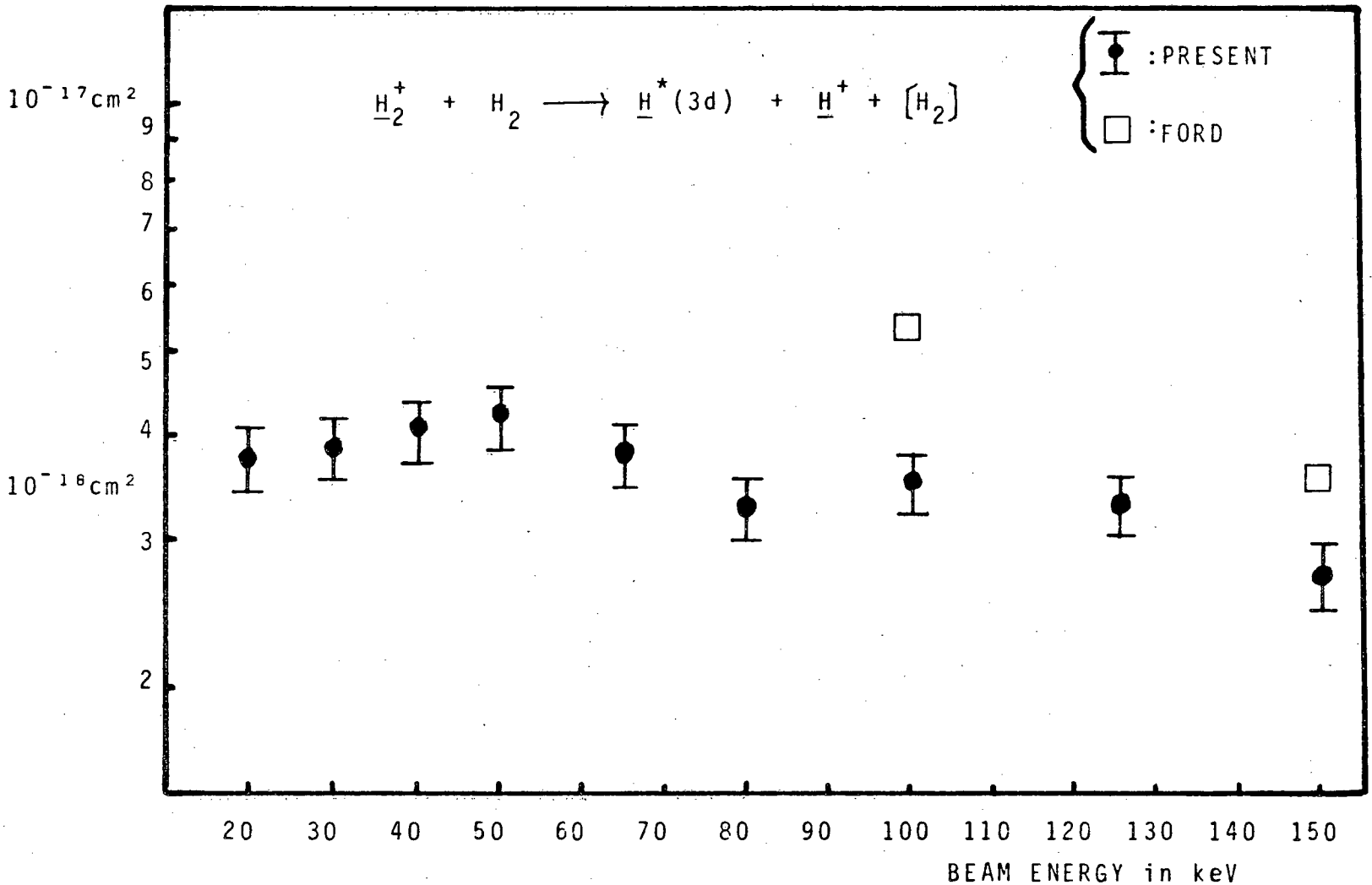

XBL 829-11798

Fig. 5-9

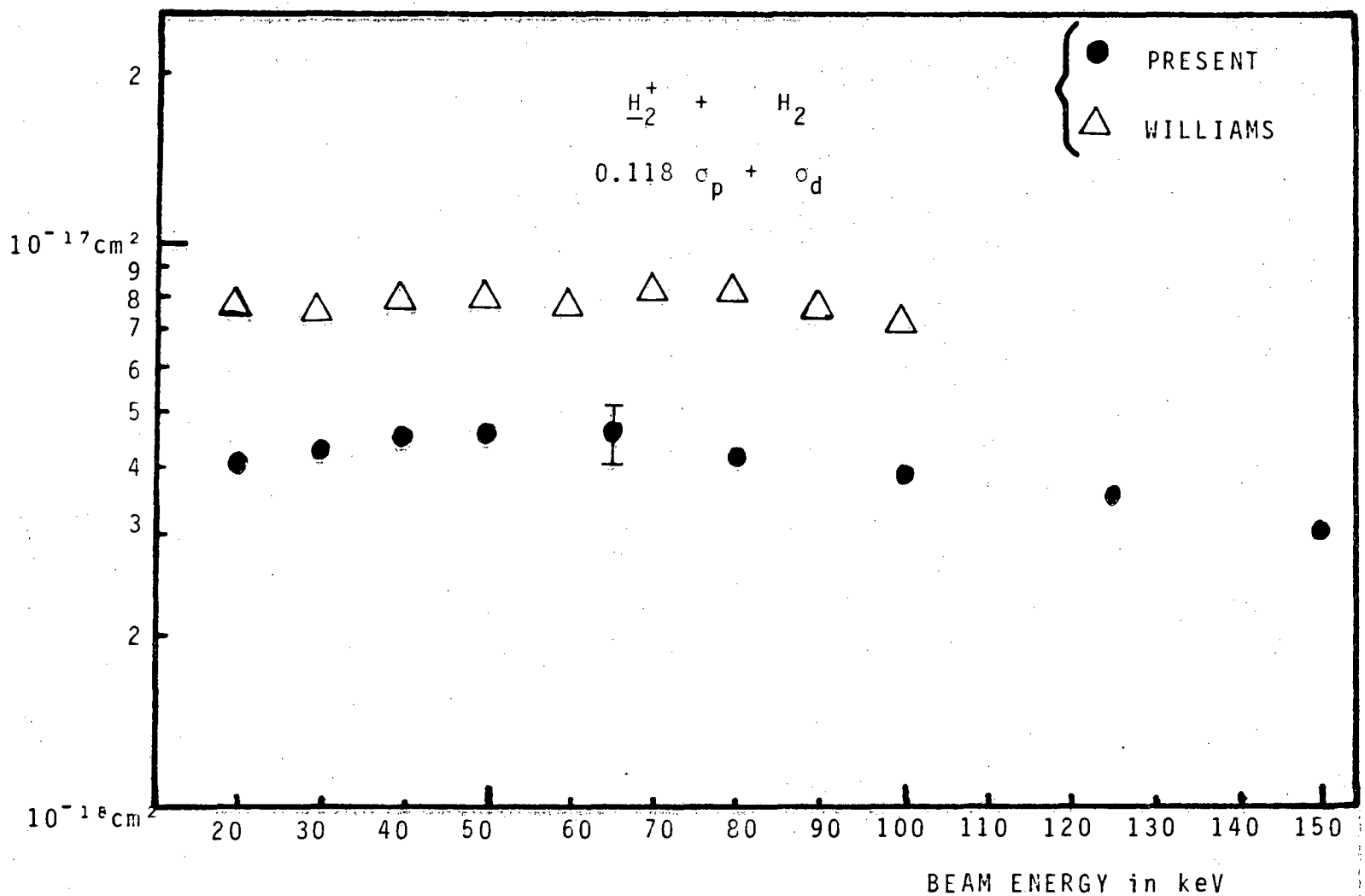

XBL 829-11799

Fig. 5-10

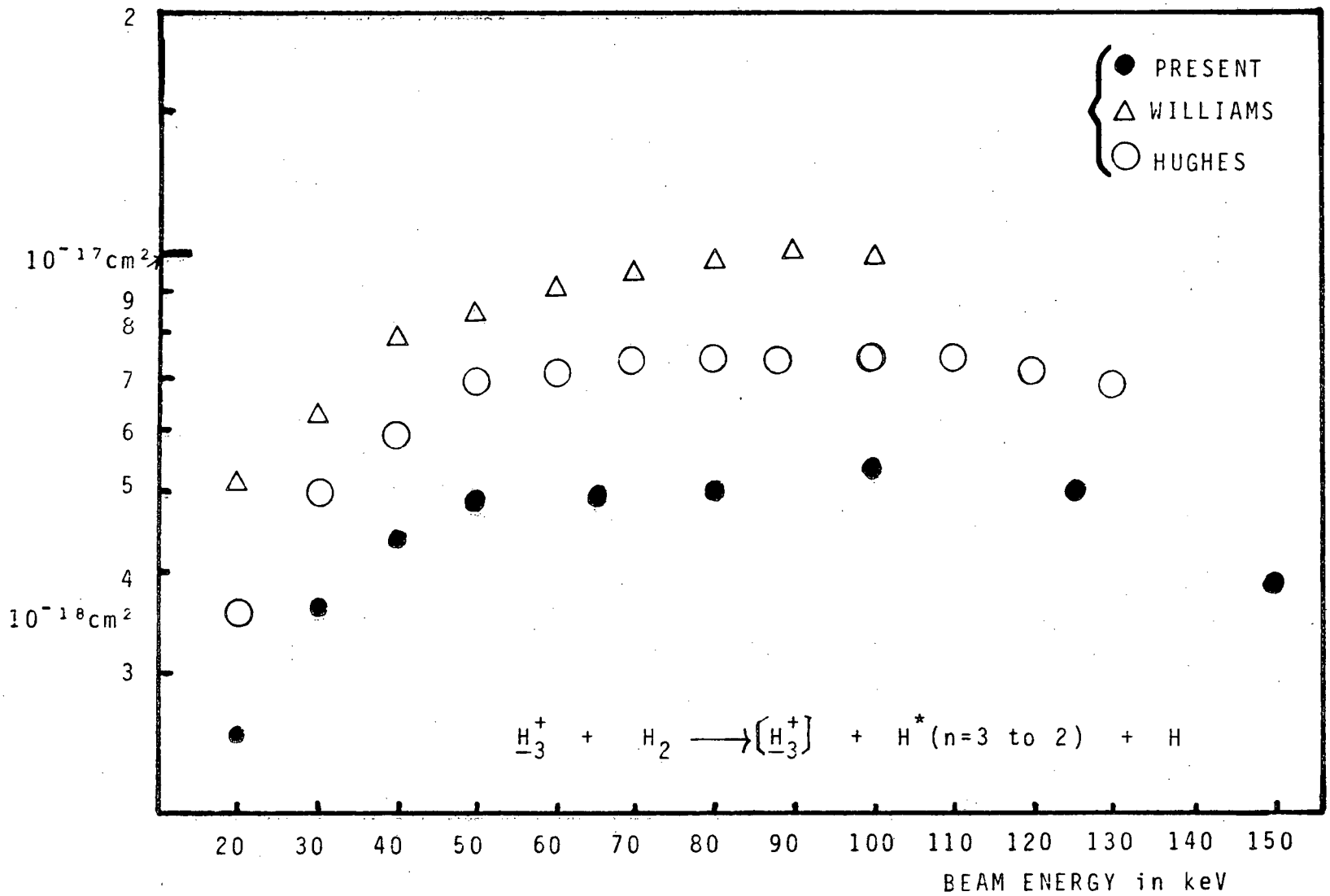

Fig. 5-11

XBL 829-11800

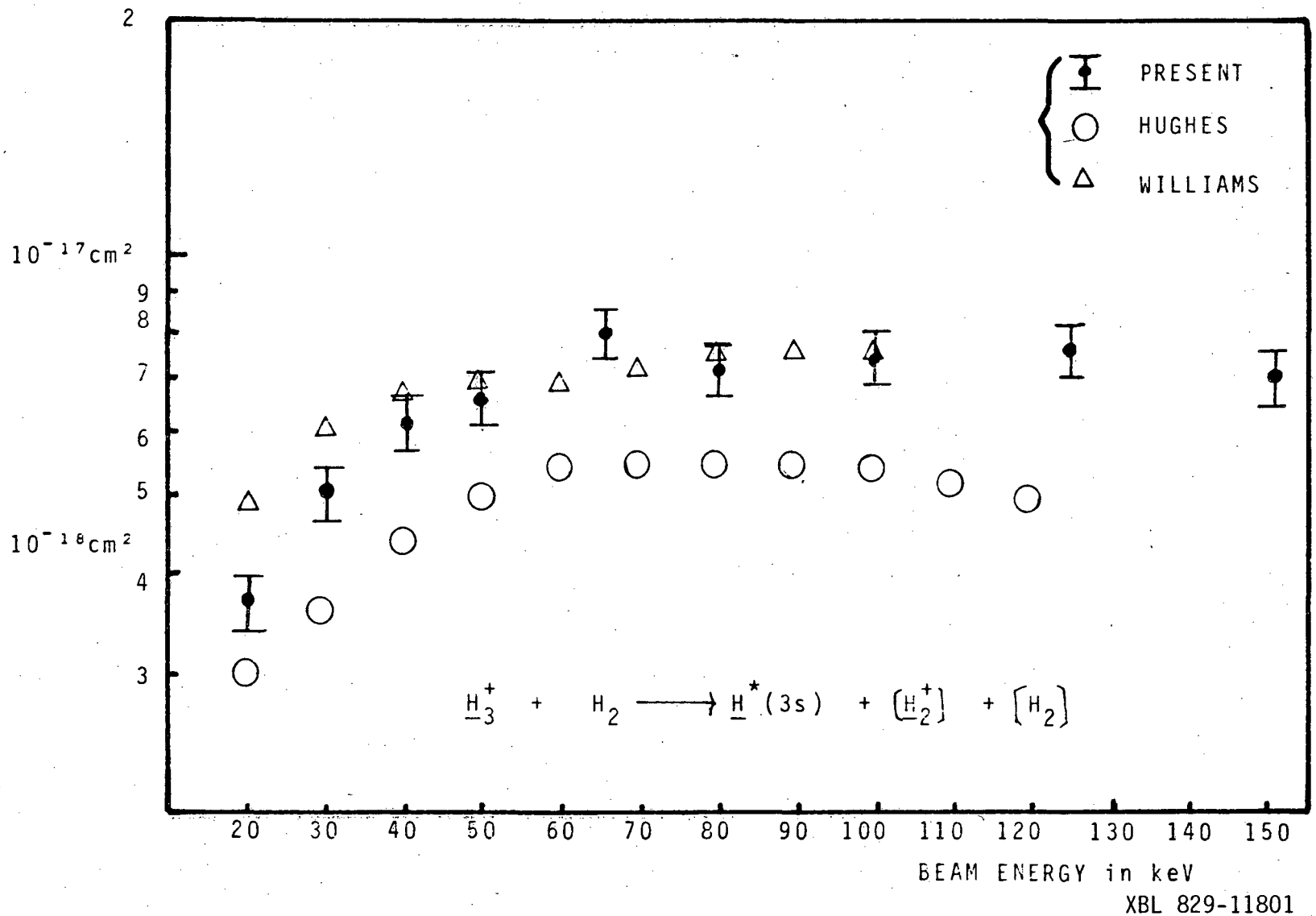
PRESENT
HUGHES
WILLIAMS
2
$10^{-17}cm^2$
9
8
7
6
5
$10^{-18}cm^2$
4
3
$\underline{H}_3^+ + H_2 \longrightarrow \underline{H}^*(3s) + [\underline{H}_2^+] + [H_2]$
20
30
40
50
60
70
80
90
100
110
120
130
140
150
BEAM ENERGY in keV
XBL 829-11801

Fig. 5-12

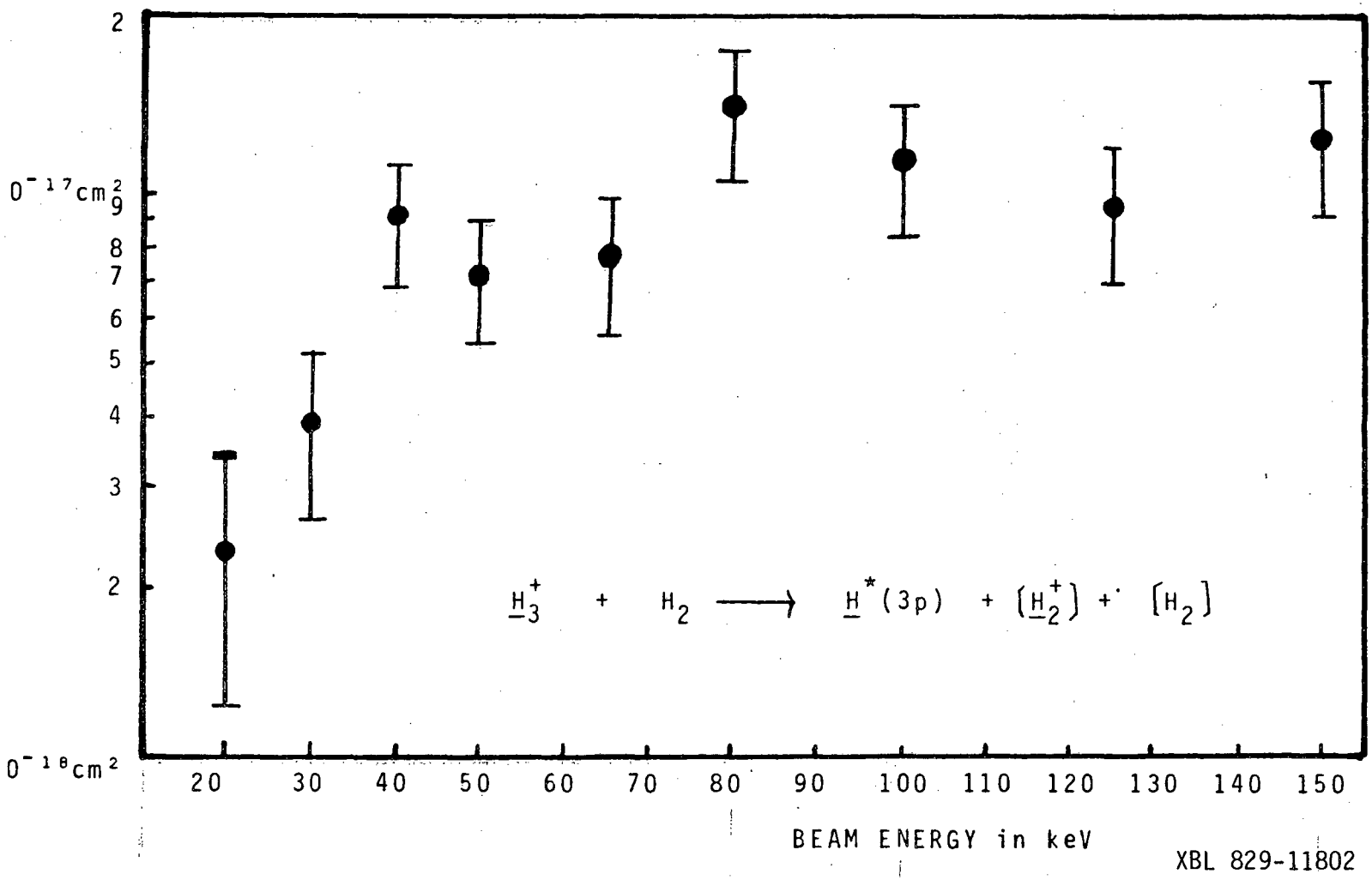
2
$10^{-17}cm^2$
9
8
7
6
5
4
3
2
$10^{-18}cm^2$
20
30
40
50
60
70
80
90
100
110
120
130
140
150
BEAM ENERGY in keV
$\underline{H}_3^+ + H_2 \longrightarrow \underline{H}^*(3p) + [\underline{H}_2^+] + [H_2]$
XBL 829-11802

Fig. 5-13

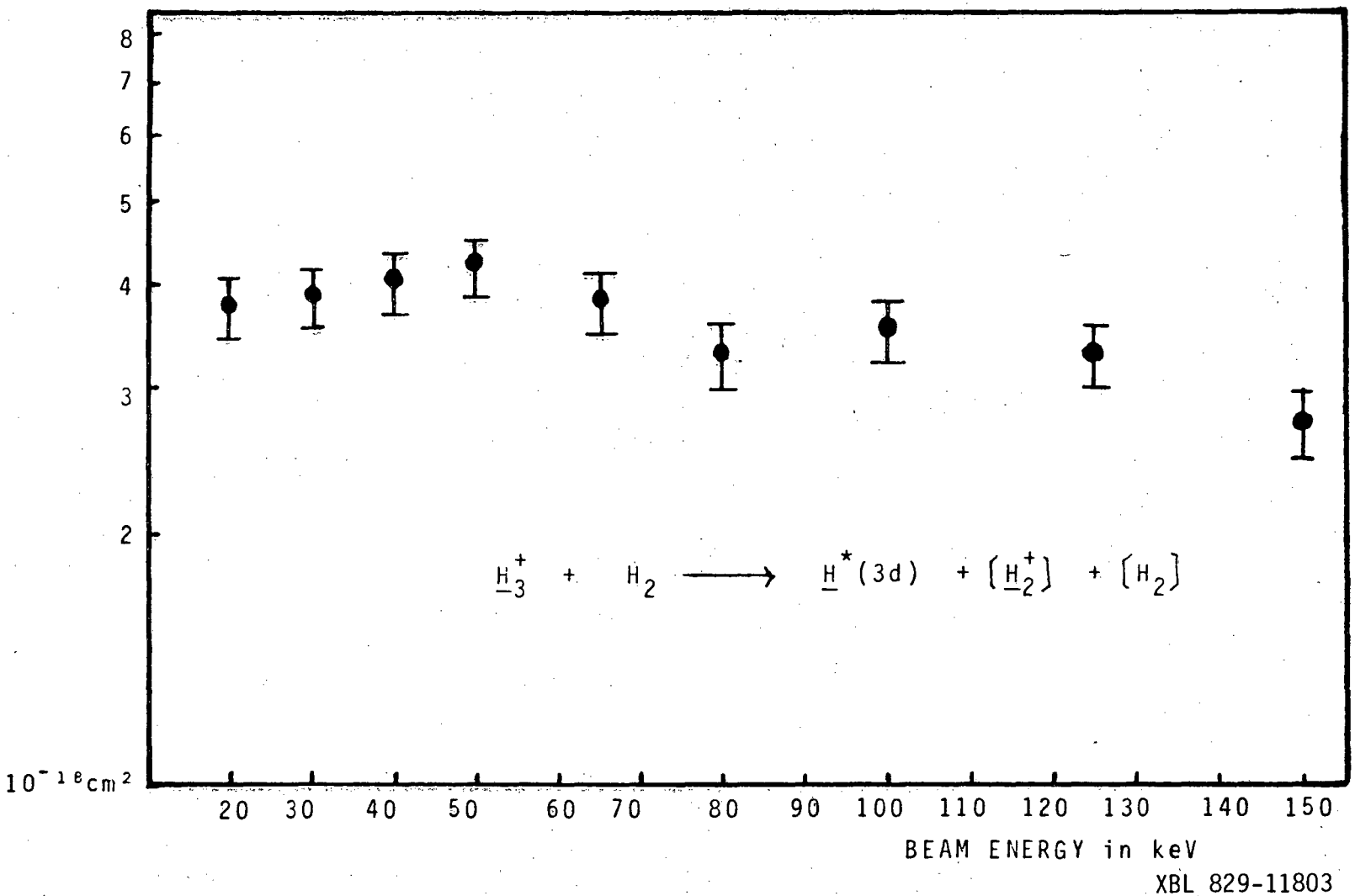

XBL 829-11803

Fig. 5-14

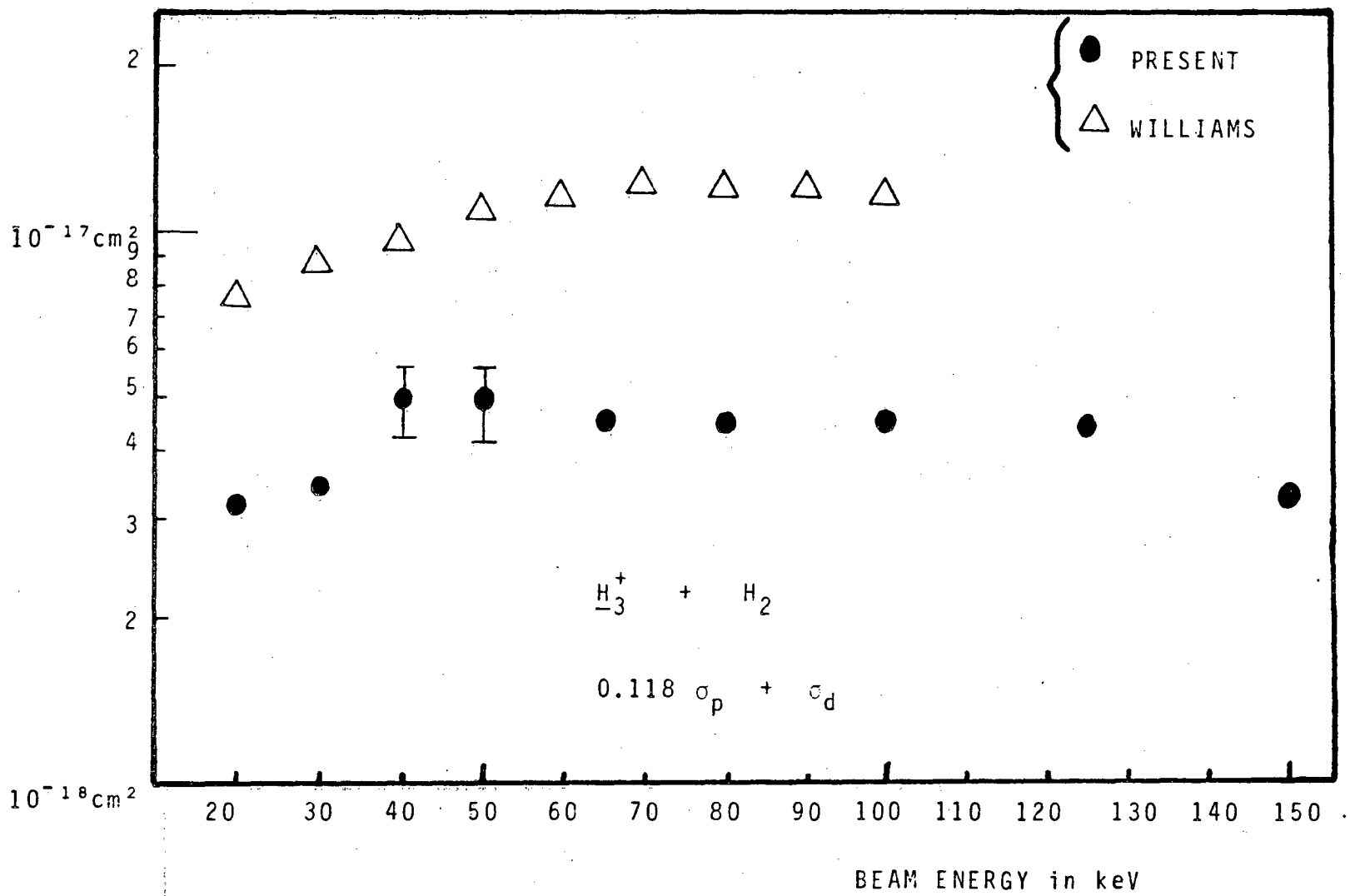

Fig. 5-15

XBL 829-11804

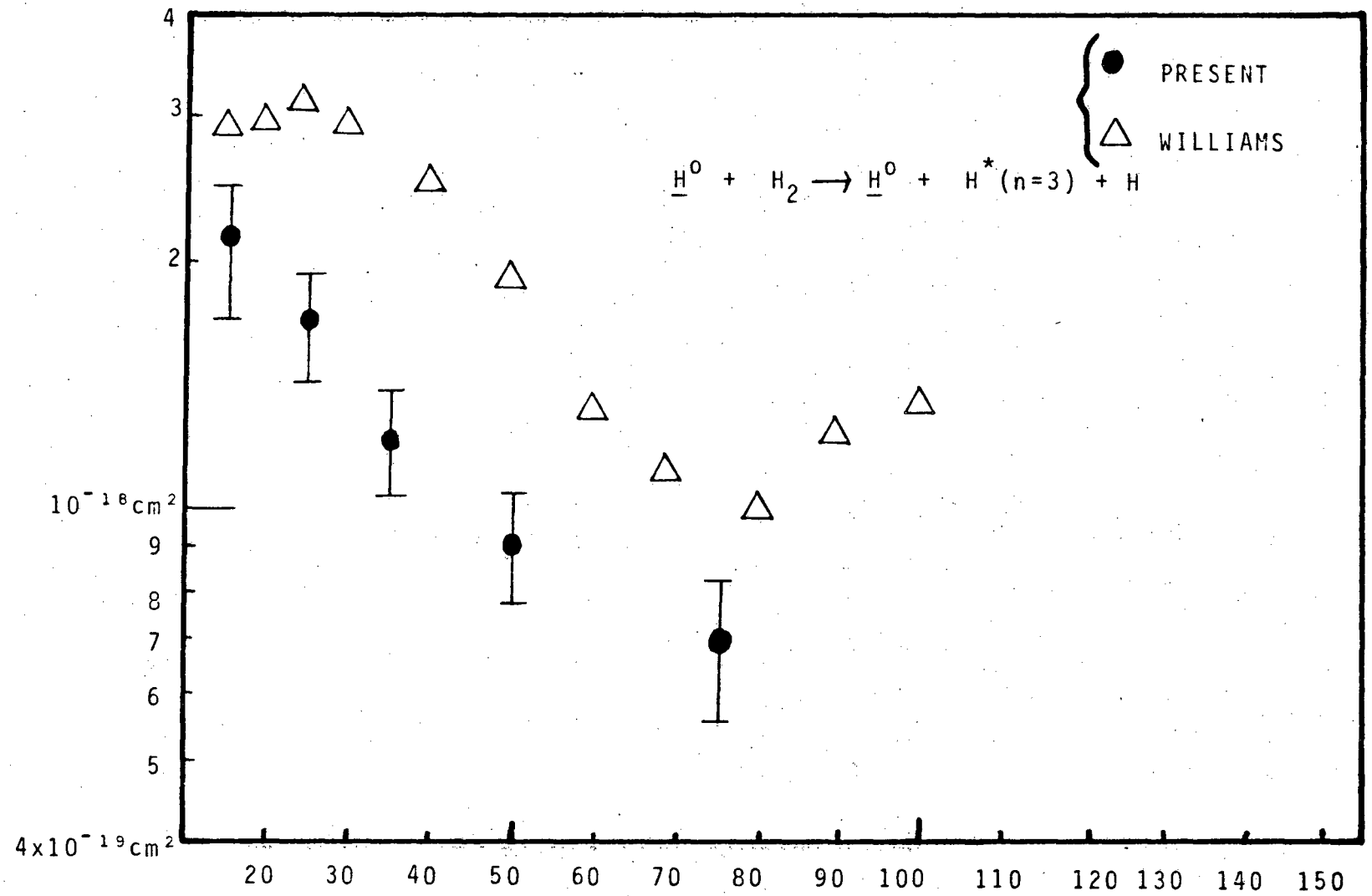

Fig. 5-16

XBL 829-11805

B. Discussion

a. H^+ case

There are three published sets of measurement, by Hughes[4], Ford[14] and Williams[29] for the case of H^+ incident on H_2. For 3s excitation cross sections (Fig. 5-2) Hughes', Thomas', and the present data agree completely with each other. The data by Williams show slightly larger cross sections within the energy range of 20 keV to 60 keV. The 3s state has the larger cross sections and therefore is the easiest to measure. There is poor agreement in the case of the 3p cross sections (Fig. 5-3) between Hughes' and the present results; on the other hand there is good agreement between Ford' and the present results. For the 3d cross sections (Fig. 5-4) Hughes' and the present results agree with each other generally, but Ford' results are a factor 10 smaller. Bates[32] and Mapleton[34] calculated theoretically the 3s, 3p and 3d charge capture cross sections of H^+ incident on H atom. Although there is no exact verification, in the high energy collision a target hydrogen molecule acts like two isolated hydrogen atoms except at very high energy where the backscattering contribution to the cross section becomes dominant[36]. Theoretical values of 3s, 3p and 3d charge capture cross sections by H^+ agree well with the present results.

For target dissociative excitation cross sections the present results show excellent agreement with Hughes'

although his maximum absolute uncertianty was 40%. The results by Ford are a factor 2 smaller than Hughes' and the present results. The results by Williams are about a factor 2 larger than Hughes' and the present results.

b. H_2^+ case

There are two published results for the case of target dissociative excitation of H_2^+ incident on H_2 (Fig. 5-5) by Hughes[5] and Williams[29]. Hughes' and the present results show good agreement with each other whereas the reaults by Williams are about a factor 2 larger than those two cross sections. Ford measured 3s and 3d dissociative excitation cross sections[16] (Fig. 5-6, Fig. 5-8) of the H_2^+ beam at the higher energies covered in this experiment, which show good agreement in the case of 3s cross section, but show poor agreement in the case of 3d cross section. The 3s cross sections by Hughes and Williams show good agreement with the present results. The 3p cross section by Andreev[51](Fig. 5-7) show good agreement with the present results within the experimental error range. Polarization was not observable within the experimental error range.

c. H_3^+ case

There are also two published results for the case of target dissociative excitation of H_3^+ incident on H_2 (Fig. 5-11) by Hughes[5] and Williams[29]. Hughes' and present

results show general agreement but the results of Williams are in poor agreement. Since the Doppler shifted cross sections by Hughes were measured in two different experimental geometries, some systematic fluctuation might be expected. This might explain the reason that the unshifted cross sections by Hughes are slightly larger than the present results; on the other hand, the Doppler shifted cross sections by Hughes are slightly smaller than the present ones. The 3s cross sections (Fig. 5-12) by Hughes and Williams show general agreement with the present results. There were no available 3p and 3d cross sections by other authors. Polarization effects were not observable within the experimental error range.

CHAPTER 6

Conclusions

There are two different methods of the excitation cross section measurement. The first one is the method of decay inside the target and the other one is that of decay outside the target. To date almost all experiments have been performed with the latter method. The conventional method of separation of different life-time states has been used in those experiment. But for short life-time states it is impossible to develop intensity decay curves due to the finite resolution in the length measurement. Numerical simulation was performed to verify this method. For the n=3 state excitation the 3p excitation cross section showed at least 100% less than the given value although there was 1% fluctuation in the decay curve. Also it was not possible to get the cross sections for H_2^+ and H_3^+ particles because of their slowness. On the other hand the measurements of those cross sections were possible by the method of the decay inside the target which was used in this experiment. Therefore, the main advantage of this method is that one can measure short life-time state excitation cross sections. The main difficulty of this method was that the single-collision condition should be confirmed for every step because the target thickness was changed in every step. Another advdntage was that it was possible to get the information of the target simult-

aneously. One could extend this method to the thick target experiment, but the statistical fluctuation didn't allow any convincing measurement. Another difficulty came from the fact that the excited state particles of the beam could not be distinguished from the ground state particles. For the atomic hydrogen experiment one can estimate the amount of the excited state atoms the n^{-3} law which is an empirical law. But this gives another unavoidable uncertainty.

In general two different types of optical system have been used. One type used a combination of filters and the other type used a monchromator. Because of small optical throughput of monchromator the former method was frequently used for Balmer- alpha excitation experiment. In the use of filters the transmittance versus wavelength should be developed with extreme care. And in procedure of calibration it is necessary to develop the relation between line radiation and continuous radiation. It was found that the calibration of the monochromator system was easier than that of a filter combination system.

There are two immediately possible experiments without any modification of this experiment. These are the case of H_2O^+ and H^0 impact on H_2. Since a H_2O^+ particle gives only 1/18 energy of the total beam energy to the hydrogen atom the expected Doppler shift of the radiation from the projectile should be small. If D_2O^+ is used instead of H_2O^+

more Doppler shift can be achieved. It is possible to get more resolution of the monochromator by modifying the slit width, but separate calibration factors are required. The ion source for H_2O^+ is now being developed and the magnet mass analyzer shows enough resolution to separate O^+, OH^+, H_2O^+ and H_3O^+as shown in Fig. 6-1.

In the case of H^o impact on H_2 additional electrostatic plates and a gas cell neutralizer are needed. The difficulty to perform this experiment mainly lies on the amount of beam. For the practical application the cross section of the dissociative excitation of H_2^o impact on H_2 is also needed. Up to date no experiment on H_2^o impact on H_2 has been tried, simply because it was nealy impossible to get a pure H_2^o beam. No practical method to pure H_2^o beams has been suggested.

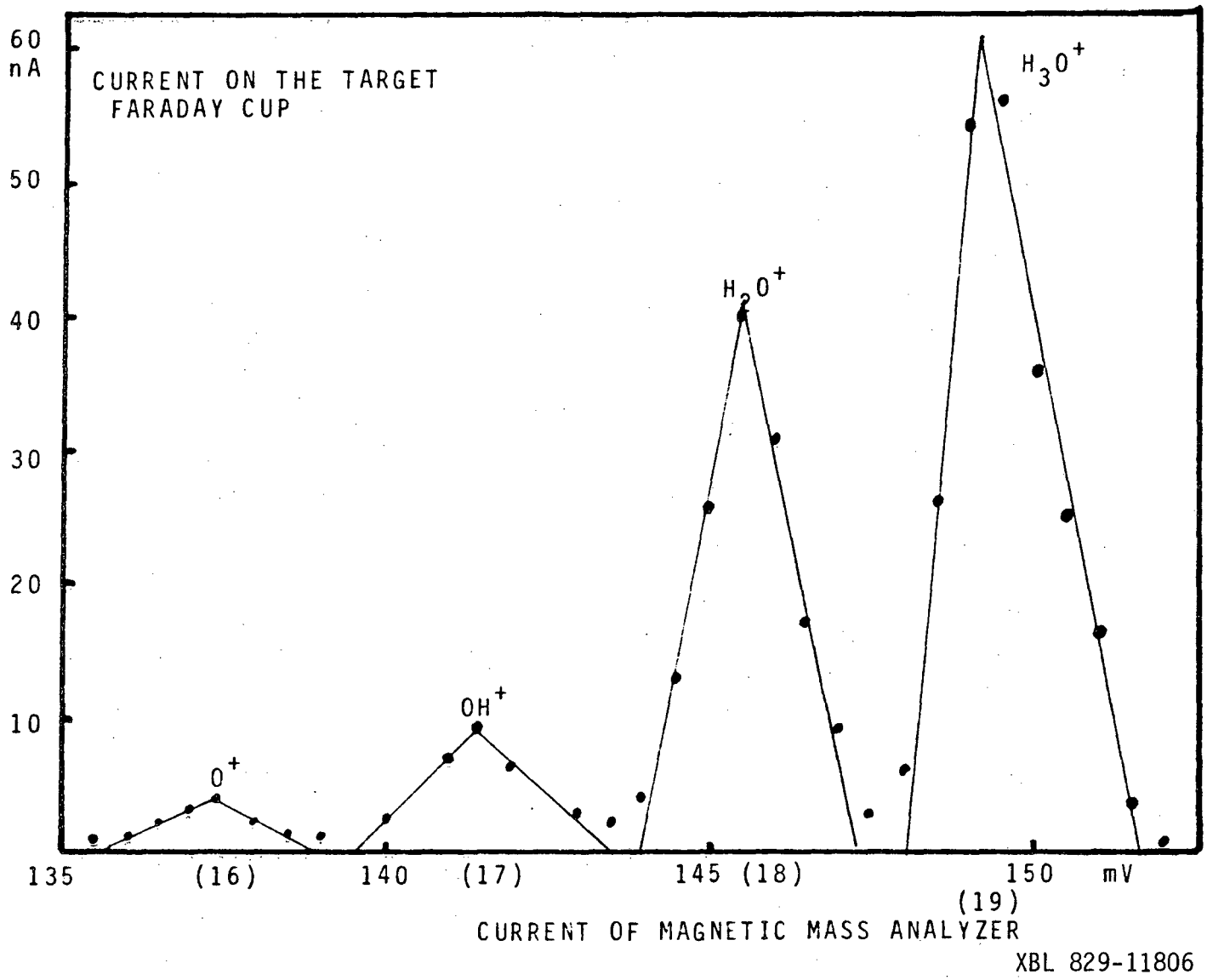

XBL 829-11806

Fig. 6-1

CHAPTER 7

References

1. K.H. Berkner, R.V. Pyle, J.W. Stearns, Nuc. Frs. 15, 249 (1975)

1a. C.F. Burrell, W.S. Cooper, W.F. Steele, R.R. Smith, in: Proc, 7th Symp. on Engineering problems of fusion research (Knoxville, 1977), IEEE 1, 374 (1977)

1b. R.H. Hughes, R.C. Waring and C.Y. Fan, Phy. Rev. 122, 525 (1961)

2. R.H. Hughes, S. Lin and L.L. Hatfield, Phy. Rev. 130, 2348 (1963)

3. L.L. Hatfield and R.H. Hughes, Phy. Rev. 134, 2556 (1963)

4. R.H. Hughes, H.R. Dawson, B.M. Doughty, D.B. Kay and C.A. Stigers, Phy. Rev. 146, 53 (1966)

5. R.H. Hughes, D.B. Kay, C.A. Stigers and E.D. Stokes, Phy. Rev. 167, 26 (1968)

6. R.H. Hughes, B.M. Doughty and A.R. Filippelli, Phy. Rev. 173, 172 (1968)

7. R.H. Hughes, A.R. Filippelli and H.M. Petefish, Phy. Rev. A. 1, 21 (1970)

8. R.H. Hughes, C.A. Stigers, B.M. Doughty and E.D. Stokes, Phy. Rev. A. 1, 1424 (1970)

9. R.H. Hughes, H.M. Petefish and H. Kisner, Phy. Rev. A. 5, 2103 (1972)

10. R.H. Hughes, H.M. Petefish and H. Kisner, Phy. Rev. A. 5, 2107 (1972)

11. R.H. Hughes and B.M. Doughty, J. Op. Soc. Am. 59, 659 (1969)

12. J.R. Edwards and E.W. Thomas, Phy. Rev. 165, 16 (1968)

13. J.L. Edwards and E.W. Thomas, Phy. Rev. A. 2, 2346 (1970)

14. J.C. Ford and E.W. Thomas, Phy. Rev. A. 5, 1694 (1972)

15. E.W. Thomas and J.C. Ford, Phy. Rev. A. 5, 1701 (1972)

16. J.C. Ford, F.M. McCoy, R. Conrads and E.W. Thomas, Phy. Rev. A. 5, 1705 (1972)

17. R.J. Conrads, T.W. Nichols, J.C. Ford and E.W. Thomas, Phy. Rev. A. 7, 1928 (1973)

18. H.R. Dawson and D.H. Loyd, Phy. Rev. A. 9, 166 (1974)

19. D.H. Loyd and H.R. Dawson, Phy. Rev. A. 11, 140 (1975)

20. H.R. Dawson and D.H. Loyd, Phy. Rev. A. 15, 43 (1977)

21. H.B. Gilbody, R. Browning, R.M. Reynolds and G.I. Riddel, J. Phys. B. 4, 94 (1970)

22. H.B. Gilbody and J.L. Corr, J. Phys. B. 14, 1953 (1974)

23. B. Van Zyl, T.Q. Le, H. Neumann and R.C. Amme, Phy. Rev. A. 15, 1871 (1977)

24. B. Van Zyl, H, Neumann, H.L. Rothwell, JR. and R.C. Amme, Phy. Rev. A. 21, 716 (1980)

25. B. Van Zyl, H.L. Rothwell, JR. and H. Neumann, Phy. Rev. A. 21, 730 (1980)

26. J. Kim and H.H. Haselton, J. Appl. Phy. 50(6), 3820 (1979)

27. J. De Heer, L. Wolterbeek Muller and R. Geballe, Physica 31, 1745 (1965)

28. I.D. Williams, J. Geddes and H.B. Gilbody, J. Phy. B. 15, 1377 (1982)

29. N.F. Mott and H.S.W. Massey, Theory of Atomic Collisions (Oxford U.P. New York) 2nd edition (1949)

30. J.R. Oppenheimer, Phy. Rev. 31, 349 (1928)

31. H.C. Brinkman, H.A. Kramers, Proc. Acad. Sci. Amsterdam, 33, 973 (1930)

32. D.r. Bates, A. Dalgarno, Proc. Phys. Soc. A. 66, 971 (1953)

33. J.D. Jackson, H. Shiff, Phy. Rev. 89, 359 (1953)

34. R.A. Mapleton, J. Phy. B. 1, 529 (1968)

35. M.L. Goldberger, K.M. Watson, Collision Theory (Wiley, New York), Chap. 5 (1964)

36. I.M. Cheshire, Proc. Phys. Soc. A. 82, 113 (1962)

37. L. Vriens, Case Studies in Atomic Collision Physics 1, ed. by E.W. McDaniel and M.R.C. McDowell (North Holland Publ. Co. Amsterdam) 1969

38. J.F. Tuan, E. Gerjuoy, Phy. Rev. 117, 756 (1960)

39. R.A. Mapleton, Proc. Phys. Soc. 83, 895 (1964)

40. J.P. Keene, Phil. Mag. 40, 369 (1949)

41. V.V. Afrosimov, R.N. Ilin and N.Y. Fedorenko, Zh. Eksperim. 1 Teor. Fiz. 34, 1398 (1958) (translation: Soviet phys. JETP 7, 968 (1958)

41a. E.U. Cordon and G.H. Shortley, The Theory of Atomic Spectra (Cambridge U.P.) (1979)

42. I.C. Percival and M.J. Seaton, Phil. Tran. Roy. Soc. London, A. 251, 113 (1958)

43. M. Born and E. Wolf, Principles of Optics, New York, Macmillan (1964)

44. G.R. Fowles, Introduction to Modern Optics, Holt, Rinehart and Winston, INC., New York (1968)

45. K.H. Berkner, B.R. Meyers and R.V. Pyle, Rev. of Sci. Inst. Vol. 39, No. 8, 1204 (1968)

46. G.A. Cottrell, A.R. Martin and C. Padgett, Proc. 2nd Joint Grenoble Varenna Int. Symp. on Heating in Toroidal Plasmas (Como 1980)

47. H.E. White, Introduction to Atomic Spectra, McGrow-Hill, New York (1934)

48. W.W. Hicks, LBL Report-2470 (1973)

49. D.R. Bevington, Data Reduction and Error Analysis for the Physical Sciences, McGrow-Hill, New York (1969)

50. E.W. Thomas, Excitation in Heavy Particle Collisions, Wiley-Interscience, New York (1972)

51. E.P. Andreev, V.A. Ankudinov and S.V. Bobashov,

Fifth International Conference on the Physics of Electronic and Atomic Collisions: Abstract Paters, p. 309, Publishing House Nanka Leningrad, USSR (1967)

52. J.M. Stone, Radition and Optics: an Introduction to the Classical Theory, McGrow-Hill, New York (1963)

CHAPTER 8

Appendices

A. Discussion of the monochromator

In this section the detailed broadening effects of the monochromator used in this work are presented. As shown in Fig. 8-1 the monochromator was designed to give large optical throughput (f number was 3.7) and was composed of a 30 cm focal length and 8.2 cm diameter achromatic lens, a 1200 line ruling per mm grating, one 1" x 1" 90° prism and a plain red filter. The slit heights of both entrance and exit slit were 1 cm and the slit widths were set to be 1.2 mm. The plain red filter was used to cut down the overlaping blue spectrum from the third order diffraction because in order to give maximum refractance the monochromator was set to give the second order diffraction of the grating. The adjustment of the monochromator was done with a white light source and a He-Ne laser. The wavelength calibration of the monochromator was done with H_2, Na and Ne discharge lamps.

The first factor of the instrumental broadening was due to the natural grating resolution. Consider the case of the monochromatic light with wavelength λ incident on the entrance slit. Assume that the light with wavelength λ which passes through the center of the entrance slit and is

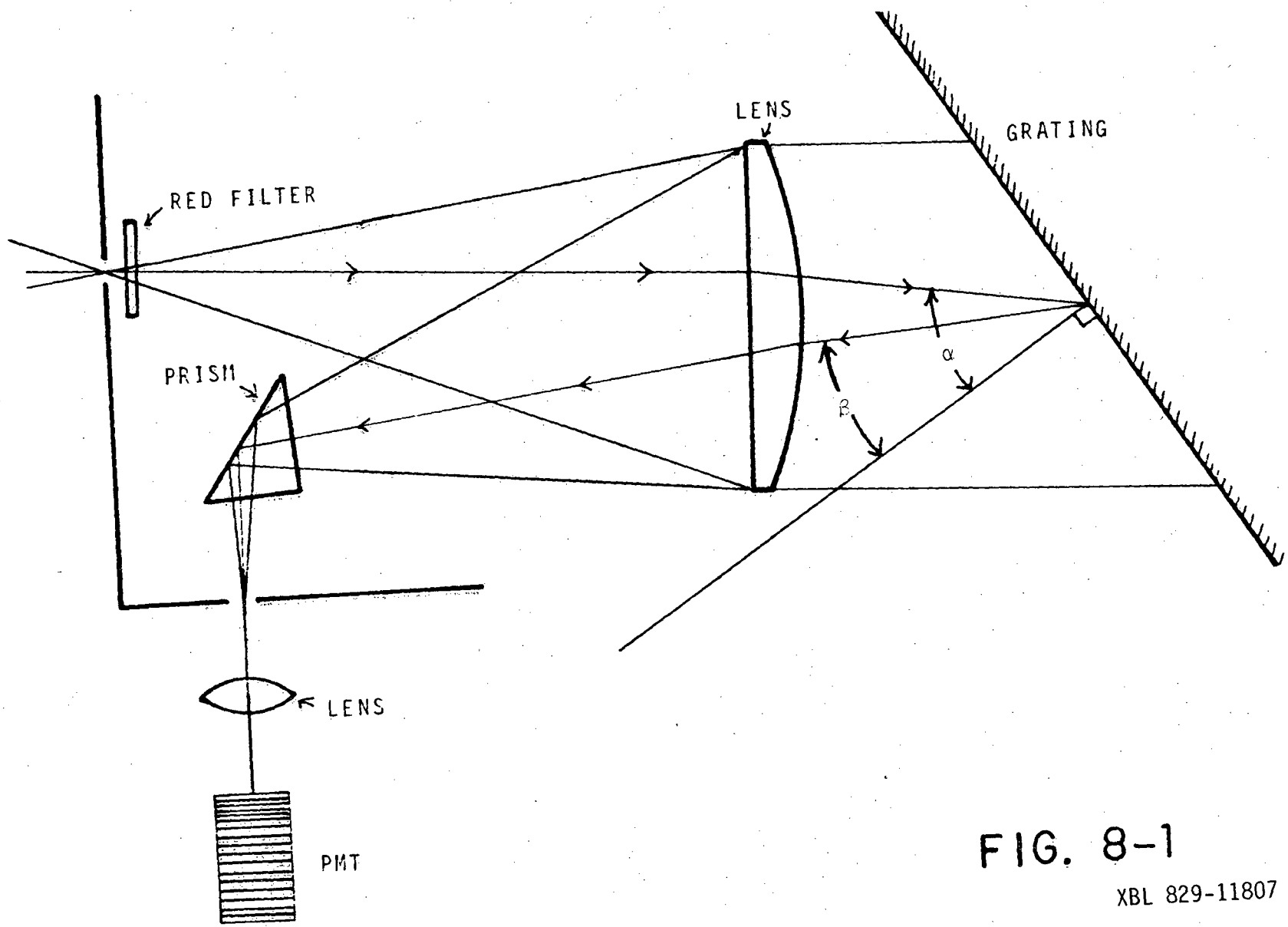

FIG. 8-1

XBL 829-11807

incident on the grating at the corresponding angle α and is diffracted into an angle β , also passes through the center of the exit slit. Then α and β must satisfy the usual grating equation such as

$$\frac{d}{\lambda} \left(\sin\alpha + \sin\beta \right) = m \qquad (8\text{-}1)$$

where d is the spacing between rulings on the grating and m is the order of the grating maxima. The dispersion D which gives the displacement at the exit slit corresponding to a unit change in the wavelength λ is given by

$$D = \frac{dy}{d\lambda} = F \frac{d\beta}{d\lambda} = \frac{F\,m}{d\cos\beta} \qquad (8\text{-}2)$$

where F is the focal length of the achromatic lens. The intensity $I(x,y)$ at a position y (or for the diffracted angle β') of the exit slit due to unit intensity of light with wavelength incident on the entrance slit at a position x corresponding incident angle α' is given by[52]

$$I(x,y) = \frac{d}{\lambda} \left(\sin\alpha' - \sin\alpha + \sin\beta' - \sin\beta \right)$$
$$\simeq \frac{d}{\lambda F} \left(x \cos\alpha + y \cos\beta \right) \qquad (8\text{-}3)$$

From this equation a full width at half maximum intensity is given by

$$w = \frac{0.88\ \lambda\ D}{m\ N} = \frac{0.88\ \lambda\ F}{d\ N\ \cos\beta} \qquad (8\text{-}4)$$

With the equations (8-2) and (8-4) the broadening due to the natural grating resolution is given by

$$\Delta\lambda_G = \frac{d\ \cos\beta}{m\ F}\ w = \frac{0.88}{m\ N}\ \lambda \qquad (8\text{-}5)$$

where N is the total number of rulings on the grating. In this experiment $\Delta\lambda_G$ was much less than 1 Å.

The main broadening effect was due to the finite slit width, where w in the previous equation was given by a full value of the slit width. From this equation the broadening due to the finite slit width is given by

$$\Delta\lambda_s = \frac{d\ \cos\beta}{mF}\ s \qquad (8\text{-}6)$$

where s is the slit width and $\sin\beta = \lambda/d$. In this experiment F= 30 cm, m=2, s=0.12 cm, d= 1/12000 cm and $\cos\beta \simeq 0.6$, therefore, $\Delta\lambda_s$ was about 10 Å.

There were other broadening effects due to curvature of the image of the entrance slit at the exit slit, etc. But they were quite negligible. The total instrumental broadening was given by the square root of the square sum of the individual broadening effect. This is

$$\Delta\lambda_I = \sqrt{\Delta\lambda_s + \Delta\lambda_G + \Delta\lambda_c + \ldots} \simeq 10\ \text{Å} \qquad (8\text{-}7)$$

B. Comments on the Thick Target Experiments

To date there have been no multiple collision experiments. The reason is that in order to do that one must handle a very complicated situation and deduce cross sections from indirect measurements. But for real applications it is necessary to deal with such a thick target system. Therefore, the description (analytically or numerically) of that system is strictly required. In this section the intensity evolution of the excited state atoms in the multiple collision system is presented with consideration of the cascading effect. The local intensity of the excited state atoms is determined by the competition between the life time decay effect, the collisional decay (or excitation) effect and the excitation from the primary and secondary particles. Since the cascading term could be treated self-consistently, it was treated by perturbation method in this calculation.

Consider the radition which comes from the fast particles in the case of H^+ incident on H_2 gas. Let the parameters be

v ; velocity of the fast particle,

τ_i ; life time of the excited state i,

N_a ; target density,

N_b ; density of the projectile,

x ; travel distance of the beam from the entrance aperture,

Q_{ij} ; cross section for collisional transition between the state i and j,

Q_i^o ; excitation cross section from the ground state,

Q_i^+ ; electron capture cross section of H^+ into the excited state i,

Q_i^{2+} ; dissociative excitation cross section of H_2^+ into H atom of the state i,

Q_i^{3+} ; dissociative excitation cross section of H_3^+ into H atom of the state i.

Then the excited state density N_{bi} follows the equation

$$\frac{dN_{bi}}{dx} = -\frac{1}{v\tau_i} N_{bi} - N_a \left(\sum_{j \neq i} Q_{ij} \right) N_{bi} + N_a N_b \left(Q_i^o y_o + Q_i^+ y_+ \right) \qquad (8\text{-}8)$$

The first term represents the life time decay of the excited state i, the second term represents collisional transition from the state i to the state j, the third term is for the excitation of H^o particle into the state i and the fourth term is for the charge capture of H^+ particle into the state i. The previous equation can be written again as

$$\frac{dN_{bi}}{dx} = -\alpha_i N_{bi} + \left(y_o Q_i^o + y_+ Q_i^+ \right) N_a N_b \qquad (8\text{-}9)$$

where $\alpha_i = 1/v\tau_i + N_a \sum_{i \neq j} Q_{ij}$.

The solution of this equation with the boundary conditions is given by

$$N_{bi} = \frac{N_a N_b}{\alpha_i} (F_{o\infty} Q_i^o + F_{1\infty} Q_i^+) (1 - e^{-\alpha_i x}) + \frac{N_a N_b}{\alpha_i - \beta} F_{o\infty} (Q_i^+ - Q_i^o)(e^{-\beta x} - e^{-\alpha_i x}) \quad (8\text{-}10)$$

where $\beta = N_a (\sigma_{10} + \sigma_{01})$, $F_{o\infty} = \sigma_{10} /(\sigma_{10} + \sigma_{01})$ and $F_{1\infty} = \sigma_{01} /(\sigma_{10} + \sigma_{01})$.

The total radiation strength from the portion ℓ of the beam is given by

$$J = \sum_i \int_L^{L+\ell} A N_{bi} A_{ij} dx \quad (8\text{-}11)$$

for $L >> \ell$, J can be written

$$J = A \ell \sum_i A_{ij} N_{bi} \quad (8\text{-}12)$$

The equation which include cascading effect can be written as

$$\frac{dN_{bi}}{dx} = - \alpha_i N_{bi} + (y_o Q_i^o + y_+ Q_i^+) N_a N_b + \frac{1}{v} \sum_{k>i} A'_{ki} N_{bk} \quad (8\text{-}13)$$

where $A'_{ki} = A_{ki} + Q_{ki} N_a v$.

In this way the solution can be developed like

$$N_{bi} = N^o_{bi} + N^1_{bi} \tag{8-14}$$

and the equation for the first order perturbation term is

$$\frac{dN^1_{bi}}{dx} = -\alpha_i N^1_{bi} + \frac{1}{v} \sum_{k>i} A'_{ki} N^o_{bk} \tag{8-15}$$

In general including H_2^+ and H_3^+ case the master equation is given by

$$\frac{dN_{bi}}{dx} = -\alpha_i N_{bi} + N_a N_b Y^q_i + \frac{1}{v} \sum_{k\ i} A'_{ki} N_{bk} \tag{8-16}$$

where Y^q_i is given by

$$\begin{aligned} H^+ \text{ case ;} \quad & Y^1_i = y_o Q^o_i + y_+ Q^+_i \\ H_2^+ \text{ case ;} \quad & Y^2_i = y_{20} Q^{20}_i + y_{2+} Q^{2+}_i + Y^1_i \\ H_3^+ \text{ case ;} \quad & Y^3_i = y_{3+} Q^{3+}_i + Y^2_i \end{aligned} \tag{8-17}$$

where Q^{20}_i is the dissociative excitation cross section of H^o_2 into H atom of the state i . The solutions for y_o, y_+, etc. are derived by Kim[26] analytically. Using the same notations the parameters are given by

$$S_{\binom{1}{2}} = \frac{1}{2}\left(C^{21}_{01} + C^{21}_{00} \right) + C^{22}_{\binom{01}{10}} ,$$

$$\gamma'_0 = 0$$

$$\gamma'_{\binom{1}{2}} = \frac{1}{2}\left(S_1 + S_2 \binom{+}{-} \sqrt{\left(S_1 - S_2 \right)^2 + C^{22}_{10} C^{22}_{01}} \right)$$

$$\gamma'_3 = \frac{1}{3}\left(C^{31}_{11} + C^{31}_{10} \right) + \frac{2}{3}\left(C^{32}_{11} + C^{32}_{10} \right)$$

$$\varepsilon = C^{11}_{10} + C^{11}_{01} = \beta \; N_a \tag{8-17}$$

and for cyclic i,j and k (for (i,j,k) = (1,2,3))

$$G_i = (-1)^{i-1} \frac{C^{32}_{10} C^{22}_{10} - C^{32}_{10}\left(\gamma'_i - S_2 \right)}{\left(\gamma_i - \gamma_j \right)\left(\gamma_i - \gamma_k \right)}$$

$$H_i = - \frac{C^{32}_{11} C^{22}_{10} - C^{32}_{01}\left(\gamma'_i - S_2 \right)}{\left(\gamma_i - \gamma_j \right)\left(\gamma_i - \gamma_k \right)} \tag{8-18}$$

and

$$K_{\binom{1}{2}} = \frac{G_{\binom{1}{2}}\left(C^{21}_{00} - 2C^{11}_{10} \right) + H_{\binom{1}{2}}\left(C^{21}_{10} - 2C^{11}_{10} \right)}{\varepsilon - \gamma'_{\binom{1}{2}}}$$

$$K_3 = \frac{G_3\left(C^{21}_{00} - 2C^{11}_{10}\right) + H_3\left(C^{21}_{10} - 2C^{11}_{10}\right) + C^{31}_{10} - 3C^{11}_{10}}{\varepsilon - \gamma'_3} \tag{8-19}$$

and for cyclic (i,j)=(1,2)

$$C_i = \frac{C_{10}^{22} \; C_{01}^{22}}{\gamma_i - \gamma_j} \cdot \frac{1}{S_2 - \gamma_i}$$

$$D_i = \frac{(S_2 - \gamma_j') \; (C_{10}^{21} - 2C_{10}^{11}) - C_{10}^{22}(C_{00}^{21} - 2C_{10}^{11})}{(\gamma_i - \gamma_j') \; (\varepsilon - \gamma_i')} \tag{8-20}$$

and $E_1 = -E_2 = \dfrac{C_{10}^{22}}{\gamma_2' - \gamma_1'}$

where C's are cross sections multiplied by N_a and are shown in Fig. 8-2 and Fig. 8-3.

Then the solutions are given by

H^+ case ; $y_o = F_{o\infty} \; (1 - e^{-\varepsilon x})$

$y_+ = 1 - y_o$

H_2^+ case ; $y_{2+} = \sum_{m=1}^{2} C_m \; e^{-\gamma_m' x}$

$y_{20} = \sum_{m=1}^{2} E_m \; e^{-\gamma_m' x}$

$y_o = 2F_{o\infty}(1 - e^{-\varepsilon x}) + \sum_{m=1}^{2} D_m(e^{-\gamma_m' x} - e^{-\varepsilon x})$

$y_+ = 2 - y_o - 2(y_{20} + y_{2+})$

H_3^+ case ; $y_{3+} = e^{-\gamma_3' x}$

$y_{20} = \sum_{m=1}^{3} G_m \; e^{-\gamma_m' x}$

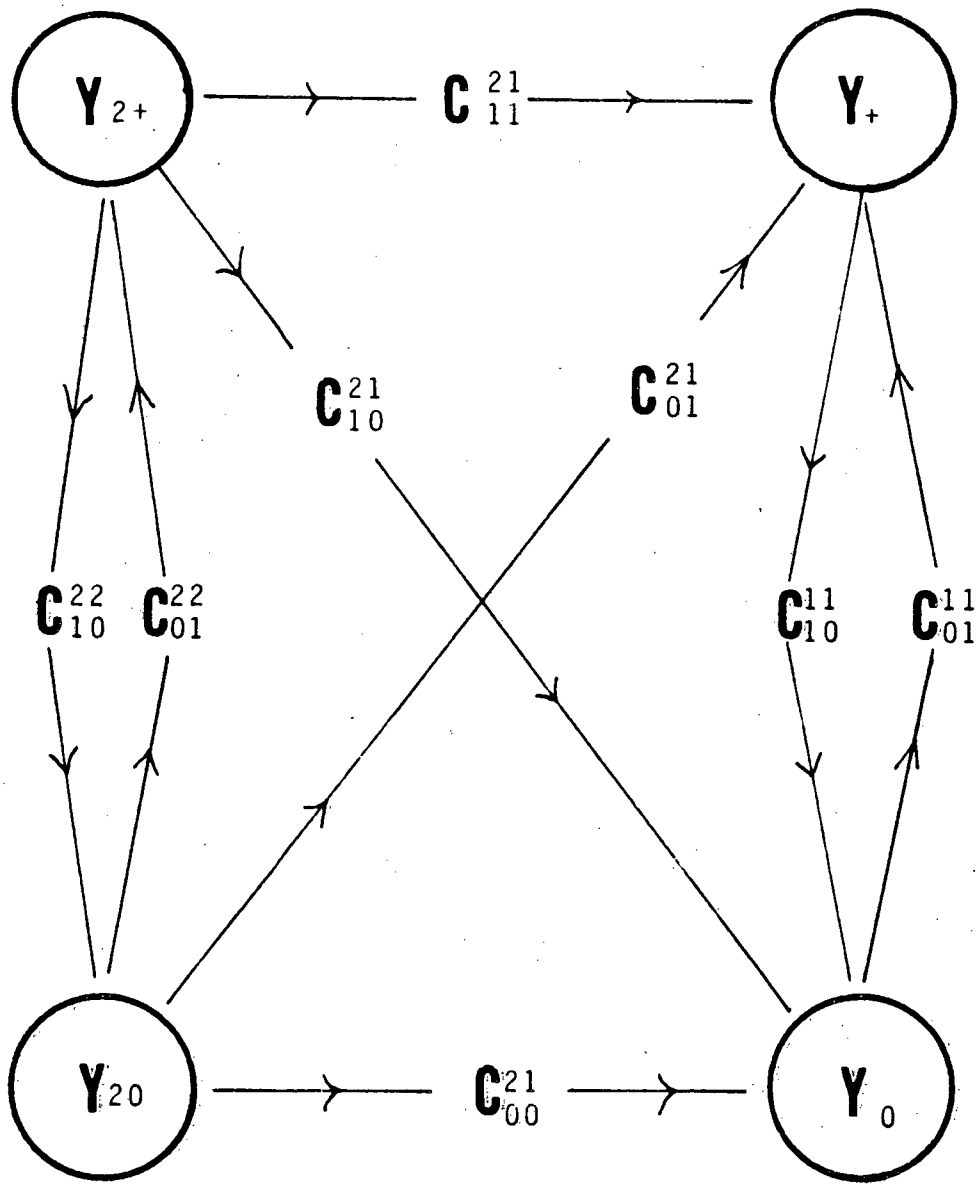

XBL 829-11808

Fig. 8-2

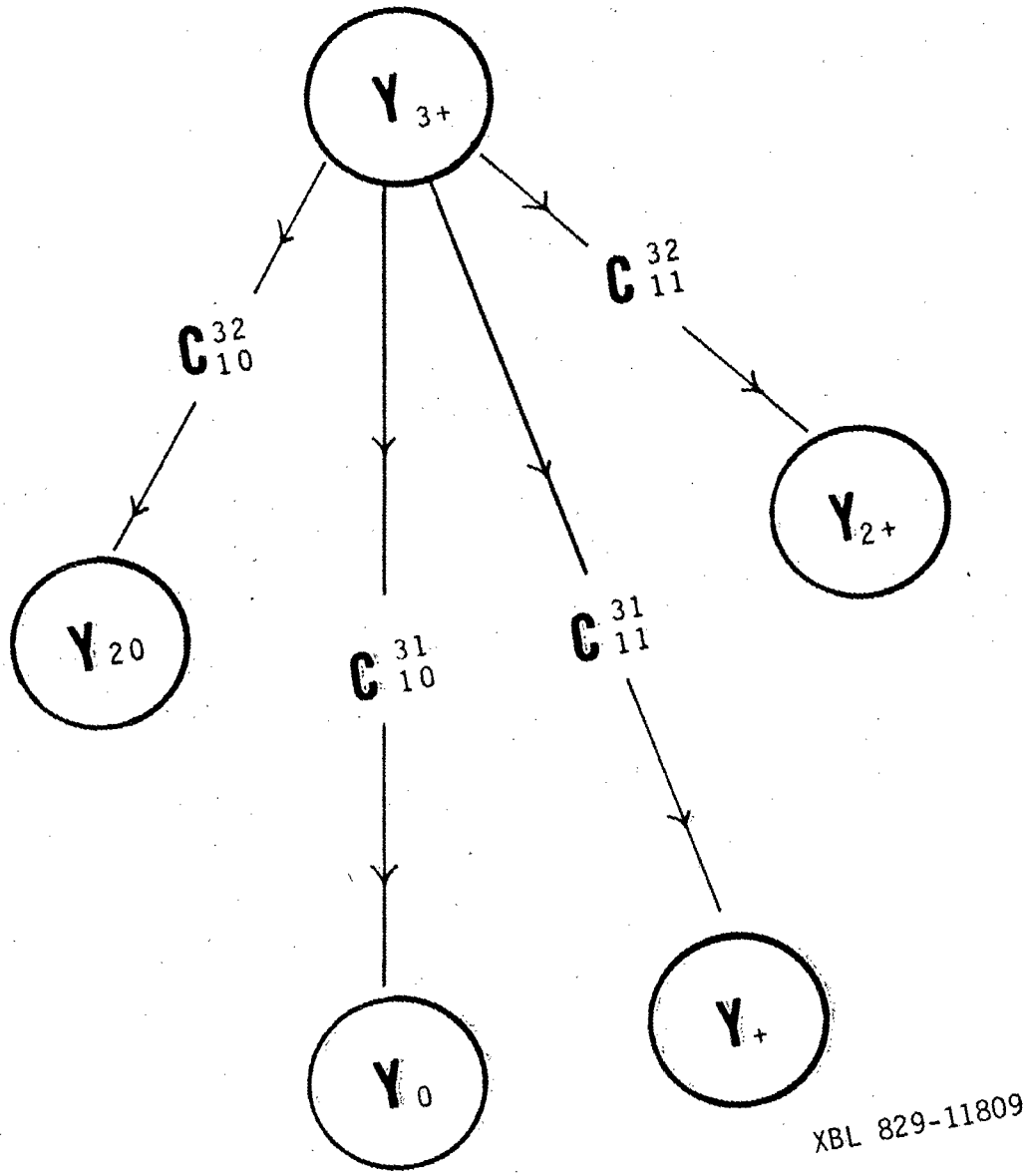

Fig. 8-3

$$y_{2+} = \sum_{m=1}^{3} H_m \; e^{-\gamma_m' x}$$

$$y_0 = 3F_o \; (1 - e^{-\varepsilon x}) + \sum_{m=1}^{3} K_m (e^{-\gamma_m' x} - e^{-\varepsilon x})$$

$$y_+ = 3 - y_0 - 2y_{20} - 2y_{2+} - 3y_{3+}$$

In the case of H^+, let $\gamma_1 = \varepsilon$ and let

$$f_i^o = \frac{3 \; N_a N_b}{\alpha_i} \; (\; F_{o\infty} \; Q_i^o \; - \; F_{1\infty} \; Q_i^+ \;)$$

$$f_i^1 = \frac{N_a N_b}{\gamma_1 - \alpha_i} \; (\; Q_i^o \; - \; Q_i^+ \;) \; F_{o\infty}$$

then the solution is given by

$$N_{bi}^o = \sum_{m=0}^{1} f_i^m \; (\; e^{-\gamma_m x} \; - \; e^{-\alpha_i x} \;)$$

$$N_{bi}^1 = \frac{1}{v} \sum_{k>i} A_{ik}' \; (\; \sum_{m=0}^{1} \frac{f_k^m}{\alpha_i - \gamma_m} \; (\; e^{-\gamma_m x} - e^{-\alpha_i x} \;)$$

$$+ \frac{\sum_{m=0}^{1} f_k^m}{\alpha_i - \alpha_k} \; (\; e^{-\alpha_i x} - e^{-\alpha_k x} \;) \;)$$

In the case of H_2^+, let $\gamma_3 = \varepsilon$ and for $j=1,2$ let $\gamma_j = \gamma_j'$

$$F_i^j = \frac{N_a \; N_b}{\alpha_i - \gamma_j} \; (\; (Q_i^{20} - 2Q_i^+)E_j + (Q_i^{2+} - 2Q_i^+)C_j$$

$$+ \left(Q_i^o - Q_i^+ \right) D_j \quad)$$

$$F_i^3 = \frac{N_a \; N_b}{\gamma_3 - \alpha_i} \left(Q_i^o - Q_i^+ \right) \left(2F_{o\infty} + \sum_{m=1}^{2} D_m \right)$$

then the solution is given by

$$N_{bi}^o = \sum_{m=0}^{3} F_i^m \left(e^{-\gamma_m x} - e^{-\alpha_i x} \right)$$

$$N_{bi}^1 = \frac{1}{v} \sum_{k>i} A'_{ik} \left(\sum_{m=0}^{3} \frac{F_k^m}{\alpha_i - \gamma_m} + \frac{\sum_{m=0}^{3} F_k^m}{\alpha_i - \alpha_k} \left(e^{-\alpha_i x} - e^{-\alpha_k x} \right) \right)$$

In the case of H_3^+ for j=1, 2 and 3, let $\gamma_4 = \varepsilon$ and $\gamma_j = \gamma'_j$ and let

$$F_i'^j = \frac{N_a \; N_b}{\alpha_i - \gamma_j} \left((Q_i^{2o} - 2Q_i^+) G_j + (Q_i^{2+} - 2Q_i^+) H_j \right.$$

$$\left. + \; (Q_i^0 - Q_i^+) K_j \right)$$

$$F_i'^4 = \frac{N_a \; N_b}{\gamma_4 - \alpha_i} \left(Q_i^0 - Q_i^+ \right) \left(3 \, F_{o\infty} + \sum_{m=1}^{3} K_m \right)$$

then the solution is given by

$$N_{bi}^o = \sum_{m=0}^{4} F_i'^m \left(e^{-\gamma_m x} - e^{-\alpha_i x} \right)$$

$$N_{bi}^{1} = \frac{1}{v} \sum_{k>i} A'_{ik} \left(\sum_{m=0}^{4} \frac{F_k'^{m}}{\alpha_i - \gamma_m} \left(e^{-\gamma_m x} - e^{-\alpha_i x} \right) + \frac{\sum_{m=0}^{4} F_k'^{m}}{\alpha_i - \alpha_k} \left(e^{-\alpha_i x} - e^{-\alpha_k x} \right) \right)$$

This report was done with support from the Department of Energy. Any conclusions or opinions expressed in this report represent solely those of the author(s) and not necessarily those of The Regents of the University of California, the Lawrence Berkeley Laboratory or the Department of Energy.

Reference to a company or product name does not imply approval or recommendation of the product by the University of California or the U.S. Department of Energy to the exclusion of others that may be suitable.

TECHNICAL INFORMATION DEPARTMENT
LAWRENCE BERKELEY LABORATORY
UNIVERSITY OF CALIFORNIA
BERKELEY, CALIFORNIA 94720